JOSEF SCHUPP

# INTERFACE BETWEEN TRAPPED-ION QUBITS AND TRAVELLING PHOTONS WITH CLOSE-TO-OPTIMAL EFFICIENCY

# INTERFACE BETWEEN TRAPPED-ION QUBITS AND TRAVELLING PHOTONS WITH CLOSE-TO-OPTIMAL EFFICIENCY

JOSEF SCHUPP

Thesis submitted to the
Faculty of Mathematics, Computer Science and Physics
of the Leopold-Franzenz University of Innsbruck
in partial fulfilment of the requirements for the degree of

Doctor of Philosophy
(Physics)

Carried out under supervision of
o. Univ.-Prof. Dr. Rainer Blatt
and
Ass. Prof. Dr. Ben Lanyon
at the Institute for Quantum Optics and Quantum Information (IQOQI),
Innsbruck

December 2021

Für Simon, den Bams.

## ABSTRACT

A quantum version of the internet, built of interacting quantum light and matter, would enable powerful new capabilities for science and technology. A key requirement for the quantum internet is the ability to efficiently collect photons that are emitted by and entangled with quantum matter. This thesis reports on a significant increase in the efficiency of photon collection from a leading example of quantum matter: a single trapped atomic ion.

In particular, the thesis presents the design and construction of an ion-photon interface and an experimental investigation of the interface's efficiency limits. The interface consists of a trapped $^{40}Ca^{+}$ ion in the focus of a near-concentric optical cavity of 20 mm length. A photon, entangled with the ion, is obtained with a probability of 0.69(3) at the cavity output and is detected with a probability of 0.462(3). These efficiencies are far beyond the previous state of the art for a trapped ion and, to the best of our knowledge, the highest reported for emitter-photon entanglement for any example of quantum matter. As we show, our interface achieves close to the optimal compromise between the probability of a photon being emitted into the cavity mode and exiting through the output mirror. Moreover, the interface is shown to operate at the theoretical efficiency limit, such that no statistically significant improvements in efficiency can be obtained without changing properties of the atom or the cavity. This result clearly identifies the parameter regimes to focus on for future improvements and provides a guide for the design of general emitter-cavity systems that are optimised for efficient photon interfacing.

A further result of this thesis is the distribution of a photon, entangled with the ion, over a distance of 50 km of optical fibre. A key component here is the conversion of the photon's wavelength to the telecom band at 1550 nm whilst preserving ion-photon entanglement. The achieved distance is two orders of magnitude larger than the previous record for light-matter entanglement and constitutes a practical distance to start building long-distance quantum networks.

High-efficiency and long-distance distribution of light-matter entanglement are both key characteristics of envisioned quantum networks. The state-of-the-art values in both parameters achieved in this thesis clearly demonstrate the suitability of trapped ions coupled to optical cavities to serve as quantum network nodes.

# ZUSAMMENFASSUNG

Ein Internet, welches auf den Gesetzen der Quantenmechanik basiert und aus welchselwirkenden Licht- und Materiequanten aufgebaut ist, würde leistungsstarke neue Fähigkeiten für Wissenschaft und Technik ermöglichen. Eine wichtige Voraussetzung für das Quanteninternet ist das effiziente Sammeln von Photonen, die von Quantenmaterie emittiert werden und mit ihr verschränkt sind. In dieser Doktorarbeit wird über eine erhebliche Steigerung der Effizienz für das Sammeln von Photonen von einem einzelnen gefangenen atomaren Ion berichtet.

Insbesondere werden in dieser Arbeit der Entwurf und die Konstruktion einer Ionen-Photonen-Schnittstelle sowie eine experimentelle Untersuchung der Effizienzgrenzen der Schnittstelle vorgestellt. Die Schnittstelle besteht aus einem gefangenen $^{40}Ca^{+}$-Ion im Fokus eines nahezu konzentrischen, 20 mm langen, optischen Resonators. Ein Photon, das mit einem Ion verschränkt ist, wird mit einer Wahrscheinlichkeit von 0,69(3) am Ausgang des Resonators erhalten und mit einer Wahrscheinlichkeit von 0,462(3) detektiert. Diese Wahrscheinlichkeiten übertreffen die bisherigen Bestleistungen für gefangene Ionen bei weitem und sind unseres Wissens nach die höchsten, die bisher für Emitter-Photonen-Verschränkung für beliebige Quantenmaterie berichtet wurden. Wie wir zeigen, erreicht unsere Schnittstelle nahezu den optimalen Kompromiss zwischen der Wahrscheinlichkeit, dass ein Photon in die Resonatormode emittiert wird und der Wahrscheinlichkeit dass es durch den Ausgangsspiegel austritt. Darüber hinaus wird gezeigt, dass die Schnittstelle an der theoretischen Effizienzgrenze arbeitet, so dass keine statistisch signifikanten Verbesserungen der Effizienz erzielt werden können, ohne Eigenschaften des Atoms oder des Resonators zu verändern. Dieses Ergebnis zeigt deutlich die Parameterbereiche auf, auf die man sich für künftige Verbesserungen konzentrieren sollte, und bietet einen Leitfaden für das Design allgemeiner, Effizienz-optimierter Emitter-Resonator-Systeme.

Ein weiteres Ergebnis dieser Arbeit ist die Verschränkung zwischen Ion und Photon über eine 50 km lange Glasfaser. Eine Schlüsselkomponente ist dabei die Umwandlung der Wellenlänge des Photons in das Telekommunikationsband bei 1550 nm, unter Bewahrung der Ionen-Photonen-Verschränkung. Die erreichte Entfernung übertrifft den bisherigen Rekord für Licht-Materie-Verschränkung um zwei Größenordnungen und stellt bereits eine praktische Entfernung für den Aufbau von Langstrecken-Quantennetzwerken dar.

Bei der Verteilung von Licht-Materie-Verschränkung sind sowohl eine hohe Effizienz als auch eine große Entfernung Schlüsseleigenschaften geplanter Quantennetzwerke. Die Spitzenwerte beider Parameter, die in dieser Arbeit erreicht werden, zeigen deutlich, dass gefangene Ionen, die an optische Resonatoren gekoppelt sind, dazu geeignet sind, als Knotenpunkte in Quantennetzwerken zu fungieren.

# PUBLICATIONS

The work presented in this thesis has led to the following journal publications:

- J. Schupp, V. Krcmarsky, V. Krutyanskiy, M. Meraner, T. E. Northup, and B. P. Lanyon. "Interface between Trapped-Ion Qubits and Traveling Photons with Close-to-Optimal Efficiency." In: *PRX Quantum* 2.2 (2021), p. 020331. DOI: 10.1103/PRXQuantum.2.020331.

- V. Krutyanskiy*, M. Meraner*, J. Schupp*, V. Krcmarsky, H. Hainzer, and B. P. Lanyon. "Light-matter entanglement over 50 km of optical fibre." In: *npj Quantum Information* 5.1 (2019), p. 72. DOI: 10.1038/s41534-019-0186-3.
  (*These authors contributed equally.)

Additional papers have been published in the framework of this thesis, but do not directly form part of it:

- M. Meraner, A. Mazloom, V. Krutyanskiy, V. Krcmarsky, J. Schupp, D. A. Fioretto, P. Sekatski, T. E. Northup, N. Sangouard, and B. P. Lanyon. "Indistinguishable photons from a trapped-ion quantum network node." In: *Physical Review A* 102.5 (2020), p. 052614. DOI: 10.1103/PhysRevA.102.052614.

- V. Krutyanskiy, M. Meraner, J. Schupp, and B. P. Lanyon. "Polarisation-preserving photon frequency conversion from a trapped-ion-compatible wavelength to the telecom C-band." In: *Applied Physics B* 123.9 (2017), p. 228. DOI: 10.1007/s00340-017-6806-8.

# ACKNOWLEDGEMENTS

This thesis would not have been possible without the support and contribution of countless people. Here, I want to express my gratitude to all and in the following mention at least some of them.

I would like to thank Ben Lanyon for taking me on as the first PhD student on his new and exciting project; for the enriching time, the close work together, his clear communication and constant availability, for sharing his excitement, enthusiasm and clear grasp of physics; and for giving me the feeling of being well taken care of and always having my back.

I thank Rainer Blatt for allowing me to be part of this outstanding scientific environment and wonderful group that he has shaped and sustained here in Innsbruck. It's unlikely that this project would have succeeded the way it has anywhere else in the world.

I am grateful to my team and the whole Blatt group. The friendships I made and the support I received made the whole thing worthwhile and helped me to continue also during the more challenging periods. In particular Martin Meraner, who was with me from the start, and the other OGs of my team Victor Krutyanskiy, Vojtech Krcmarsky and Helene Hainzer, who shared with me in all the joys and frustration that are part of the process. My appreciation goes to Daniel Heinrich, Klemens Schüppert, Martin van Mourik, Milena Guevara-Bertsch, Konstantin Friebe, Christine Maier, and all the others from whom I received some help now and then, for the discussions, the enjoyable times and for generally brightening my days. I'm also happy that the experiment is now in the capable hands of Marco Canteri, James Bate and Armin Winkler.

I thank Tracy Northup for her detailed input to the main paper and chapters of this thesis. Moreover, the know-how we received from her and the CQED team constitutes an invaluable contribution to the design, construction and understanding of the experiment.

Building the experimental setup would not have been possible without the guys of the mechanical and electronic workshop, Stefan Haslwanter, Andreas Strasser, Bernhard Öttl and Gerhard Hendl. Many thanks to Stefan in particular, who went out of his way to design and manufacture many of the core parts of the setup, teaching me some workshop lore on the way.

I would also like to thank the administrative staff, without whom nothing would go: Elisabeth Huck, Klaus Falschlunger, Valentin Staubmann and Markus Knabl on the IQOQI side, and Patricia Moser at the University.

Finally, I want to thank my family, especially my partner Melanie, for their encouragement, their constant support and their love.

# CONTENTS

# LIST OF FIGURES

## LIST OF TABLES



## ACRONYMS

AOM acousto-optic modulator

APD avalanche photodiode

AR anti-reflection

ASR anti-Stokes Raman

BS beam splitter

CCD charge-coupled device
CMRT cavity-mediated Raman transition
DDS direct digital synthesiser
ECDL external-cavity diode laser
EM CCD electron multiplying charge-coupled device
EOM electro-optic modulator
FPGA field-programmable gate array
FSR free spectral range
FWHM full width at half maximum
HWP half-wave plate
NEG non-evaporable getter
PBS polarising beam splitter
PDH Pound-Drever-Hall
PID proportional-integral-derivative
PM polarisation-maintaining
PMT photomultiplier tube
PPLN periodically poled Lithium Niobate
QED quantum electrodynamics
QIP quantum information processing
QWP quarter-wave plate
RF radiofrequency
RMS root mean square
ROC radius of curvature
SHG second harmonic generation
SHV secure high voltage
SM singlemode
SNSPD super-conducting nano-wire single-photon detector
TA tapered amplifier
Ti:Sa Titanium-Sapphire
UHV ultrahigh vacuum
UIBK University of Innsbruck
ULE ultralow expansion
UV ultraviolet
WLM wavelength meter

# Part I

# INTRODUCTION AND THEORY

# 1 INTRODUCTION

Information is arguably one of the most important resources at present. The information age that we live in is governed by the modern computer and the internet, bringing unprecedented possibilities for the acquisition, processing and distribution of information. Key innovations that paved the way for today's technology[1] were made in the wake of new insights into nature due to the advent of quantum mechanics at the turn of the last century. Today, that era is known as the *first quantum revolution*: the quantum mechanical revolution of our understanding of the structure and properties of matter, which led to "[...] a technological revolution, at the root of our information-based society" [2].

In present-day research, fundamentally new ways to encode and manipulate information are at the root of a movement that researchers themselves like to refer to as the *second quantum revolution* [3]. During the first quantum revolution, quantum-mechanical principles like superposition and entanglement were discovered. In the second quantum reovolution, these principles are seen as key resources for new concepts in information processing and communication. The classical bit, which is either "0" or "1", is replaced by the quantum bit—the *"qubit"*—which can take on arbitrary superpositions of the quantum states $|0\rangle$ and $|1\rangle$. Accordingly, the classical electronic "on/off" signal of, e.g., a transistor is replaced by a quantum object in which a qubit can be encoded, e.g., in the electronic states of an atom or the polarisation states of a photon.

Based on these principles, proposals for *quantum information technologies* have emerged, advertising powerful new tools for the processing and distribution of information. For example, envisioned quantum computers [4, 5] could be used to simulate other quantum systems [6] or perform certain computational tasks in a much more efficient way than their classical counterpart [7, 8]. In the field of communication, quantum cryptography [9] could enable fundamentally secure communication between remote locations.

The development of *interfaces* between travelling photons and quantum matter is one of the key requirements for emerging quantum technologies, allowing for single photon sources [10] and the transfer, storage and redistribution of quantum information [11]. If the quantum matter is a register of qubits with quantum processing capabilities, then more powerful applications become possible, such as scalable

1 A prominent example here is the invention of the transistor [1], the most elementary component of the modern computer, in 1948.

quantum computing [12] and arbitrary-distance quantum networks [13, 14] for secure communication [9], distributed quantum sensing [15] and enhanced timekeeping [16].

The efficiency of a photon-matter interface—the probability with which photons can be collected from or absorbed by matter qubits—is a key parameter to optimise for the practical realisation of the aforementioned quantum technologies. Paths to deterministic interfaces include collective effects in interacting particle ensembles [17] or optical resonators that exploit vacuum-modification effects to enhance emission into and absorption from a desired optical mode, e.g., Fabry-Pérot cavities [18], micro-resonators [19, 20] and nano-photonic waveguides [21, 22].

Efficient photonic interfaces for trapped-ion qubits are desirable: the deterministic, near fault-tolerant and multiqubit quantum-information-processing capabilities of the ion-trap platform [23–26] could enable arbitrary-distance quantum networking via the repeater approach [27, 28] and scalable quantum computing [12]. Furthermore, trapped ions are amongst the most precise sensors [29] and clocks [30] ever developed and could be used to construct distributed networks of quantum-limited sensors.

Combining trapped ions with high numerical aperture lenses is a powerful approach to connecting the quantum states of trapped-ion qubits to travelling photons. Using this approach, ions in separate traps have been entangled over a distance of ~1 m [31, 32]. Moreover, single photons on demand, emitted by and entangled with a trapped-ion qubit, have been generated and detected with a total probability of 0.024 after collection via an in-vacuum lens [33].

The first use of an optical cavity for the enhanced collection of ion-entangled photons achieved a combined probability for generation and detection—in the following simply called detected probability—of 0.057(2) [34]. Ion-entangled photons were recently collected using a microscopic fibre cavity, with a detected probability of $2.5 \times 10^{-3}$ [35].

As a first key result, this thesis describes the design, construction and characterisation of an ion-photon interface with an improved efficiency. Using this interface, photons entangled with the ion are obtained with a probability of 0.69(3) at the cavity output and are detected with a probability of 0.462(3). The latter value constitutes a fivefold increase over the previous best performance of 0.057(2) [34], obtained with another ion-cavity system in Innsbruck [36].

As a second key result of this thesis, it is shown that the probability with which photons are obtained at the cavity output could not be significantly higher without changing properties of our cavity or quantum emitter. Specifically, the performance of the system saturates theoretical limits on the photon collection efficiency from an emitter-cavity system [37], set only by the cavity parameters and electronic structure of the quantum emitter. These first two key results,

published in Ref. [38], provide clear paths for future improvements in the efficiency of photon-emitter interfaces.

As a third key result and as an application of the newly built interface, this thesis describes the distribution of ion-photon entanglement over 50 km of optical fibre. This result was published in Ref. [39]. For that experiment, the ion-cavity interface is combined with a frequency conversion stage [40] which converts the ion-entangled photons to telecom wavelength (1550 nm), the wavelength that suffers the lowest absorption in optical fibre. The construction and characterisation of the frequency conversion setup is part of the PhD work of Martin Meraner [41], carried out in parallel to the work described in this thesis.

This thesis is structured as follows: In Ch. 2 the theoretical framework for the description of photon generation in the context of cavity quantum electrodynamics (QED) is introduced, including the theoretical efficiency limits mentioned above. In Ch. 3 the implementation of the model described in Ch. 2 is discussed within the framework of the $^{40}Ca^{+}$ ion. The protocols for the generation of single photons and ion-photon entanglement in $^{40}Ca^{+}$ are presented, based on the works of Refs. [42] and [34], respectively. In Ch. 4 the experimental apparatus is described, including the design and construciton of the cavity, as well as details about the ion trap, vacuum chamber, laser systems, photon detection setups and experiment control. In Ch. 5 some key methods employed in this thesis are described, including the mapping of the intra-cavity field with an ion in order to determine the ion's location in the field. Further methods concern the preparation of the experiment and characterisation of experimental parameters, as well as the analysis of experimental results. In Ch. 6 the efficiency limits of the interface are experimentally investigated. The results include the improved efficiencies mentioned above as well as a discussion of the system performance in the light of the efficiency limits introduced in Ch. 2. In Ch. 7 the experiment and experimental results for the distribution of ion-photon entanglement over 50 km are presented and discussed. The chapter includes a brief overview of the employed method for photon frequency conversion, used to convert the photon's wavelength to 1550 nm. Finally, Ch. 8 concludes the thesis with a summary and provides an outlook to future experiments.

# 2 THEORY

What is the maximum efficiency with which a photon can be collected from a quantum emitter? Ideal optical resonators, if they existed, would allow for deterministic interfacing between light and matter (a model system is sketched in Fig. 2.1). The efficiency of real systems, however, is limited by finite emitter-resonator coupling strengths and unavoidable resonator loss. In this chapter, the basic concepts and theory of single-photon generation in the context of resonator (cavity) QED are introduced. First, a theoretical framework is presented for describing the coupling between a quantised emitter, which we will interchangeably refer to as "atom", and an optical Fabry-Pérot cavity that enhances photon emission into a desired optical mode. In the second part of this chapter, theoretical efficiency limits to photon generation are introduced which underpin the main results of this thesis.

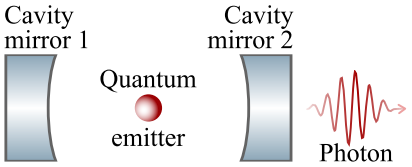


Fig. 2.1: **Photon collection with an optical cavity.** The model for photon collection described in this chapter is based on a (single) quantum emitter coupled to an optical resonator. The resonator (or cavity) consists of two mirrors and enhances photon emission into a desired optical mode.

## 2.1 COUPLING ATOMS AND CAVITIES

This section starts with a summary of relevant parameters of optical cavities, after which the basic aspects of cavity QED are introduced for a system consisting of a two-level atom interacting with the quantised electromagnetic field of an optical resonator (cavity). A more detailed treatise on the properties of cavities can be found in Ref. [43]; for basic information on the formalism of quantum mechanics, field quantisation and cavity QED, the reader is referred to Refs. [44, 45].

### 2.1.1 *Optical cavities*

Consider a Fabry-Pérot cavity consisting of two mirrors that are separated by a length $l$. Resonances occur for light undergoing constructive interference after one round trip. The resonance frequencies are sep-

arated by integer multiples of the cavity's free spectral range (FSR) $\Delta\nu_{FSR}$, given by the inverse round-trip time $t_{RT}$ of light travelling in the cavity at speed $c$:

$$\Delta\nu_{FSR} = \frac{1}{t_{RT}} = \frac{c}{2l}. \tag{2.1}$$

With this, resonances occur at frequencies $\nu_q = q\Delta\nu_{FSR} + \text{const.}$, where the integer $q$ denotes the axial mode number and the constant is due to the mirror curvature which is introduced later.

The mirrors, denoted 1 and 2 (Fig. 2.1), are characterised by their transmission, reflection and loss coefficients (of intensity), $T_i$, $R_i$ and $L_i$, respectively, with $i \in \{1, 2\}$. Here, $L_i$ corresponds to loss due to absorption and scattering in the mirrors. Energy conservation dictates that $T_i + R_i + L_i = 1$. We define the total cavity round-trip loss as $\mathscr{L} = T_1 + T_2 + L_1 + L_2$. The quality of the cavity is characterised by its finesse

*Cavity finesse*

$$\mathcal{F} = \frac{\pi(R_1R_2)^{1/4}}{1-\sqrt{R_1R_2}} \approx \frac{2\pi}{\mathscr{L}}, \tag{2.2}$$

where the approximation holds for $1 - R_1 \ll 1$ and $1 - R_2 \ll 1$ [46], as is the case in this work. Around a resonance, the spectral transmission profile is Lorentzian with a linewidth [full width at half maximum (FWHM)] of

$$\Delta\nu_c = \frac{\Delta\nu_{FSR}}{\mathcal{F}} = \frac{2\kappa}{2\pi}, \tag{2.3}$$

where $\kappa$ is the decay rate of the cavity field, defined only by the total cavity loss and its length.

If spherically curved mirrors are used, as in this work, the cavity eigenmodes are restricted to geometrically stable Hermite-Gauss (or Laguerre-Gauss) modes. In the case of both mirrors having the same radius of curvature (ROC) $R_C$, the resonance frequencies of axial-plus-transverse modes in the cavity are given by

$$\nu_{qmn} = \Delta\nu_{FSR}\left[(q+1) + \frac{(m+n+1)}{\pi}\arccos\left(1 - \frac{c}{2\Delta\nu_{FSR}R_C}\right)\right], \tag{2.4}$$

where $m$ and $n$ specify the transverse-mode indices of a Gauss $TEM_{qmn}$ (transverse electromagnetic) mode. The frequency spacings $\Delta\nu_{mn}$ between adjacent transverse modes will be of practical interest for the cavity characterisation presented in Sec. 4.1.1.

In order to allow for the maximum possible interaction strength between atom and cavity (see Sec. 2.2), the atom is coupled to a $TEM_{00}$ mode[1]. We therefore restrict the discussion in the rest of this chapter

1 The value of the axial mode index $q$ is of no practical interest and is usually omitted.

to this mode. The smallest electric field radius[2] of this mode is called the waist, whose size is given by *Cavity waist*

$$w_0^2 = \frac{\lambda}{2\pi}\sqrt{l(2R_C - l)} \tag{2.5}$$

for a wavelength $\lambda$. At a distance $z$ from the waist[3] along the optical axis, the mode radius is calculated as

$$w(z) = w_0\sqrt{1 + (z/z_R)^2}, \tag{2.6}$$

with the Rayleigh range $z_R = \pi w_0^2/\lambda$. The spatial distribution of the electric-field standing-wave inside the cavity $E_{cav}$ has the following dependency:

$$E_{cav}(\mathbf{r}) \propto \cos(kz)\frac{w_0}{w(z)}e^{-(x^2+y^2)/w(z)^2}, \tag{2.7}$$

where $k = 2\pi/\lambda$ is the wave number.[4] With this, we can define the mode volume as

$$V = \int |E_{cav}|^2 d\mathbf{r} = \frac{\pi}{4}w_0^2 l = A_{eff} l, \tag{2.8}$$

where we have introduced the effective mode area $A_{eff} = \frac{\pi}{4}w_0^2$. As we will see later, the mode volume is the only cavity parameter that determines the interaction strength between atom and cavity, and $A_{eff}$ is a key parameter on which the efficiency of photon collection by the cavity depends.

In order to understand the interactions between single photons and single atoms, it is necessary to consider a quantized description of the electromagnetic field [45]. The single-mode field of the cavity can be treated as a quantum harmonic oscillator with resonance frequency $\omega_C = 2\pi c/\lambda$. The Hamiltonian of the cavity, written in terms of the annihilation operator $a$ and creation operator $a^\dagger$, is given by:

$$H_C = \hbar\omega_C\left(a^\dagger a + \frac{1}{2}\right). \tag{2.9}$$

The quantum-mechanical state vector of the cavity mode is then generally described by a superposition of photon number states, the so-called Fock states $|n\rangle$. Each photon of a mode carries an energy $\hbar\omega_C$.

2 The radius is defined as the distance from the optical axis where the electric field strength has dropped to $1/e$ of its on-axis value.

3 Throughout this thesis, depending on the context, the term "waist" is used to signify both the smallest radius $w_0$ and its location.

4 Of course, the electric field does not necessarily take a maximum value of the cosine function at the waist ($z = 0$). Eq. (2.7) is an (excellent) approximation based on the fact that the paraxial approximation is generally assumed throughout this thesis, implying $z_R \gg \lambda$.

For $n$ photons in the cavity, the total energy is given by $\hbar\omega_C(n+1/2)$, with the zero-point energy $\hbar\omega_C/2$.

Note that the description using a Hamiltonian does not, generally, contain losses. In a real optical cavity, all photon states that are populated in the cavity, e.g., due to photons emitted by an atom into the cavity mode, decay due to, e.g., transmission out of the cavity or scattering and absorption loss. This dissipation to the environment is treated later in this chapter.

### 2.1.2 *Two-level atom coupled to a cavity*

For an atom with ground state $|g\rangle$ of energy $\hbar\omega_g$ and excited state $|e\rangle$ of energy $\hbar\omega_e$, the Hamiltonian is given by

$$H_A = \hbar\omega_g\sigma_{gg} + \hbar\omega_e\sigma_{ee}, \quad \text{with} \quad \sigma_{ij} = |i\rangle\langle j|. \tag{2.10}$$

The coupling strength between the atomic dipole $\mu_{ge}$ and the vacuum field of a cavity $\vec{E}_{vac}$ surrounding the atom is given by the vacuum Rabi frequency

$$g = \frac{\vec{\mu}_{ge}\cdot\vec{E}_{vac}}{\hbar}. \tag{2.11}$$

With the vacuum electric-field amplitude $E_{vac,0} = \sqrt{\hbar\omega_C/(2\epsilon_0 V)}$ [45], the atom-cavity coupling strength at an antinode of the cavity standing wave can be written as

*Atom-cavity coupling strength*

$$g = \sqrt{\frac{4\mu_{ge}^2 c}{\epsilon_0\hbar w_0^2 l\lambda}}\zeta = \sqrt{\frac{c\gamma_g}{2l\widetilde{A}_{eff}}}\zeta, \tag{2.12}$$

for a cavity of length $l$ and with $\widetilde{A}_{eff} = \frac{A_{eff}}{\sigma}$. The factor $\zeta \leqslant 1$ is introduced to account for the projection of the cavity polarisation onto the atomic dipole moment, as discussed further in Sec. 3.2. The right-hand side of Eq. (2.12) is obtained by writing the dipole moment as [37]

$$\mu_{ge}^2 = \frac{\gamma_g 6\epsilon_0\hbar\lambda^3}{8\pi^2}. \tag{2.13}$$

For a closed system, in which energy is preserved, an atom in the ground state is excited by absorbing a single photon from the cavity and an atom in the excited state will be transferred to the ground state by emitting a photon into the cavity mode. The interaction Hamiltonian is therefore given by

$$H_{int}^{cav} = \hbar g[\sigma_{eg}a + a^\dagger\sigma_{ge}], \tag{2.14}$$

where the absorption (emission) of a photon is represented by the annihilation operator $a$ (creation operator $a^\dagger$). The complete Hamiltonian is $H^{(2)} = H_A + H_C + H_{int}^{cav}$, which is usually referred to as the Jaynes-Cummings Hamiltonian [47]. Note that the formal derivation of the interaction Hamiltonian (2.14) relies on both the dipole approximation and rotating wave approximation [44].[5]

The ground state of the system is trivially given by $|g,0\rangle = |g\rangle \otimes |0\rangle$, the atom in the ground state and no photon in the cavity. For a given number of excitation quanta (photons) $n > 0$ in the system, the atom-cavity coupling leads to pairs of non-degenerate eigenstates, the so-called dressed states. These states are given by $|\pm, n\rangle = \sqrt{1/2}(|g,n\rangle \pm |e,n-1\rangle)$ and have an energy splitting $2g$.[6] An excited atom in a vacuum mode of a cavity will undergo oscillations between the states $|e,0\rangle$ and $|g,1\rangle$ at frequency $2g$, hence the term vacuum Rabi frequency.

In order to include dissipation to the environment in the description of the system, the master equation formalism can be used (see, e.g., Ref. [44] Ch. 15.4). Here, dissipative processes are modelled via collapse operators $L_j$ (so-called Lindblad operators) which describe the coupling of the system to a reservoir of empty modes. The system is then described via its density matrix $\rho$ with the master equation in Lindblad form:

$$\begin{aligned} &\frac{d\rho}{dt} = -\frac{i}{\hbar}[H,\rho] - \mathcal{L}[\rho] \\ \text{with} \qquad &\mathcal{L}[\rho] = -\frac{1}{2}\sum_j \left(2L_j\rho L_j^\dagger - \rho L_j L_j^\dagger - L_j^\dagger L_j \rho\right), \end{aligned} \tag{2.15}$$

where the Liouvillian $\mathcal{L}[\rho]$ describes the non-unitary evolution of the system due to its coupling to the reservoir and is responsible for irreversible dissipation. The master equation can be rewritten as

$$\begin{aligned} &\frac{d\rho}{dt} = -\frac{i}{\hbar}[H_{eff},\rho] + \sum_j L_j\rho L_j^\dagger \\ \text{with} \qquad &H_{eff} = H - \frac{i\hbar}{2}\sum_j L_j^\dagger L_j, \end{aligned} \tag{2.16}$$

where $H_{eff}$ is the effective non-Hermitian Hamiltonian describing nonunitary evolution. In the following discussion, two dissipative

5 In short, the dipole approximation assumes that the size of the atom is much smaller than the wavelength of the electromagnetic field, such that the amplitude of the field can be considered constant across the extent of the atom. In the rotating wave approximation, terms proportional to $a\sigma$ and $a^\dagger\sigma^\dagger$ are neglected in the full interaction Hamiltonian $\hbar(a + a^\dagger)(g\sigma^\dagger + g^*\sigma)$. The time evolution of these terms is of the form $e^{\pm i(\omega_{ge}+\omega_C)t}$. Rotating at twice an optical frequency, these terms quickly average out to zero on a timescale which is dominated by the evolution of the other terms evolving with $e^{\pm i(\omega_{ge}-\omega_C)t}$ (the condition $|\omega_{ge} - \omega_C| \ll \omega_{ge}, \omega_C$ is assumed). For further details, see Ref. [44], Chapters 3 and 14.

6 Resonant interaction between cavity and atom is assumed.

processes are of importance: spontaneous emission from the atom at rate $2\gamma$, which is represented by the operator $L_A = \sqrt{2\gamma}\sigma_{ge}$, and decay from the cavity mode at rate $2\kappa$, which is represented by $L_C = \sqrt{2\kappa}a$. The effective Hamiltonian is then given by $H_{\text{eff}} = H_{\text{int}}^{(2)} - i\hbar(\gamma\sigma_{ee} + \kappa a^\dagger a)$, where only the interaction part is taken into account now and cavity and atom are considered to be on resonance.

The system dynamics can be analysed by solving the time-dependent Schrödinger equation

$$i\hbar|\dot{\psi}\rangle = H_{\text{eff}}|\psi\rangle\,. \tag{2.17}$$

For the state $|\psi\rangle = c_e|e,0\rangle + c_g|g,1\rangle$ with time-dependent coefficients $c_{e,g}$ and with the atom initially in the excited state [$c_e(0) = 1$, $c_g(0) = 0$], the following system of differential equations is obtained:

$$\begin{pmatrix}\dot{c}_e\\ \dot{c}_g\end{pmatrix} = -\begin{pmatrix}\gamma & ig\\ ig & \kappa\end{pmatrix}\begin{pmatrix}c_e\\ c_g\end{pmatrix}. \tag{2.18}$$

Different regimes can be distinguished from these equations, depending on the relative strengths of $g, \kappa, \gamma$. In the *"strong coupling regime"*, with $g \gg (\kappa, \gamma)$, the system dynamics are dominated by vacuum Rabi-oscillations and the system is best described in the basis of the dressed states mentioned above [44].

Another regime can be characterised by $\kappa \gg g$. Here, vacuum Rabi-oscillations are inhibited by the strong damping of the one-photon state in the cavity: the photon is emitted from the cavity before it can be re-absorbed by the atom. The transient population of the state $|g,1\rangle$ is negligible and the adiabatic approximation $\dot{c}_g \approx 0$ yields [48, 49]

$$\dot{c}_e = -\tilde{\gamma}c_e, \quad \text{i.e.,} \quad c_e(t) = \exp(-\tilde{\gamma}t) \quad \text{with} \quad \tilde{\gamma} = \gamma + \frac{g^2}{\kappa}. \tag{2.19}$$

*Purcell effect*

The excited atom decays exponentially with a rate that is enhanced by the presence of the cavity. This is the so-called Purcell effect [50].

It is interesting to look at the ratio of the probability $P_{|g,1\rangle}$ for being in state $|g,1\rangle$ and the probability $P_{|e,0\rangle}$ for being in the excited state [48]: $P_{|g,1\rangle}/P_{|e,0\rangle} = g^2/\kappa^2$ (the condition $\dot{c}_g = 0$ is still assumed). Disregarding internal losses of the cavity, like absorption and scattering in the mirrors, the state $|g,1\rangle$ decays with a rate $2\kappa$ by emitting a photon from the cavity. On the other hand, the state $|e,0\rangle$ spontaneously decays with a rate $2\gamma$ into free space. The ratio of the probability for emission from the cavity into the output mode $P_S$ and the probability for spontaneous emission into free space $P_{\text{loss}}^{\text{atom}}$ is therefore given by

$$\frac{P_S}{P_{\text{loss}}^{\text{atom}}} = \frac{2\kappa P_{|g,1\rangle}}{2\gamma P_{|e,0\rangle}} = \frac{g^2}{\kappa\gamma}. \tag{2.20}$$

This is the Purcell factor, which is twice the one-atom cooperativity parameter

*Cooperativity*

$$C = \frac{g^2}{2\kappa\gamma}. \tag{2.21}$$

Still ignoring internal cavity loss, and assuming that either a photon is emitted from the cavity into the output mode or lost due to spontaneous atomic decay, i.e., $P_S + P_{\text{loss}}^{\text{atom}} = 1$, we can determine the success probability for collecting a photon in the cavity output in the case of a two-level atom:

$$P_S = \frac{2C}{1+2C} \tag{2.22}$$

This relation is usually derived for the so-called *"bad cavity"* or *"Purcell"* regime, which is characterised by $\kappa \gg g^2/\kappa \gg \gamma$. Note, however, that only the condition $\dot{c}_g = 0$ was necessary in deriving the relation, suggesting that it is a bound which can also be applied outside the bad-cavity regime [48]. Indeed, using the same condition and similar considerations, an upper bound on the photon-collection probability will be presented in the next section for an atom with more than two levels, in the presence of internal cavity loss, and independent of the coupling regime.

## 2.2 SINGLE PHOTONS FROM ATOM-CAVITY SYSTEMS

Generating single photons with a two-level atom requires exciting the atom, e.g., via a resonant laser pulse or rapid adiabatic passage. However, upon emission of a photon, the atom will revert back to the ground state and another photon can potentially be generated before the laser pulse is switched off. Many atom-based photon-generation schemes therefore rely on a three-level configuration with distinct initial and final atomic states, where only one photon is ever generated per laser pulse [18, 37, 49, 51]. In this section, a model of a three-level atom coupled to a cavity and driven by a laser is introduced and the presence of internal cavity loss is treated explicitly. Upper bounds on the probability for generating single photons in the context of the model will be presented. These upper bounds, or figures of merit, were derived in Ref. [37] and will be discussed with inspiration taken from Refs. [48, 51]. They will serve as reference points throughout this thesis and will be compared against experimental data and numerical simulations in a later chapter. The section concludes with an overview of the cavity-mediated Raman transition (CMRT), which is the particular photon generation scheme employed in this thesis.

### 2.2.1 *Three-level atom in a cavity*

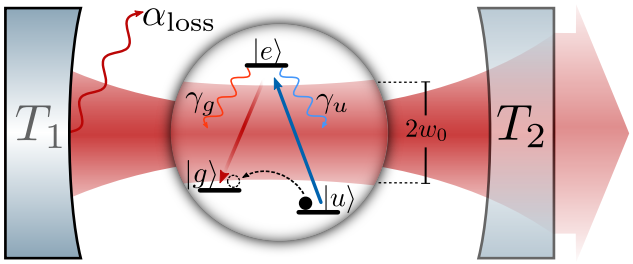


Fig. 2.2: **Three-level atom in a cavity.** A three-level atom in the waist with radius $w_0$ of a vacuum mode of a cavity formed by two mirrors with transmission coefficients $T_1$ and $T_2$. The unwanted cavity loss per round-trip $\alpha_{\text{loss}}$ includes $T_1$. The $|u\rangle \leftrightarrow |e\rangle$ transition is driven by an external field (blue arrow) with coupling strength $\Omega$. The $|g\rangle \leftrightarrow |e\rangle$ transition is coupled to the cavity (red arrow) with coupling strength $g$. For the generation of photons, the system is initialised into the state $|u, 0\rangle$, where $|0\rangle$ is the vacuum Fock state of the cavity. Emission of a photon into the cavity leaves the system in $|g, 1\rangle$. Spontaneous decay from $|e, 0\rangle$ to $|g, 0\rangle$ with decay constant $\gamma_g$ ends the attempt in failure, whereas decay from $|e, 0\rangle$ to $|u, 0\rangle$ with decay constant $\gamma_u$ allows for subsequent cavity photon generation (re-initialisation events). This figure has been reproduced from Fig. 1 of Ref. [38].

COHERENT INTERACTION: Consider a three-level atom in a $\Lambda$-type configuration with two ground states, $|u\rangle$ and $|g\rangle$, and one excited state $|e\rangle$. The atom is located at the position of the waist $w_0$ [Eq. (2.5)] of a cavity formed by two mirrors with transmission values $T_1$ and $T_2$, as illustrated in Fig. 2.2. The output mode of the cavity is the free-space spatial mode that couples to the cavity via the mirror with transmission $T_2$. The $|e\rangle \leftrightarrow |g\rangle$ transition with frequency $\omega_{ge} = \omega_e - \omega_g$ and absorption cross-section $\sigma = 3\lambda^2/(2\pi)$ [52] at wavelength $\lambda = 2\pi c/\omega_{ge}$, is coupled by a vacuum mode of the cavity. The $|u\rangle \leftrightarrow |e\rangle$ transition with frequency $\omega_{ue} = \omega_e - \omega_u$ is driven by an external drive field of frequency $\omega_d$ with Rabi frequency $\Omega$. We introduce the cavity and drive-field detunings $\Delta_C = \omega_{ge} - \omega_C$ and $\Delta_d = \omega_{ue} - \omega_d$. The system Hamiltonian is composed of the energy of the free atom ($H_A = \sum \hbar\omega_i \sigma_{ii}, i \in \{u, e, g\}$), the energy of the cavity $H_C$ [Eq. (2.9)], the interaction term due to the cavity $H_{\text{int}}^{\text{cav}}$ [Eq. (2.14)] and an interaction term due to the coupling of the atom to the drive laser $H_d = \hbar\Omega/2(\sigma_{eu}e^{i\omega_d t} + \sigma_{ue}e^{-i\omega_d t})$. Again, the dipole approximation and rotating wave approximation[7] are assumed. Choosing the zero-

7 Here, not only terms rotating at twice an optical frequency ($2\omega_C$, $2\omega_d$, $\omega_C + \omega_d$) are neglected, but also terms rotating at $\omega_C - \omega_d$ [48]. This is justified under the assumption $\max\{2g, \Omega, |\Delta_C|, |\Delta_d|\} \ll |\omega_C - \omega_d|$, implying that cavity and drive field only couple to their respective transitions.

point energy to lie with the state $|g\rangle$, the Hamiltonian can be written as follows, in a frame rotating at the cavity and drive-field frequencies[8]:

$$H^{(3)} = \hbar\left[(\Delta_C - \Delta_d)\sigma_{uu} + \Delta_C\sigma_{ee} + g(\sigma_{eg}a + a^\dagger\sigma_{ge}) + \frac{\Omega}{2}(\sigma_{eu} + \sigma_{ue})\right]. \tag{2.23}$$

DISSIPATION: Using the formalism introduced in the previous section, we can now include dissipation channels in the model. The total cavity decay rate is given by

*Cavity decay rate*

$$\kappa = \kappa_{in} + \kappa_{ext} = \frac{c}{4l}(\alpha_{loss} + T_2), \tag{2.24}$$

where the internal decay rate $\kappa_{in} = \frac{c}{4l}\alpha_{loss}$ is determined by $\alpha_{loss}$, the unwanted cavity-loss probability per round trip. This unwanted cavity loss contains all photon-loss mechanisms in the cavity except for $T_2$, such as internal cavity loss due to absorption and scattering in the mirrors and transmission through the mirror with coefficient $T_1$. The external decay rate is $\kappa_{ext} = \frac{c}{4l}T_2$ and corresponds to wanted decay into the output mode.

The free-space spontaneous decay rates on the $|e\rangle \to |g\rangle$ and $|e\rangle \to |u\rangle$ transitions are given by $\gamma_g$ and $\gamma_u$, respectively. As an extension to the model, possibly existing ground states other than $|g\rangle$ and $|u\rangle$ to which the excited state $|e\rangle$ can decay are grouped in a fourth state $|o\rangle$; the corresponding decay rate is $\gamma_o$. The total decay rate of the excited state is therefore $\gamma = \sum_j r_j\gamma = \sum_j \gamma_j$, with $j \in \{g, u, o\}$ and $r_j$ the branching ratio of the transition $|e\rangle \to |j\rangle$. With the definition of $g$ in Eq. (2.12), the cooperativity [Eq. (2.21)] can now be expressed as

$$C = \frac{g^2}{2\kappa\gamma} = \frac{1}{\widetilde{A}_{eff}(\alpha_{loss} + T_2)}\frac{\gamma_g}{\gamma}\zeta^2, \tag{2.25}$$

independent of the cavity length and atomic dipole moment.

MASTER EQUATION: In analogy to the case of the two-level atom, the effective non-Hermitian Hamiltonian in the case of a three-level atom is given by

$$H_{eff}^{(3)} = H^{(3)} - i\hbar(\gamma\sigma_{ee} + \kappa a^\dagger a) \tag{2.26}$$

8 The Hamiltonian in a rotating frame $\tilde{H}$ is obtained from a Hamiltonian $H$ via the transformation $\tilde{H} = UHU^\dagger - A$, where $U = e^{iAt/\hbar}$ is a unitary operator generated by a Hermitian and time-independent operator $A$ (see, e.g., Ref. [45] Appendix C). Obtaining the Hamiltonian of Eq. (2.23) requires $A = (\omega_C - \omega_d)\sigma_{uu} + \omega_C(a^\dagger a + \sigma_{ee})$.

and the master equation is

$$\frac{d\rho}{dt} = -\frac{i}{\hbar}\left[H_{\text{eff}}^{(3)}, \rho\right] + 2\kappa_{\text{ext}} a\rho a^\dagger + 2\kappa_{\text{in}} a\rho a^\dagger + \sum_{j=g,u,o} 2\gamma_j \sigma_{je}\rho\sigma_{ej}. \tag{2.27}$$

Note that the coupling to the output mode can also be treated explicitly via an interaction Hamiltonian instead of the simple Lindblad operator $\sqrt{2\kappa_{\text{ext}}}a$ used here, as shown in Ref. [37]. While the explicit method has the advantage of allowing one to obtain an expression for the frequency spectrum of the emitted photon, the approach taken here is sufficient in order to shed light on the efficiency limits presented next.

PHOTON GENERATION: In order to generate an intra-cavity photon, the system is initialised in the state $|u, 0\rangle$, from which it is driven to $|g, 1\rangle$ via interaction with the drive laser for a duration T and interaction with the vacuum mode of the cavity. To begin with, we assume that any quantum jumps, i.e., atomic ($\gamma$) or cavity ($\kappa$) decay, lead to a loss from the three-level system described by the Hamiltonian $H^{(3)}$ of Eq. (2.23). The time evolution is then described by the non-Hermitian Schrödinger equation (2.17) [37], where the effective Hamiltonian $H_{\text{eff}}^{(3)}$ is given by Eq. (2.26). For the state $|\psi\rangle = c_u|u, 0\rangle + c_e|e, 0\rangle + c_g|g, 1\rangle$, the Schrödinger equation becomes

$$\begin{pmatrix} \dot{c}_u \\ \dot{c}_e \\ \dot{c}_g \end{pmatrix} = -\begin{pmatrix} i(\Delta_C - \Delta_d) & i\Omega/2 & 0 \\ i\Omega/2 & i\Delta_C + \gamma & ig \\ 0 & ig & \kappa \end{pmatrix} \begin{pmatrix} c_u \\ c_e \\ c_g \end{pmatrix}. \tag{2.28}$$

Successful photon collection consists in driving the system to the state $|g, 1\rangle$ (via emission of a photon into the cavity mode) and subsequent decay of the photon into the cavity output mode, i.e., decay of the state $|g, 1\rangle$ to $|g, 0\rangle$ at rate $2\kappa_{\text{ext}}$. The corresponding probability is given by

$$P_S^{\text{pure}} = 2\kappa_{\text{ext}} P_{|g,1\rangle} = 2\kappa_{\text{ext}} \int_0^T |c_g|^2 dt, \tag{2.29}$$

where the notation "pure" indicates the no-quantum-jump condition.

Starting from the master equation (2.27) and the Schrödinger equation (2.28), and making use of the expression for the collection probability (2.29), an upper bound on the photon collection probability is derived in Ref. [37]. This upper bound is independent of the drive strength $\Omega$ and the detunings $\Delta_{C,d}$. In the following subsection, this upper bound is presented and discussed; the reader is referred to Ref. [37] for details on its derivation. At the end of this chapter we will come back to Eq. (2.29) in order to determine the conditions under

which the upper bound can be achieved using our specific photon generation scheme.

### 2.2.2 *Efficiency limits of photon collection*

An important aspect of the three-level atom presented above is that quantum jumps on the $|e\rangle \rightarrow |u\rangle$ transition before a cavity photon has been generated do not lead out of the state space spanned by $|\psi\rangle$. Such quantum jumps re-initialise the atom in the state $|u, 0\rangle$ and the photon-generation process continues until the state vector becomes $|\psi\rangle = 0$. This means that, given a long enough time $T$, either a photon was successfully transmitted into the output mode or the photon-generation attempt failed due to internal cavity decay or spontaneous atomic decay, leaving the system in one of the states $|g, 0\rangle$ or $|o, 0\rangle$. Taking into account these *"re-initialisation events"*, an upper bound to the photon-collection probability $P_S$—the probability for obtaining a photon in the cavity output mode—is derived in Ref. [37]:

*Upper bound to the photon-collection probability ($P_S^{bound}$)*

$$P_S \leqslant P_S^{bound}, \qquad \text{with} \tag{2.30}$$

$$P_S^{bound} = \left(\frac{\kappa_{ext}}{\kappa}\right)\left(\frac{2C}{1+2C}\right)\sum_{m=0}^{\infty}\left(\frac{r_u}{1+2C}\right)^m. \tag{2.31}$$

As a reminder, $r_u = \gamma_u/\gamma$ is the atomic branching ratio to state $|u\rangle$ (see Fig. 2.2). The first term in brackets in Eq. (2.31) is the escape probability

$$P_{esc} = \frac{\kappa_{ext}}{\kappa} = \frac{T_2}{T_2 + \alpha_{loss}}, \tag{2.32}$$

i.e., the probability for a photon inside the cavity to escape to the output mode and not be lost due to the internal cavity loss. The product of the second term in brackets and the summation can be interpreted as the (internal) generation efficiency $P_{in}$—the probability for a photon to be emitted into the cavity mode—such that $P_S^{bound} = P_{esc}P_{in}$. Note that the second term in brackets corresponds to the collection efficiency $P_S$ derived in Sec. 2.1.2 for a two-level atom in the absence of internal cavity loss [Eq. (2.22)]. The terms with $m > 0$ in Eq. (2.31) arise due to the presence of the $|e\rangle \leftrightarrow |u\rangle$ transition driven by the laser: they are contributions to $P_{in}$ due to the re-initialisation events described above (spontaneous decay on the $|e\rangle \rightarrow |u\rangle$ transition preceding successful photon generation). These re-initialisation events lead to cavity output photons that are not transform-limited; that is, the summation over $m$ describes a mixture of wave packets in the temporal domain.

The upper bound on $P_S^{pure}$—the photon-collection probability without re-initialisation events—is calculated by setting $m = 0$ in Eq. (2.31). While we do not measure $P_S^{pure}$ in the experiment, we will revisit the

fraction of photons in the cavity output mode generated without prior spontaneous decay of the emitter: $P_S^{\text{pure}}/P_S$ (see Ch. 6). Note that the extent to which re-initialisation events are detrimental depends on what the photons are to be used for. While re-initialisation has no observable effect on the fidelity of our emitter-photon entanglement (Sec. 6.4), it will reduce the indistinguishability of the photons, as we have recently studied [53].[9]

DERIVATION OF $P_S^{\text{BOUND}}$: Achieving the upper bound given by Eq. (2.31), i.e., satisfying the equality in Eq. (2.30), requires the condition $\int_0^T |\dot{c}_g|^2 dt = 0$ [37]. Recall from Sec. 2.1.2 that the photon-collection probability for the two-level atom [Eq. (2.22)] was derived under the same condition. Indeed, by following the same intuitive considerations used for the two-level atom, an equivalent form of Eq. (2.31) may be obtained, as outlined in the following. Starting from the Schrödinger equation (2.28) and the condition $\int_0^T |\dot{c}_g|^2 dt = 0$, consider again the ratio of the probability $P_{|g,1\rangle}$ for being in state $|g,1\rangle$ and the probability $P_{|e,0\rangle}$ for being in the excited state: $P_{|g,1\rangle}/P_{|e,0\rangle} = g^2/\kappa^2$. The state $|g,1\rangle$ decays with a rate $2\kappa_{\text{ext}}$ by emitting a photon from the cavity into the output mode. While the state $|e,0\rangle$ spontaneously decays with a rate $2\gamma$ into free space, only the part $\gamma_{\text{loss}} = \gamma_g + \gamma_o = \gamma - \gamma_u$ leads to an atomic state that is decoupled from the photon generation process [48]. The ratio of the probability for collecting a photon in the cavity output mode $P_S$ and the loss probability due to spontaneous emission into free space $P_{\text{loss}}^{\text{atom}}$ is therefore given by

$$\frac{P_S}{P_{\text{loss}}^{\text{atom}}} = \frac{2\kappa_{\text{ext}} P_{|g,1\rangle}}{2\gamma_{\text{loss}} P_{|e,0\rangle}} = \frac{\kappa_{\text{ext}}}{\kappa} \frac{g^2}{\kappa(\gamma - \gamma_u)}.$$

Taking into account internal cavity decay, which occurs with a probability $P_{\text{loss}}^{\text{cav}} = 2\kappa_{\text{in}} P_{|g,1\rangle}$, the condition $P_S + P_{\text{loss}}^{\text{atom}} + P_{\text{loss}}^{\text{cav}} = 1$ holds. With the definition of an effective cooperativity $C_{\text{eff}} = \frac{g^2}{2\kappa(\gamma-\gamma_u)}$, it is straightforward to arrive at $P_S = \frac{\kappa_{\text{ext}}}{\kappa} \frac{2C_{\text{eff}}}{1+2C_{\text{eff}}}$, which is equivalent to Eq. (2.31).[10]

OPTIMISED UPPER BOUND: The upper bound on the photon-collection probability [Eq. (2.31)] is maximised for the optimal output-mirror transmission [37]

$$T_2^{\text{opt}} = \alpha_{\text{loss}} \sqrt{1 + \beta \frac{1}{\alpha_{\text{loss}}} \frac{2}{\widetilde{A}_{\text{eff}}}}, \tag{2.33}$$

9 The results of Ref. [53] can also be found in the upcoming thesis of M. Meraner [41].
10 The sum in Eq. (2.31) yields the expression $(1+2C)/(1+2C-r_u)$.

with $\beta = \frac{\gamma_g}{\gamma-\gamma_u}\zeta^2$, yielding the optimised upper bound[11]

$$P_S^{opt} = 1 - \frac{2}{1+\sqrt{1+\beta\frac{1}{\alpha_{loss}}\frac{2}{\tilde{A}_{eff}}}}. \tag{2.34}$$

Excluding re-initialisation events, the optimised upper bound on $P_S^{pure}$ (the photon-collection probability without prior spontaneous decay to $|u\rangle$) is calculated by setting $\gamma_u = 0$, so $\beta = \frac{\gamma_g}{\gamma}\zeta^2$.

The existence of an optimal output-mirror transmission can be understood by considering that there is a tradeoff relation in Eq. (2.31) between the probability for photon emission into the cavity ($P_{in}$) and the escape probability ($P_{esc}$) with respect to $T_2$: while $T_2 > T_2^{opt}$ would increase the probability for a photon already inside the cavity to be transmitted to the output mode, it would reduce the probability of the photon being emitted into the cavity in the first place, and the opposite would be true for $T_2 < T_2^{opt}$.

This tradeoff relation needs to be considered when designing a new cavity-QED system for the generation of single photons: the output-mirror transmission $T_2$ needs to be chosen with respect to the values of $w_0$ and $\alpha_{loss}$ one expects to achieve. In other words: for a free choice of the transmission $T_2$, the cavity waist $w_0$ and unwanted photon loss $\alpha_{loss}$ are the only parameters that determine the efficiency of the atom-photon interface on a given atomic transition.

### 2.2.3 *Cavity-mediated Raman transition (CMRT)*

In theory, $P_S^{bound}$ can be achieved via one of several different drive schemes, e.g., resonant excitation, vacuum-stimulated Raman adiabatic passage (vSTIRAP) or cavity-enhanced Raman scattering [37]. Our drive scheme, which we call *cavity-mediated Raman transition (CMRT)*, is based on cavity-enhanced off-resonant Raman scattering. For a calcium ion coupled to a cavity, the scheme was first presented in Refs. [42, 54] and has further been employed in a number of works, e.g., Refs. [36, 55–57]. In this section, a brief summary of the key working principles is given and the conditions under which $\int_0^T |\dot{c}_g|^2 dt \approx 0$ is fulfilled, i.e., for which the efficiency converges towards the upper bound, will be analysed for our regime of cavity and atomic parameters.

In our system, spontaneous atomic decay is the dominant rate, i.e., $\gamma \gg g, \kappa$. In order to reduce the probability of spontaneous decay from the excited state $|e\rangle$ during the CMRT, a value for the detuning of the drive laser is chosen that is much greater than both the laser's drive strength $\Omega$ and the decay rate $\gamma$. In the case of drive laser

11 Eq. (2.34) corresponds to Eq. (34) in Ref. [37], but the latter is expressed in terms of the internal cooperativity $C_{in} = \frac{g^2}{2\kappa_{in}\gamma} = \frac{1}{\tilde{A}_{eff}\alpha_{loss}}\frac{\gamma_g}{\gamma}\zeta^2$. Eq. (2.34) follows directly from Eq. (34) in Ref. [37] by substituting $2C_{in}/(1-r_u) = 2\beta/(\tilde{A}_{eff}\alpha_{loss})$.

and cavity having the same detuning $\Delta$ from the excited state, the system is said to be on *Raman resonance* and population is ideally coherently transferred directly from initial state $|u, 0\rangle$ to state $|g, 1\rangle$, which includes the emission of a photon into the cavity. Under the condition $\Delta \gg (\gamma, \Omega, g)$, the description can be approximated by that of a two-level system involving atomic initial and final levels $|u\rangle$ and $|g\rangle$, respectively. The effective coherent coupling rate of this process is approximately given by [42]

*Coupling strength of the CMRT*

$$\Omega_{\text{eff}} = \frac{g\Omega}{|2\Delta|}. \tag{2.35}$$

Spontaneous decay due to off-resonant population of the excited state now occurs at an effective rate of incoherent scattering, approximately given by [42]

$$\gamma_{\text{eff}} = \left(\frac{\Omega}{2\Delta}\right)^2 \gamma. \tag{2.36}$$

As can be seen from this approximate description, the ratio of the coherent rate $\Omega_{\text{eff}}$ to the incoherent rate $\gamma_{\text{eff}}$ can be tuned by adjusting the ratio of drive strength to detuning $\Omega/\Delta$ [54].[12] Indeed, for given atomic and cavity parameters, the ratio $\Omega/\Delta$ determines how close to $P_S^{\text{bound}}$ the system operates, i.e., how close the system comes to satisfying the condition $\int_0^T |\dot{c}_g|^2 dt = 0$. This is illustrated in Fig. 2.3, using solutions of the three-level-system's Schrödinger equation (2.28). For the parameters in our experimental setup, the integral $I'_g = \int_0^\infty |\dot{c}_g|^2 dt$ is plotted for different values of $\Omega$ (and a fixed detuning $\Delta$). Also shown are calculations of $P_S^{\text{pure}} = 2\kappa \int_0^\infty |c_g|^2 dt$, normalised by the corresponding upper bound $P_S^{\text{bound,pure}}$ given by Eq. (2.31) for $m = 0$. As $\Omega$ tends to 0, $I'_g$ vanishes and $P_S^{\text{pure}}/P_S^{\text{bound,pure}}$ tends to 1. In other words, the lower the Rabi frequency (the slower we drive the Raman process) the closer to the maximum photon efficiency we can expect to get.

The plots in Fig. 2.3 show that the upper bound on the photon-collection probability is indeed approximately achievable with our drive scheme for small enough ratios of $\Omega/\Delta$. The concrete efficiency limits of our experimental apparatus will be revisited in Ch. 6. Here, the upper bounds obtained from the analytic model introduced in this chapter will be compared to experimentally measured efficiencies and to numeric simulations of the full master equation, taking into account the level scheme of the $^{40}Ca^+$ ion used in the experiments, as well as dephasing mechanisms due to imperfect frequency stability of the CMRT.

12 The failure probability due to spontaneous scattering cannot be made arbitrarily small. Its lower bound is given by $1 - P_{\text{in}}$ (see Sec. 2.2.2).

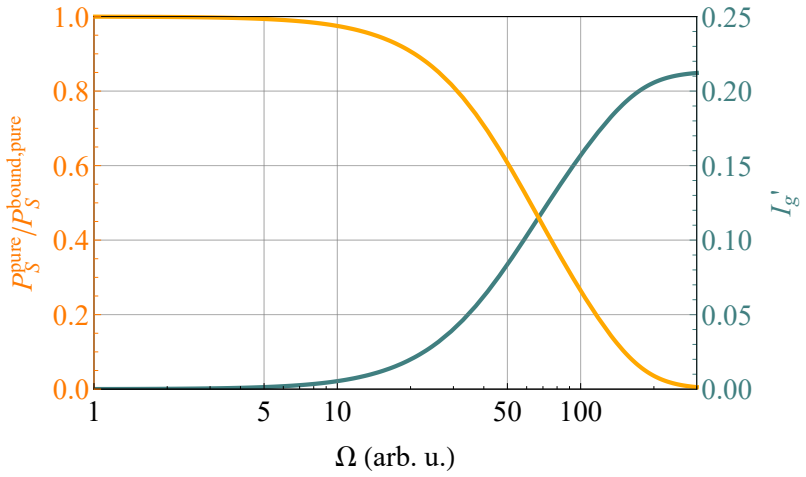


Fig. 2.3: **Approximating the upper bound on the photon-collection probability with the CMRT.** From the Schrödinger equation (2.28), the integrals $I_g' = \int_0^\infty |\dot{c}_g|^2 dt$ and $P_S^{pure} = 2\kappa \int_0^\infty |c_g|^2 dt$ are calculated for different values of $\Omega$ and the following parameters (in arbitrary units): $\Delta_C = 400$, $g = 0.88$, $\kappa = 0.07$, $\gamma = 11.5$. The Raman-resonance condition is met by setting $\Delta_C - \Delta_d = -\Delta_C/2 + \sqrt{\Omega^2 + \Delta_C^2}/2 = \delta_{AC}$, the AC Stark shift induced by the drive field on the $|u\rangle \leftrightarrow |e\rangle$ transition. The drive strength $\Omega$ is set to be constant (time independent).

Part II

# THE $^{40}Ca^{+}$ ION, EXPERIMENTAL SETUP AND METHODS

# 3

# IMPLEMENTATION OF AN ION-PHOTON INTERFACE WITH $^{40}Ca^{+}$

This chapter provides an overview of how the general model for photon generation presented in the previous chapter is implemented in our lab, thereby realising a light-matter interface for a trapped $^{40}Ca^{+}$ ion. After a short introduction to the basic principle of the experimental system, the transitions involved in our generation of single photons are identified in the level structure of $^{40}Ca^{+}$. Furthermore, our photon generation scheme (CMRT, Sec. 2.2.3), is extended to allow for the generation of ion-photon entanglement. Finally, the atomic transitions used for laser cooling, state initialisation and state readout are reviewed, as well as the use of trapped $^{40}Ca^{+}$ as a quantum bit (qubit), involving coherent manipulations on an optical quadrupole transition.

Trapped $^{40}Ca^{+}$ has been extensively employed in research projects in the field of quantum-information processing in Innsbruck (and elsewhere). In the context of cavity-QED experiments in Innsbruck, experimental demonstrations most relevant for this thesis include the generation of single photons [42, 55] as well as ion-photon entanglement [34, 36, 56] (for a nice overview of the history of cavity QED in Innsbruck, see Ch. 2 of the PhD thesis of K. Friebe [58]). The principles outlined in this chapter are for the most part based on the works listed above and provide the framework for the experimental setup and the experiments presented later in this thesis. A key difference in results achieved in this thesis, compared to those previous works, is the higher photon-collection efficiency achieved here and the theoretical understanding of the limits on that efficiency.

In Secs. 3.1, 3.2 and 3.3, text from our publication [38] has been reprinted with modifications.

## 3.1 PRINCIPLE OF THE EXPERIMENT

A single $^{40}Ca^{+}$ ion in the centre of a linear Paul trap is coupled to an optical cavity that enhances photon emission on an electronic dipole transition at 854 nm. Photons are generated via a CMRT (Sec. 2.2.3), where the external drive-laser field is detuned from a dipole transition at 393 nm, triggering the emission of an 854-nm photon into the cavity. By adding a second frequency to the drive-laser field, we can drive a bichromatic CMRT to generate entanglement between the polarisation degree of freedom of the photon and the electronic states of the ion, as will be explained in Sec. 3.3.

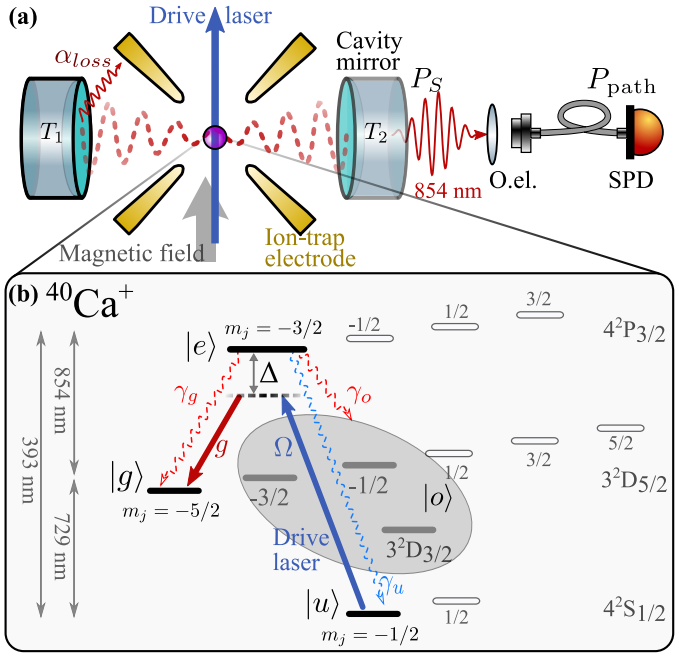


Fig. 3.1: **Implementation of the ion-photon interface with $^{40}Ca^{+}$. (a)** A $^{40}Ca^{+}$ ion in a linear Paul trap (the electrodes depicted here are for radial, in-plane, confinement) and at the focus, and a vacuum antinode, of an optical cavity. A drive-laser pulse, propagating along the quantisation axis defined by a magnetic field perpendicular to the cavity axis, causes emission of an 854-nm photon into a vacuum mode of the cavity. Mirror transmission coefficients are denoted $T_1$ and $T_2$, $\alpha_{loss}$ is the cavity round-trip loss, $P_S$ is the probability for obtaining a photon in the cavity output mode, $P_{path}$ is the probability that a photon in the cavity output mode reaches the fibre-coupled single-photon detector (SPD) via some optical elements (O.el.) and is detected. **(b)** Atomic level scheme showing the CMRT for photon generation. The cavity (red solid arrow) and drive laser (blue solid arrow) have a common detuning of $\Delta/2\pi = -403(5)$ MHz from the excited state. The vacuum Rabi frequency of the ion-cavity coupling is $g$, the Rabi frequency of the drive laser is $\Omega$. Ground states other than $|g\rangle$ and $|u\rangle$ to which the excited state $|e\rangle$ can decay are grouped in state $|o\rangle$ (contained within grey oval). The spontaneous decay rates are $(\gamma_g, \gamma_u, \gamma_o)/2\pi = (0.45, 10.74, 0.30)$ MHz, with $\gamma_g + \gamma_u + \gamma_o = \gamma = 2\pi \times 11.49(3)$ MHz. This figure has been modified from Fig. 2 of Ref. [38].

The generated photon preferentially leaks out of the cavity mirror with transmission $T_2$ into the cavity output mode. See Fig. 3.1a for a schematic of the experiment. The total probability $P_{tot}$ for detecting a photon is estimated from many repeated attempts to generate and detect a photon. This total probability is given by $P_{tot} = P_S P_{path}$, where the photon collection probability $P_S$ is the probability for obtaining a photon in the cavity output mode and the path efficiency $P_{path}$ is the probability that a photon in the cavity output mode reaches the detector and is detected. From an independent calibration of $P_{path}$, the probability $P_S$ can be determined and compared to the upper bound

given by Eq. (2.31). The components of the setup shown in Fig. 3.1a will be described in detail in Ch. 4.

## 3.2 TRANSITIONS FOR PHOTON GENERATION

The Λ-scheme $|u\rangle \leftrightarrow |e\rangle \leftrightarrow |g\rangle$ in Fig. 2.2 is realised in $^{40}Ca^{+}$ within the fine-structure (angular-momentum state) manifolds $4^2S_{1/2} \leftrightarrow 4^2P_{3/2} \leftrightarrow 3^2D_{5/2}$. Here, the notation $^{2s+1}L_J$ is used, with spin s, orbital angular momentum L and total angular-momentum quantum-number J. The $S_{1/2}$ manifold is the lowest-lying of $^{40}Ca^{+}$ that is not fully occupied and is infinitely long lived. The $D_{5/2}$ manifold is a metastable state with a lifetime of 1.17 s [59], which can be considered infinite on the timescales relevant to the experiments of this work. The excited-state manifold $P_{3/2}$ has a lifetime of $\tau = 6.924(19)$ ns [60] and corresponding rate of spontaneous emission $1/(2\tau) = \gamma = 2\pi \times 11.49(3)$ MHz.

An externally applied magnetic field lifts the degeneracy of these manifolds such that individual Zeeman sublevels $m_j$ can be addressed in a frequency-selective manner. In the context of this thesis, the magnetic field has a strength of 4.23 G (see Sec. 4.3), resulting in a Zeeman splitting of the $D_{5/2}$ manifold of $\delta_Z/2\pi = 7.1$ MHz. The CMRT couples the initial state $|u, 0\rangle = |4^2S_{1/2}, m_j = -1/2\rangle\,|0\rangle$, where the second ket describes the cavity photon number, to the metastable final state $|g, 1\rangle = |4^2D_{5/2}, m_j = -5/2\rangle\,|1\rangle$ via the intermediate excited state $|e, 0\rangle = |4^2P_{3/2}, m_j = -3/2\rangle\,|0\rangle$. The three atomic states are shown as thick black lines in the atomic level scheme of Fig. 3.1b. The reasons for choosing these states for photon generation in the level structure of $^{40}Ca^{+}$ are outlined in Ref. [61].

The excited state $|e\rangle$ can decay to states other than $|g\rangle$ and $|u\rangle$, namely the Zeeman sublevels $|m_j = -3/2\rangle$ and $|m_j = -1/2\rangle$ of the $D_{5/2}$ manifold as well as the $3^2D_{3/2}$ manifold. For the purpose of future calculations, these other states can be grouped in a fourth artificial state $|o\rangle$ (grey oval in Fig. 3.1b). With the branching ratios r and Clebsch-Gordan coefficients $\mathcal{G}$ displayed in Fig. 3.2, the atomic decay rates are calculated as

$$\begin{aligned}
\gamma_g &= \gamma \times r_{D_{5/2}} \times (\mathcal{G}_{-\frac{5}{2}})^2, \\
\gamma_u &= \gamma \times r_{S_{1/2}}, \\
\gamma_o &= \gamma \times r_{D_{5/2}} \left[(\mathcal{G}_{-\frac{3}{2}})^2 + (\mathcal{G}_{-\frac{1}{2}})^2\right] + \gamma \times r_{D_{3/2}},
\end{aligned}$$

yielding $(\gamma_g, \gamma_u, \gamma_o)/2\pi = (0.45, 10.74, 0.30)$ MHz. The Clebsch-Gordan coefficients $\mathcal{G}_m$ describe the transition amplitudes between the states $|e\rangle = |P_{3/2}, m_j = -3/2\rangle \rightarrow |D_{5/2}, m\rangle$, with final Zeeman sub-level $|m\rangle$, and are given by $\mathcal{G}_m = (\sqrt{10/15}, -\sqrt{4/15}, \sqrt{1/15})$, with $m = (-5/2, -3/2, -1/2)$ (see Fig. 3.2b), respectively.

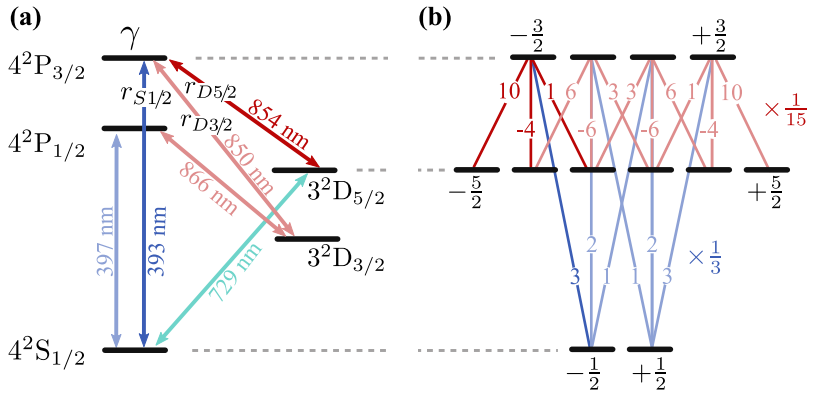


Fig. 3.2: **$^{40}Ca^{+}$ level scheme** with transition wavelengths, branching ratios and transition amplitudes relevant for this thesis. **(a)** Total decay of $P_{3/2}$ [60]: $\gamma/2\pi = 11.49(3)$ MHz. Branching ratios [62]: $r_{D1/2} = 0.9347(3)$, $r_{D3/2} = 0.00661(4)$, $r_{D5/2} = 0.0587(2)$. **(b)** Zeeman sublevels and corresponding Clebsch-Gordan coefficients $\mathcal{G}$ of the states $|4^2S_{1/2}\rangle$, $|4^2P_{3/2}\rangle$ and $|3^2D_{5/2}\rangle$. The Clebsch-Gordan coefficient of a particular transition is obtained by multiplying the modulus of the respective number with the factor on the right, taking the square root and applying the sign indicated with the number. This figure was inspired by Fig. 1 from Ref. [63].

A circularly polarised drive laser, propagating along the magnetic field axis, addresses the $|u\rangle \leftrightarrow |e\rangle$ dipole transition at 393 nm with a detuning $\Delta/2\pi = -403(5)$ MHz and a Rabi frequency $\Omega$ set by (our choice of) the drive-laser intensity. The cavity is detuned by the same amount from the 854-nm $|g\rangle \leftrightarrow |e\rangle$ dipole transition. In terms of the decay rates introduced above, the ion-cavity coupling strength of Eq. (2.12) can be written on the $D_{5/2} \leftrightarrow P_{3/2}$ transition as

$$g = \sqrt{\frac{c\gamma r_{D5/2}}{2l\widetilde{A}_{\text{eff}}}}\mathcal{G}_m\zeta = g_0\mathcal{G}_m\zeta. \tag{3.1}$$

As a reminder, $\zeta$ [see Eq. (2.11)] accounts for the projection of th cavity polarisation onto the atomic dipole moment. For all the experiments in this thesis, the magnetic field axis is aligned perpendicular to the cavity axis and parallel to the propagation direction of the drive field. The atomic quantisation axis is chosen to be parallel to the magnetic field axis, and photon polarisation along this axis is denoted horizontal (H). The polarisation of a photon generated in the cavity on the $|g\rangle \leftrightarrow |e\rangle$ transition is vertical (V), as determined by the projection of the $|g\rangle \leftrightarrow |e\rangle$ dipole moment onto the plane perpendicular to the cavity axis. This projection leads to $\zeta = \sqrt{0.5}$ in Eq. (3.1), such that $g = g_0\sqrt{5/15}$.

## 3.3 BICHROMATIC RAMAN TRANSITION FOR ION-PHOTON ENTANGLEMENT

Entanglement between ion and photon is generated via a bichromatic CMRT that was developed and first demonstrated in Refs. [34, 36]. Here, a second, co-propagating, drive-laser field is added, detuned from the frequency of the original drive-laser field by the Zeeman splitting $\delta_Z$ between $|g_1\rangle = |g\rangle = |D_{5/2}, m_j = -5/2\rangle$ and neighbouring state $|g_2\rangle = |D_{5/2}, m_j = -3/2\rangle$. Consequently, a second Raman process is simultaneously driven. In free space, this second Raman transition generates a $\pi$-polarised photon which is projected to horizontal (H) polarisation within the cavity. Here, the resulting polarisation projection is $\zeta = 1$. See Fig. 6.4a in Ch. 6 for a simplistic graphical representation of the bichromatic CMRT in $^{40}Ca^{+}$.

Following Eq. (2.35), the effective coherent coupling strength of each Raman process with final state $|g_i\rangle$ ($i \in \{1, 2\}$) is given by

$$\Omega_i^{\text{eff}} \approx \frac{\Omega_i g_i}{|2\Delta_i|}, \tag{3.2}$$

with $\Omega_i$ the Rabi frequency of each drive component, $\Delta_i$ the corresponding detuning from the excited state $|e\rangle$ and $g_i$ the ion-cavity coupling strength on the transition $|e\rangle \leftrightarrow |g_i\rangle$. We assume that the Raman resonance condition is fulfilled for each drive field. The two Raman transitions were chosen to yield both high and similar coupling strengths [61]: with a polarisation projection $\zeta = 1$ and Clebsch-Gordan coefficient $\mathcal{G}_{-3/2} = \sqrt{4/15}$, the ion-cavity coupling strength on the $|e\rangle \leftrightarrow |g_2\rangle$ transition, $g_2 = g_0\sqrt{4/15}$, is similar compared to the $|e\rangle \leftrightarrow |g_1\rangle$ transition, for which $g_1 = g_0\sqrt{5/15}$. For further details on the choice of the two transitions for the generation of ion-photon entanglement, see Ref. [61].

In the case where the two Raman processes occur with equal probability, the initial state $|u\rangle|0\rangle$ is ideally transferred to the final, maximally entangled state of ion and cavity photon

$$|\Psi(\theta)\rangle = \frac{1}{\sqrt{2}}\left(|g_1\rangle|V\rangle + e^{i\theta}|g_2\rangle|H\rangle\right), \tag{3.3}$$

where the phase $\theta$ is set by the relative phase of the two laser fields and can be tuned [34]. A qubit encoded in the photon's polarisation is therefore entangled with a qubit encoded in the ion's electronic states $|g_1\rangle$ and $|g_2\rangle$. As shown in Ref. [34], by setting the frequency difference between the bichromatic components to the Zeeman splitting $\delta_Z$ of the $D_{5/2}$ manifold, the phase of the atomic state after photon detection, and therefore the experimental reconstruction of the entangled state $|\Psi(\theta)\rangle$, is independent of the photon detection time.

It should be noted that frequency-degenerate polarisation eigenmodes of the cavity are assumed in the model presented above, i.e.,

a non-birefringent cavity. Sec. 4.1.1 contains a brief discussion of the complications that cavity birefringence introduces in the generation of the ion-photon entangled state of Eq. (3.3), as well as a description of our methods for avoiding and characterising birefringence in our system.

## 3.4 TRAPPED $^{40}Ca^{+}$ AS A QUANTUM BIT

The ion-photon interface implemented in this thesis requires a high degree of control over both the external and internal degrees of freedom of the $^{40}Ca^{+}$ ion. This section gives a brief overview of how cooling of the ion, as well as state initialisation, state detection and coherent manipulation of the ion qubit are implemented within the level structure of $^{40}Ca^{+}$. More detailed information on the transitions of $^{40}Ca^{+}$ as well as treatments of laser cooling, state initialisation and state readout are readily available in the literature (e.g., Refs. [64, 65]) and other theses published in the field (e.g., Ch. 3 of Ref. [66]).

### 3.4.1 *Cooling, state preparation and state detection*

The electric dipole transitions $S_{1/2} \leftrightarrow P_{1/2}$ and $P_{1/2} \leftrightarrow D_{3/2}$, displayed in Fig. 3.2a, are used for both Doppler cooling the ion and readout of the ion-qubit state. The $P_{1/2}$ state has a decay rate $\gamma_{P_{1/2}}/2\pi = 11.2$ MHz and preferentially decays back to the $S_{1/2}$ manifold, while decay to the (metastable) $D_{3/2}$ manifold only happens with a branching fraction of 0.064 [67]. The transition $S_{1/2} \leftrightarrow P_{1/2}$ is driven using a laser at 397 nm (Sec. 4.4.1), while a repumping laser at 866 nm (Sec. 4.4.1) drives any population in the $D_{3/2}$ state back to the excited $P_{1/2}$ state.

Photons at 397 nm, scattered from the ion during interaction with those lasers, provide the momentum transfer for Doppler cooling [68]. The laser parameters (powers and detunings) for Doppler cooling (and state detection, see below) are set up according to the procedure described in numerous theses in the field, e.g., Ref. [69] (Sec. 4.2). After Doppler cooling in our system, mean phonon numbers of 11(2) and 8(2) are found in the axial and radial modes with mode frequencies[1] of $2\pi \times 0.9$ MHz and $2\pi \times 2.4$ MHz, respectively.

Cooling the ion via Doppler cooling localises the ion to within a fraction of a half-wavelength of the cavity's optical standing wave, as discussed in Ref. [36] (Sec. 6.1). Following Ref. [36], we estimate the ion's spatial extent along the cavity axis after Doppler cooling in our setup to be around 20 nm, using the above values for the mean phonon number and the trap frequency in the radial direction.[2] For

1 The motional modes of the ion in our trap are introduced in Sec. 4.2.

2 By comparison, the intra-cavity field, and thereby the ion-cavity coupling strength, is reduced by merely 1% at a distance of 20 nm from an anti-node.

the maximum photon-generation efficiency, the ion even needs to be cooled close to its ground state of motion, in order to maximise the coupling strength of the CMRT, as discussed in Sec. 3.4.2.

When detected with a photomultiplier tube (PMT) or electron multiplying charge-coupled device (EM CCD) camera (Sec. 4.6), photons scattered on the $S_{1/2} \leftrightarrow P_{1/2}$ transition shed light on the atomic state[3]: if the ion is in the $D_{5/2}$ manifold, which remains uncoupled from interaction with the lasers at 397 nm and 866 nm, no photons are scattered, and the ion is said to be *"dark"*. Otherwise, if the ion is in the $S_{1/2}$ state, it is *"bright"*, and fluorescence is detected at 397 nm. This technique is known as *electron shelving* [64] and is used to analyse the ion-qubit state for the ion-photon entanglement protocol. See Ref. [69] (Sec. 4.2) for a description of the procedure we follow in order to set up state detection. For details on the experimental parameters (detection time, scattering rate, signal-to-noise ratio), see Sec. 5.3.

Initialising the ion in state $|u\rangle$ is accomplished via optical pumping. Here, the $S_{1/2} \leftrightarrow P_{1/2}$ transition is driven with a 397-nm $\sigma^{-}$-polarised laser field (Sec. 4.4.1), propagating along the magnetic field axis, in combination with repumping at 866 nm. Additional repumping at the 854-nm wavelength is performed in case there is a possibility for the ion to be in the $D_{5/2}$ manifold, i.e., after interaction with the photon-generation drive laser at 393 nm or the laser at 729 nm.

### 3.4.2 *Operations on the optical quadrupole transition*

The transition $S_{1/2} \leftrightarrow D_{5/2}$ is an optical quadrupole transition, such that the $D_{5/2}$ manifold is metastable with a lifetime of 1.17 s [59]. The transition is driven with a laser at 729 nm (Sec. 4.4.4) for coherent manipulation of the ion qubit and for resolved sideband cooling.

Two Zeeman states, one in each of the $S_{1/2}$ and $D_{5/2}$ manifolds, can be used to encode a qubit over which full quantum control is well established [24, 70]. Qubit operations, in this thesis, are limited to resonant laser pulses for analysing the ion-photon entangled state. For this purpose, the D-manifold qubit of the ion-photon entanglement protocol (encoded in the states $|g_1\rangle$ and $|g_2\rangle$) is converted to the (optical) S-D qubit with logical states $|u\rangle$ and $|g_2\rangle$, as in Ref. [34]. This is done by mapping the $|g_1\rangle$ population to the $|u\rangle$ state, corresponding to a $\pi$-pulse on the $|g_1\rangle \leftrightarrow |u\rangle$ transition. The complete pulse sequence for the ion-qubit measurement is outlined in Sec. 5.3.

A second use of the 729-nm transition in this thesis is for resolved sideband cooling of the ion [71, 72]. The technique is implemented according to the procedure outlined in Ref. [69] (Sec. 4.6). Using a 729-nm laser beam that has an overlap with all three motional modes of the ion ("729-ax", see Sec. 4.4), mean phonon numbers of

3 In the context of this thesis, only the PMT signal is used for detecting the state of the ion.

$\bar{n} < 0.5(2)$ are achieved in each motional mode. The mean phonon number $\bar{n}$ is determined by measuring Rabi oscillations on the 729-nm qubit transition and fitting the observed dependence of the excitation probability on the 729-nm pulse length with a model that takes into account the ion temperature (see Ref. [66] Sec. A1). Rabi oscillations are performed with two different 729-nm laser-beam directions ("729-ax" and "729-rad", see Sec. 4.4), allowing the temperature in different motional modes to be distinguished.

In the context of cavity-photon generation, the dominant effect of being outside the motional ground state in our system is due to changes in the coupling of the drive laser to the ion. Specifically, for a motional mode with phonon number $n$, the drive-laser Rabi frequency in the CMRT can be approximated by $\Omega_n \approx \Omega(1-\eta^2 n)$ [64]. Here, $\eta = \vec{k}\vec{e}_z\sqrt{\hbar/(2m\omega_z)}$ is the Lamb-Dicke parameter, quantifying the coupling strength between internal states of an ion of mass $m$ and its (harmonic) motional mode along $\vec{e}_z$ with frequency $\omega_z$. The approximation holds for $\eta^2(2n+1) \ll 1$, the Lamb-Dicke regime [64]. For the full expression without approximation, see, e.g., Ref. [73] or Eq. (3.11) of Ref. [66]. Outside of the ground state, the coupling of the drive-laser to the motional modes of the ion causes a reduction of the Rabi frequency $\Omega_n$ and therefore a reduction in the rate of the CMRT [Eq. (2.35)] used to generate cavity photons. At the same time, the effective spontaneous decay rate [Eq. (2.36)] remains constant at Doppler-cooled temperatures and below, leading to a reduced maximum efficiency for cavity photon production. Experimental data highlighting this effect is shown in Sec. 7.5.

# 4

# EXPERIMENTAL SETUP

The experiments presented in this thesis were carried out on a newly built setup located in Lab 1 at the Institute of Quantum Optics and Quantum Information (IQOQI) in Innsbruck. The design of the ion-cavity system is based on the setup built during the PhD of Carlos Russo [42] at the University of Innsbruck (UIBK), in the following simply called UIBK setup. While important parameters of the two setups are the same, in particular the cavity and trap geometries and relative orientation, the setup described in this thesis was designed from scratch and incorporates many changes. A key improvement in the new setup are the cavity parameters: the lower value for the unwanted cavity loss $\alpha_{loss}$ and a tailored value of the output mirror transmission $T_2$ in our setup allowed for an increase in the photon-collection probability $P_S$ from 0.19(3) in [34] to 0.72(3) in this work. Other notable differences will be pointed out in the corresponding sections of this chapter.

Throughout this chapter, the experimental layout will be described with respect to the cardinal directions indicated in Fig. 4.1 (we follow here the convention also described in [58]): when looking at the chamber through the single largest CF100 viewport, the left side is referred to as "west" (W), the right side as "east" (E), while the upper side of the setup is "top" or "north" (N) and the lower side of the setup is "bottom" or "south" (S). The side facing the spectator is denominated "front" (F), the far side, which is closest to the quantum simulation "Qusim" experiment, is called "back" (B).

The components shown in Fig. 4.1 are integrated with the vacuum chamber in the following way. The optical cavity is attached to the bottom flange of the chamber via a system of translation stages used for 3D positioning of the cavity with respect to the trap. The ion trap is rigidly attached to the top flange, with the trap axis vertical and perpendicular to the cavity axis. Atomic fluorescence for detecting the internal state of the ion is collected with an objective that is mounted 6 cm from the trap centre in an inverted viewport coming in from the back side.

The whole setup takes up two optical tables (and overhead racks): the vacuum chamber containing ion trap and cavity is located at the *"experiment table"*[1], most of the lasers are installed on the *"laser table"*[2]. Note that a third table, the *"conversion table"*[3], accommodates the setup for the frequency conversion to telecom wavelength which is part

1 Newport M-ST-UT2-58-12
2 Melles Griot
3 Melles Griot

of the experiment presented in Ch. 7. An overview of the setup for frequency conversion will be given in Ch. 7, a detailed description can be found in Refs. [39, 40] and the upcoming thesis of M. Meraner [41].

In the following sections, the components of the setup (excluding the conversion setup) and their function in the experiment are presented in detail, with a focus on the cavity, its construction and characterisation (Sec. 4.1). After that, the ion trap is described (Sec. 4.2), followed by an overview of the vacuum chamber (Sec. 4.3) and the various laser systems (Sec. 4.4). The detection path for cavity photons is characterised (Sec. 4.5), followed by a description of the detection setup for ion fluorescence (Sec. 4.6). The chapter concludes with an overview of the experimental control system (Sec. 4.7).

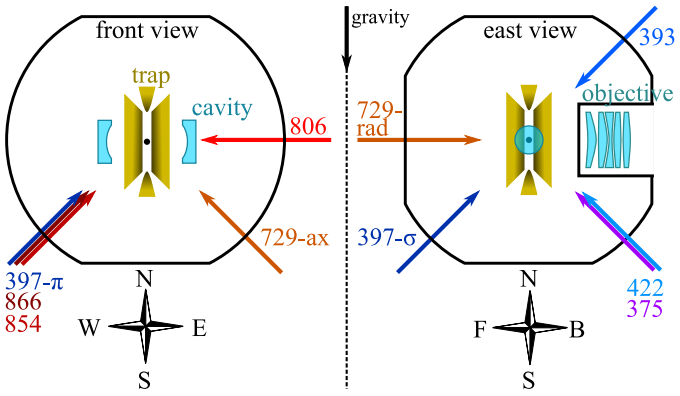


Fig. 4.1: **Schematic showing the relative geometry of the ion-cavity system.** Left: view through the single large (CF100) viewport of the vacuum chamber hosting the cavity and trap, with an ion at the centre. The principle axis of the linear ion trap is vertical, defined by the location of the endcap electrodes (gold tips). Right: view from the east of the vacuum chamber, where the objective for collecting the ion fluorescence can be seen in an inverted viewport coming in from the back side. The various laser beams for illuminating the ion or stabilising the cavity length enter the chamber at normal angles through viewports.

## 4.1 OPTICAL CAVITY

As we have seen in Ch. 2, a small cavity waist and low internal cavity loss are essential for the realisation of a deterministic light-matter quantum interface. For single neutral atoms, the conditions for the deterministic interaction between matter and single photons are usually achieved via high-finesse optical resonators of microscopic lengths [49, 74, 75]. Owing to their long-range Coulomb interaction, trapped ions are one of the leading platforms in the field of quantum information processing (QIP) and make for promising candidates as nodes in a quantum network. Their long-range interaction, however, makes trapped ions particularly difficult to efficiently interface with photons: anything without precisely controllable charge, like, e.g., the

dielectric surface of a cavity mirror, will disturb the trapping field if brought too close [76, 77]. Despite this challenge, there has been recent progress on interfacing trapped ions with microscopic cavities [35, 78].

In this work, instead of taking the approach of a microscopic-length cavity, a near-concentric cavity was constructed, following the successful implementation during the PhD work of Carlos Russo [42]. A near concentric cavity is characterised by its length being close to twice the mirror ROC. With this, a microscopic waist [see Eq. (2.5)] at a macroscopic ion-mirror separation (10 mm) is achieved, rendering the effect of mirror surface charges on the trapping potential negligible.[4] This approach comes at the cost of having to build a cavity close to the edge of the stability region, where the slightest misalignment introduces significant additional optical loss. Moreover, with a large surface area being sampled by the cavity mode [Eq. (2.6)], the near-concentric configuration is highly susceptible to loss caused by defects on the mirrors' surfaces. In the following, an overview is first given of the cavity characterisation methods and the results for the final, in-vacuum cavity. After that, the main aspects of the cavity design will be described as well as key points in the construction process. Finally, the scheme and performance of the cavity length control and stabilisation are presented.

### 4.1.1 *Cavity characterisation*

A precise knowledge of the cavity parameters is essential for a meaningful comparison between data and theory: both when modelling the system with numerical simulations and when comparing measured efficiencies with the upper bound given by Eq. (2.31). Important parameters of the final in-vacuum and ion-trap-integrated cavity are summarised in Table 4.1. In the following, the employed methods for obtaining these values are explained.

| $w_0$ (μm) | $g_0/2\pi$ (MHz) | $\kappa/2\pi$ (kHz) | $\mathcal{F}/10^3$ | $\alpha_{\text{loss}}$ (ppm) | $T_2$ (ppm) |
|---|---|---|---|---|---|
| 12.31(8) | 1.53(1) | 70(2) | 54(1) | 26(4) | 90(4) |

Table 4.1: **Key cavity parameters at 854 nm.** $w_0$: waist. $g_0$: ion-cavity coupling strength on the $D_{5/2} \leftrightarrow P_{3/2}$ transition. $\kappa$: decay rate. $\mathcal{F}$: Finesse. $\alpha_{\text{loss}}$: unwanted round-trip loss (all cavity loss except $T_2$). $T_2$: output-mirror transmission.

MEASUREMENT OF THE FREQUENCY SPACINGS OF THE CAVITY MODES: From a measurement of the cavity's FSR $\Delta\nu_{\text{FSR}}$ [Eq. (2.1)]

4 That is, we do not see the effects of charges on the mirror surfaces affecting the experiments presented in this thesis.

and higher-order mode spacing $\Delta\nu_{mn}$ [Eq. (2.4)], the cavity length and mirror ROC $R_C$ can be determined. Important parameters can therefore be derived, such as the cavity waist $w_0$ [Eq. (2.5)] and ion-cavity coupling strength $g_0$ [Eq. (2.12)].

Two methods to determine the frequency spacings $\Delta\nu_{FSR}$ and $\Delta\nu_{mn}$ were used at different stages. For both methods, laser light at 854 nm is coupled to the cavity and the cavity length is scanned across one FSR via a piezo under one of the mirrors. Like this, the cavity transmission signal, measured by a photodiode and displayed on an oscilloscope, contains the transmission peaks of two axial modes ($TEM_{q00}$ and $TEM_{q+1,00}$) with frequencies $\nu_{q00}$ and $\nu_{q+1,00}$ [Eq. (2.4)] spaced by $\Delta\nu_{FSR}$. The laser is aligned to the cavity in such a way that the peaks of higher-order $TEM_{mn}$ modes, spaced by $\Delta\nu_{nm}$, are also clearly visible. In addition to this main laser, an auxiliary light field is simultaneously coupled to the cavity. The auxiliary field has a precisely tunable and known frequency difference $\Delta\nu$ with respect to the first laser. The mode spacings $\Delta\nu_{FSR}$ ($\Delta\nu_{mn}$) can then be directly measured by tuning $\Delta\nu$ until the $TEM_{q00}$ transmission peak of the auxiliary field overlaps with the $TEM_{q+1,00}$ ($TEM_{qmn}$; $m, n \neq 0$) transmission peak of the main laser on the oscilloscope.

Throughout the construction phase of the cavity, when determining how close to the concentric limit the cavity was aligned (Sec. 4.1.2), the auxiliary laser field was given by a second, independent laser. Here, the frequencies of both lasers were measured with a wavelength meter (WLM)[5] and the frequency spacings could be determined with a precision of 1 MHz, limited by the 1-MHz resolution of the WLM.

*Measured mode spacings, cavity length and mirror ROC*

For the final characterisation of the in-vacuum cavity (determining the values for $w_0$ and $g_0$ in Table 4.1), the auxiliary light field was given by a first-order sideband modulated onto the laser via a signal generator and fibre electro-optic modulator (EOM)[6]. With this method, $\Delta\nu_{FSR} = 7.5303(2)$ GHz could be determined, corresponding to a cavity length of $l = 19.9057(5)$ mm. The distances of the $TEM_{01}$ and $TEM_{10}$ modes from the nearest $TEM_{00}$ mode were measured to be $\Delta\nu_{01} = 270.9(1)$ MHz and $\Delta\nu_{10} = 265.3(1)$ MHz, respectively. The error here is limited by the resolution of the transmission signal, i.e., by how accurately the transmission peaks of both fields could be overlapped by eye on the oscilloscope displaying the transmission signals. The non-degeneracy of the $TEM_{01/10}$ modes (present in all transverse modes) is potentially caused by an astigmatism of the cavity, i.e., at least one of the cavity mirrors has two different radii of curvature. This non-degeneracy is not accounted for by Eq. (2.4), for which cylindrical symmetry is assumed.

Fig. 4.2 shows a graphical representation of the modes and their relative frequencies in the transmission spectrum. The indicated transverse

5 High-Finesse WSU-10
6 Photline NIR-MPX800-LN-10, 10 GHz bandwidth

mode spacing corresponds to the average $\overline{\Delta\nu}_{mn} = (\Delta\nu_{01} + \Delta\nu_{10})/2 = 268.1$ MHz and the uncertainty was chosen to be half the frequency splitting $\pm(270.9 - 265.3)/2$ MHz $= \pm 2.8$ MHz. Assuming the same ROC for both mirrors, a value of $R_C = 9.9841(7)$ mm is obtained from Eq. (2.4). Via Eq. (2.5), a cavity waist $w_0 = 12.31(8)$ µm can be inferred from the measured values of $l$ and $R_C$, corresponding to an ion-cavity coupling strength $g_0/2\pi = 1.53(1)$ MHz on the $D_{5/2} \leftrightarrow P_{3/2}$ transition at 854 nm [Eq. (3.1)].

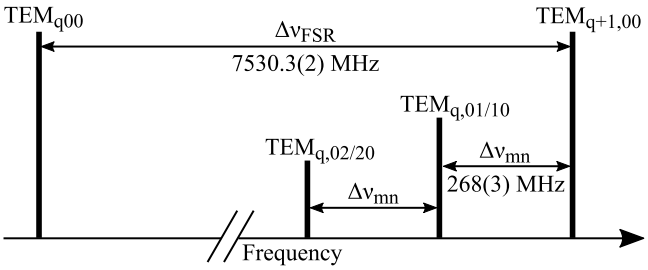


Fig. 4.2: **Simplified representation of the cavity transmission spectrum.** Vertical lines indicate the peaks of $TEM_{qmn}$ modes in the cavity transmission spectrum of a laser coupled to the cavity, when scanning the cavity length over one FSR. Heights are arbitrary and not to scale. Further peaks of higher-order transverse modes, as well as the non-degeneracy of the transverse modes, visible in a real spectrum, are not drawn. Note how the transverse modes are grouped to the lower-frequency side of the next axial mode, which is a property of the near-concentric configuration.

MEASUREMENT OF THE CAVITY DECAY RATE AND FINESSE: The cavity decay rate $\kappa$ and finesse $\mathcal{F}$ were obtained from a measurement of the cavity decay time $\tau$, via a so-called ringdown measurement. Here, the frequency of an incident laser is scanned until it becomes resonant with a $TEM_{00}$ axial mode of the cavity. Triggered upon a preset threshold $I_0$ of the transmitted light intensity, the incident laser is switched off[7] on a time scale of a few nanoseconds, in order to allow for the measurement of the exponentially decaying light-intensity leaking from the cavity. The decay time constant $\tau = 1/(2\kappa) = (\mathcal{F}/\pi)(l/c)$, with $c$ the speed of light, can then be retrieved from an exponential fit to the data of the form $I(t) = I_0 e^{t/\tau}$. With knowledge of the cavity length $l$, the Finesse can be determined and from it the total losses $\mathcal{L} = T_2 + \alpha_{loss}$ of the resonator [Eq. (2.2)].

Using this method, the final batch of mirrors received from the coating company was characterised during the early stages of the experiment (Appendix A.2). Furthermore, the suitability of individual mirror pairs for building near-concentric resonators was tested by measuring the finesse for different cavity lengths. The closer to the concentric limit the cavity is, the larger the cavity mode cross-section on the mirrors, rendering the near-concentric configuration highly

7 using a Schmitt trigger and acousto-optic modulator (AOM)

susceptible to loss caused by potential defects on the mirrors' surfaces. A mirror pair was selected with one of the highest finesse values of the batch (Appendix A.2) and where the finesse did not decrease significantly when aligning the mirrors in the near-concentric regime.

The finesse of a cavity formed by the aforementioned mirror pair was measured at various points during the construction phase; a timeline is displayed in Fig. 4.3. At a wavelength of 854 nm, a finesse of $\mathcal{F} = 62(3) \times 10^3$ was measured out of vacuum in a test setup, with each mirror mounted on a multi-axes alignment stage. This finesse was obtained for a cavity length $l = 18.5(5)$ mm, measured with a caliper for the sake of a quicker measurement. In a near-concentric configuration, a finesse of $60(1)\times10^3$ was measured in the test setup (for the same length as the the in-vacuum cavity discussed above). In this case and in the following, the uncertainty corresponds to $\pm1\sigma$ standard deviation, dominated by shot-to-shot fluctuations in a succession of up to ten closely-spaced measurements (taken with a repetition rate on the order of 1 Hz). After fully assembling the cavity out of vacuum (gluing the mirrors in place on the piezos, as described later), a finesse of $59(1)\times10^3$ was measured (for the in-vacuum cavity length), which corresponds to an increase in $\mathcal{L}$ of 4(2) ppm. Integrating the cavity with the ion trap into the vacuum chamber (involving a two-week vacuum bake at 80 °C, see Sec. 4.1.2) was achieved without any discernable drop in finesse. After the cavity had been in vacuum for a few weeks, the finesse dropped to $54(1)\times10^3$, corresponding to a further increase in $\mathcal{L}$ of 9(2) ppm to a final value of $\mathcal{L} = 116(2)$ ppm. The reason for this additional loss is likely some misalignment of the cavity, the cause of which is unclear. After that, no further change of the finesse was registered.

*Measured cavity finesse*

MEASUREMENT OF THE MIRROR LOSSES AND TRANSMISSION: The individual mirror transmission values $T_{1,2}$ and the cavity internal loss $L = L_1 + L_2$, comprising the individual mirror losses $L_{1,2}$ due to scattering and absorption, were quantified via two different methods. The first method, employed during the cavity construction phase, consisted in measuring $T_1$ and $T_2$ directly by detecting the fraction of laser light transmitted through the bare mirrors. Using a diode laser[8] and calibrated power meters[9] the values obtained at 854 nm via this first method are $T_1 = 2.0(1)$ ppm, $T_2 = 92(4)$ ppm. The value for L is then calculated to be $L = L_1 + L_2 = \mathcal{L} - T_1 - T_2 = 22(4)$ ppm, using the final value for $\mathcal{L}$ of 116(2) ppm (see above). The standard deviations of the results were obtained from repeated measurements. Care was taken to rule out systematic error sources like scattered or stray light, nonlinearities in the power meters and an off-centred or tilted mirror surface with respect to the impinging beam. Nonetheless, due to the

8 Toptica DL Pro

9 Thorlabs S130C for low transmission (~ 2 ppm) measurements, Thorlabs S132C for the high transmission (~ 100 ppm) measurements

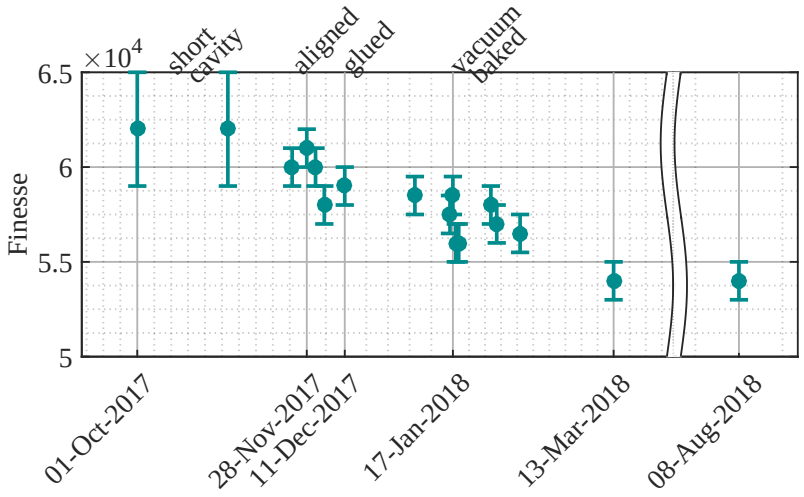


Fig. 4.3: **Cavity finesse timeline.** The cavity finesse was measured via cavity ringdown. For the earliest two data points, the error bars are due to an uncertainty in the cavity length (measured with a caliper), for all the other data points the cavity length was determined more accurately via the method of measuring mode frequency spacings described earlier in this section and the uncertainty corresponds to $\pm 1\sigma$ standard deviation of repeated measurements.

sensitivity of the technique to these systematic error sources, it is difficult to assess the uncertainties and reliability of the measurement.

Once the cavity was fully assembled and in vacuum, a second method was used, following the protocol described in Ref. [79]. Here, a laser coupled to a specific mode of the cavity is considered. The reflected power $P_r$ and transmitted power $P_t$ are compared to the input power $P_{in}$, in the realistic situation where only the fraction $\epsilon P_{in}$ of the incoming light matches the cavity mode. The following equation is derived

$$\frac{P_t}{P_r - P_{in}} = \frac{4T_1T_2(\frac{\mathcal{F}}{2\pi})^2}{(L + T_1 - T_2)^2(\frac{\mathcal{F}}{2\pi})^2 - 1}, \tag{4.1}$$

which is independent of the mode-matching factor $\epsilon$. By using each side of the cavity alternatively as input port, as reported also in Ref. [42], a system of equations is obtained from which, after simple algebraic manipulation, $T_1$, $T_2$ and $L$ can be extracted.

For the characterisation of our cavity, a laser was scanned across the resonance of a $TEM_{00}$ mode, recording the transmission and reflection curves as well as the input light levels with photodiodes. A series of ten closely spaced measurements to either side of the cavity, together with a measurement of the cavity finesse, yielded the following results at 854 nm: $T_1 = 2.9(4)$ ppm, $T_2 = 90(4)$ ppm and $L = 23(4)$. With this, a value of $\alpha_{loss} = T_1 + L = 26(4)$ ppm is given as the final value for the unwanted loss of our system, as presented in Table 4.1. Uncertainties represent one standard deviation. Within error bars, these outcomes

*Measured transmission and loss coefficients of the cavity*

match the ones of the first method. The results of both methods, as well as values obtained at 806 nm (the wavelength of the laser to which the cavity length is stabilized) via the second method, are summarised in Table 4.2. The second method can be considered a more systematic approach than the first method, depending less on the skill of the experimentalist and being less prone to systematic errors. Therefore, the values obtained via the second method are used for the calculation of probabilities in Ch. 6.

| IN PPM: | $T_1$ | $T_2$ | L |
|---|---|---|---|
| METHOD 1 | 2.0(1) | 92(4) | 22(4) |
| METHOD 2 (854 NM) | 2.9(4) | 90(4) | 23(3) |
| METHOD 2 (806 NM) | 380(13) | 112(11) | 32(3) |

Table 4.2: **Transmission and loss of the cavity mirrors.** Values of the cavity mirror transmission coefficients $T_{1,2}$ and cavity internal loss $L = L_1 + L_2$. As a reminder, $\alpha_{loss} = L + T_1$. Method 1 corresponds to a direct measurement of laser power transmitted through the bare mirrors; Method 2 follows the protocol described in Refs. [79] and [42].

MEASUREMENT OF THE CAVITY BIREFRINGENCE: Cavity birefringence is generally caused by a path-length difference between the polarisation eigenmodes of a cavity, lifting their frequency degeneracy. If the polarisation of a photon emitted into the cavity does not coincide with one of these eigenmodes, the photon polarisation is in a superposition of the cavity eigenmodes. These eigenmodes will acquire a phase difference at rate $\omega_b$, the energy difference between them. This phase difference accumulates during the round trips in the cavity and results in an effective rotation of the polarisation state. If the phase difference accumulates faster than the cavity decay rate, a time-dependent polarisation will be observed [80, 81]

As explained in Sec. 3.3, ion-photon entanglement is generated using the polarisation degree of freedom of single photons. Birefringence on the order of the cavity decay rate $\kappa$ could therefore lead to a loss of coherence in the generated state when averaging the photonic state across the extent of its temporal wavepacket. By averaging the photonic polarisation state across its temporal wavepacket, the purity of the generated entangled state would reduce, since every detected photon has spent a different time in the cavity and so has experienced a different degree of polarisation rotation.

During the construction of the cavity, special care was taken to keep the birefringence as low as possible and well below the cavity decay rate. First, a rotational alignment of one cavity mirror with respect

to the other was found for which the lowest amount of birefringence was measured. The thus aligned mirrors were then glued into mirror holders, keeping the stress induced by the glue on the mirrors as low and evenly distributed as possible, as explained in Sec. 4.1.2.

For a birefringence smaller than the cavity linewidth $2\kappa$, the frequency splitting $\omega_b$ cannot be reliably resolved in a transmission spectrum of the cavity. A different method, described in Ref. [82], was therefore employed with which even low degrees of birefringence ($\omega_b \ll 2\kappa$) can be determined. Here, cavity ringdown measurements are performed, as described previously, but for specific input polarisations and in the presence of polarisation analysis of the cavity output light. The frequency splitting of the polarisation eigenmodes can then be observed as a beating during the cavity decay, effectively modulating the cavity decay time $\tau$.

The measurement was performed in the following way. The cavity decay signal is projected onto a linear polarisation analyser (PA), consisting of a polarising beam splitter (PBS) and half-wave plate (HWP), orientated at an angle $\gamma$ relative to the slow axis of the birefringent cavity. In the presence of only small birefringence, the cavity ringdown signal still follows an exponential decay with effective decay time $\tau_{\text{eff}}$, which is measured in the same way as described previously via the cavity ringdown method. When exciting the cavity with circularly polarised light, the following dependence can be observed:

$$\tau_{\text{eff}}(\theta) = \tau(1 \mp \omega_b \tau \sin[4(\theta - \alpha)])^{-1}. \tag{4.2}$$

Here, $\theta = \alpha + \gamma$ is the angle the PA makes with the x-axis in the laboratory frame (an axis perpendicular to the cavity axis) and $\alpha$ is the angle the slow cavity-axis makes with the x-axis.[10] The minus sign is used for left-handed (LH), the plus sign for right-handed (RH) input polarisation.

Fig. 4.4a shows two cavity ringdown signals of the final (in-vacuum) cavity, for PA angles $\theta$ that correspond to the largest modulation of the decay time $\tau$. In Fig. 4.4b, an example curve of a cavity ringdown signal is displayed in the case of strong cavity birefringence, for the same pair of mirrors but with different gluing. Here, the modulation of the cavity decay is so strong that the decay does not follow a simple exponential dependence and the method explained above cannot be applied. The signal in Fig. 4.4b, and others like them, were obtained regularly during the assembly phase of the cavity, where the birefringence resulted from stress induced by glue that was used to fix the mirrors to holders (Sec. 4.1.2). Fig. 4.4c shows a measurement of $\tau_{\text{eff}}(\theta)$ for our in-vacuum cavity, for LH and RH input light polarisation, together

10 A coordinate system can be found in Ref. [82], though the absolute orientation is not important for us. Note that a factor of 4 instead of 2 in the argument of the sine in Eq. 4.2 is used compared to [82] since the PA consists of a HWP and PBS instead of a polariser (a HWP rotates the polarisation vector through an angle $2\theta$).

*Measured cavity birefringence*

with a fit to the model of Eq. 4.2. A birefringence $\omega_b/2\pi = 13.8(5)$ kHz was determined from the average of the model parameters of each dataset. This compares to the cavity decay rate $\kappa = 70(2)$ kHz.

The method described above was further used when selecting a cavity mirror pair (Appendix A.2) and during the assembly phase of the cavity (Sec. 4.1.2) for determining the amount of stress-induced birefringence due to the gluing.

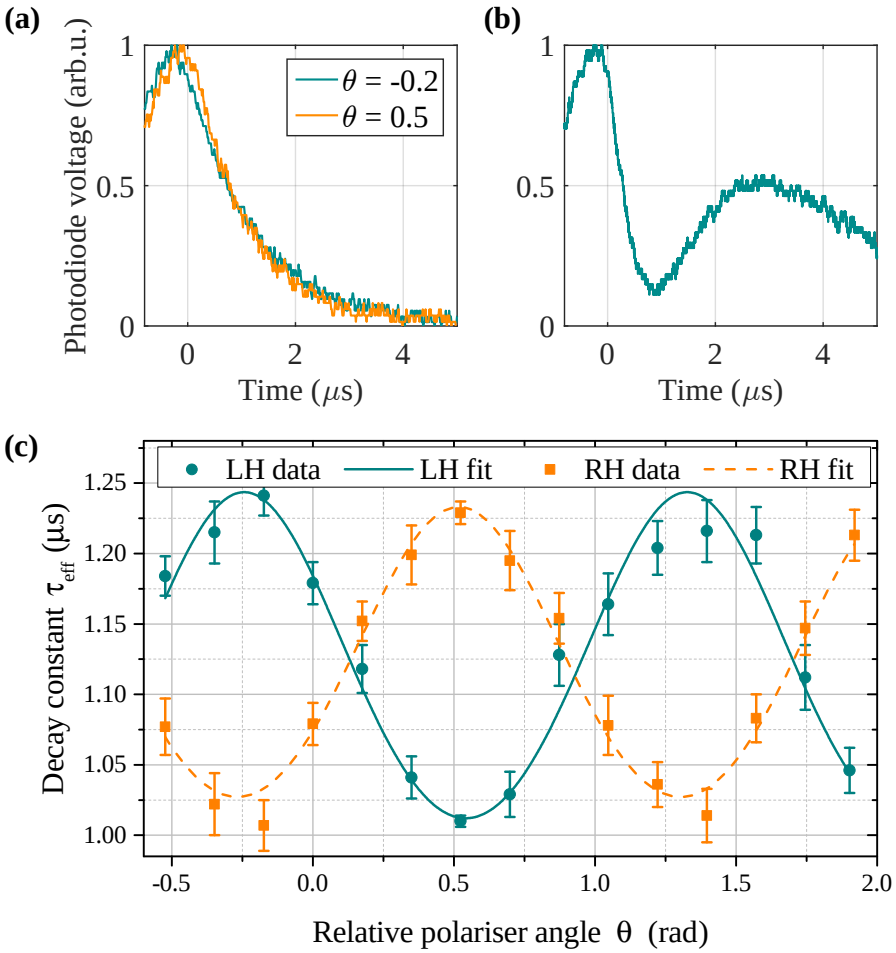


Fig. 4.4: **Cavity birefringence measurement. (a)** Cavity ringdown signals of the final, in-vacuum cavity, in the presence of polarisation analysis of the cavity output light. The indicated polariser angles θ correspond to the angles in subpanel (c) for LH input light polarisation. **(b)** Cavity ringdown signal in the presence of polarisation analysis of the cavity output light and in the case of strong cavity birefringence. **(c)** The effective cavity decay time constant $\tau_{eff}$ is plotted as a function of θ, the angle defined by the PA relative to the laboratory x-axis. Each data point corresponds to the average of five closely spaced, consecutive measurements taken with a repetition rate on the order of 1 Hz. Subpanel (a) displays two example curves of ringdown signals from which $\tau_{eff}$ is determined via a fit to the decaying slope. Error bars correspond to $\pm 1\sigma$ standard deviation, dominated by shot-to-shot fluctuations.

### 4.1.2 *Cavity assembly*

CAVITY MIRRORS: The mirror substrates have a diameter of 7.75 mm and a thickness of 3 mm (a drawing is shown in Appendix A.1). The super-polishing of the surfaces of the mirror substrates[11] was performed by Perkins Precision, Boulder, achieving a root mean square (RMS) roughness of 1.0(2) Å and 1.5 ppm (parts per million) scattering losses per substrate, as measured by them on a test piece from the batch.

Mirror coating via ion beam sputtering was performed by Advanced Thin Films (ATF). The coatings are composed of $SiO_2 - Ta_2O_5$ dielectric stacks with the topmost layer $SiO_2$. The mirror with transmission coefficient $T_1$ was designed with a target value of 2 ppm at 854 nm, the other mirror with transmission coefficient $T_2$ had a target value of 100 ppm. Coating profiles are provided in Appendix A.2. The target value for $T_2$ was chosen to lie between the values of $T_2^{opt}$ and $T_2^{opt.pure}$ (see Sec. 2.2.2), given the value of $\alpha_{loss} < 12$ ppm at 854 nm that was expected from the manufacturer's specifications ($T_1 = 2$ ppm and $L_{1,2} < 5$ ppm) and given the value of $w_0 = 13.2(8)$ µm achieved in the UIBK setup [36, 42]. In order to be able to lock the cavity to a laser at 785 nm, the mirror coatings were ordered with an additional target transmission of $T_{1,2} \approx 100$ ppm at that wavelength. The backsides of the mirrors are anti-reflection (AR) coated (specified reflection <0.1% for 760-890 nm).

Obtaining the cavity mirrors required a long process of ordering and communication with the manufacturers, involving multiple coating runs that failed to produce the desired targets (Appendix A.1). Within the final batches of mirrors we received, we found significant variations between different mirrors concerning their losses and birefringence. Details on the characterisation of these batches are provided in Appendix A.2. For the final cavity, a mirror pair was selected that was among the ones with the lowest losses and where the losses did not increase when aligning the cavity in the near-concentric regime (Appendix A.2). Here, we aimed for a cavity length that would result in the same cavity waist as the UIBK cavity, given our mirror ROC [see Eq. (2.5)]. Moreover, a mirror pair was chosen for which the residual birefringence of the bare (i.e., unglued) mirror pair could be minimised to well below the cavity linewidth by rotating one mirror with respect to the other.

GLUING THE CAVITY: An explosion view of the cavity components is shown in Fig. 4.5. Assembling the cavity involved multiple steps to glue the mirrors into position, such that the only tunable degree of freedom once glued is the cavity length. The used adhesives were selected under three essential aspects: one, ultrahigh vacuum (UHV)

11 Fused silica 7980 1D material

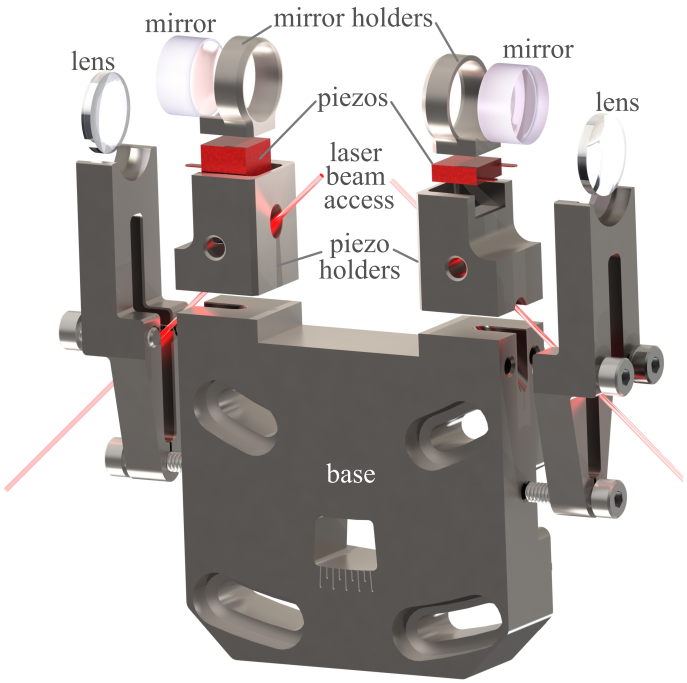


Fig. 4.5: **Components of the cavity assembly.** The mirrors are glued into mirror holders, in turn glued to piezos, in turn glued to piezo holders, in turn glued to a solid titanium base. Collimation lenses are attached to each side of the cavity. The elongated holes in the bulk of the base are for attaching the assembly to the translation stages. All shown metal is titanium.

compatibility, i.e., low outgassing, to avoid contamination of the vacuum and correspondingly shortened ion lifetimes in the trap; two, low shrinkage upon curing to avoid stress-induced birefringence in the mirrors and misalignment of the cavity during the final gluing step; three, a high glass transition temperature $T_g$ to allow for a high temperature of the final vacuum bake of the whole apparatus without destroying the cavity due to softening of the glue and subsequent misalignment.

In a first step, the mirrors were glued into mirror holders (see Fig. 4.5). The adhesive used here was the EpoTek353ND-HYB-HV which is dual curable via ultraviolet (UV) light and temperature. The stress induced by the glue on the mirrors lead to a dramatic increase of birefringence in some cases, characterised by a strong modulation of the cavity ringdown signal, as described in Sec. 4.1.1 and Fig. 4.4b. Several attempts were necessary before the mirrors could be glued without significantly raising the birefringence, as outlined in the following.

After each unsuccessful attempt, the mirrors were baked at 450 °C for several hours to remove the glue[12]. This could be done without contaminating the mirrors, i.e., the combined loss of the mirrors $L = L_1 + L_2$ did not increase by the glue removal, where L was extracted from combined measurements of the mirror transmission coefficients and cavity finesse (see Sec. 4.1.1). However, the high-temperature bake lead to changes in the transmission profiles of the mirrors[13]. At 854 nm, the value of $T_2$ changed from 127(4) ppm to 92(4) ppm (the value shown in Table 4.1), whereas the value of $T_1$ did not change measurably. At 785 nm, the value of $T_2$ changed from 85(4) ppm to 145(4) ppm and the value of $T_1$ changed from 143(4) ppm to $> 2 \times 10^3$ ppm. This significant change in the value of $T_1$ is likely due to the fact that the wavelength of 785 nm lies at the edge of the high-reflective region of the coating, where the dependence of the transmission on the coating-layer thickness is steepest. A summary of these transmission measurements and the coating profile of the mirrors can be found in Appendix A.2. The transmission values were obtained via the method using a laser and a power meter presented in Sec. 4.1.1 (Method 1). As a consequence of this transmission change, a different wavelength of 806 nm had to be selected for locking the cavity (see Sec. 4.1.3).

The final gluing of the mirrors into the mirror holders consisted in applying glue between mirror holder and mirror substrate in three equidistant spots around the back of the substrate. Care was taken to keep the substrates centred in the holders to keep the amount of required glue consistent in each spot. A gap of 30-40 µm was adjusted between the two components with the help of distance plates. Following an initial UV cure to fix the mirrors in place, the glued parts were air-baked at 150 °C for several hours, after which a birefringence of 6.4(6) kHz was recorded. This value compares to a birefringence of 6(1) kHz, measured for the unglued mirrors. The birefringence was measured with the method described in Sec. 4.1.1 As specified in Sec. 4.1.1, a birefringence of 13.8(5) kHz was measured for the final, in vacuum cavity. A possible explanation for this additional birefringence is stress accumulated during the several temperature cycles involved in assembling the cavity (see below).

For gluing all the other components together (see Fig. 4.5), the epoxy Masterbond EP21TCHT-1 was used, which was cured at room temperature followed by a high-temperature air-bake to raise $T_g$. First, the mirror holders were glued to piezos for cavity-length stabilisation,

12 The temperature was ramped to 450 °C at a speed of 5 °C/min, held constant for 2 h, and then ramped down again over night. At this temperature, which is well above the glue's degradation temperature of 388 °C, the glue evaporated.

13 The mirrors had been annealed by the manufacturer ATF, albeit at a lower temperature than our bake. ATF annealing cycle: ramp up to 300 °C in 1 h; dwell at 300 °C for 1 h; cool down to room temperature (no forced cooling).

which were in turn glued to titanium piezo-holders.[14] In a second step, one of the piezo holders was glued to one side of the titanium base (with a glue-layer thickness of about 40 μm).[15] In a third step, the free piezo holder (not attached to the base), carrying one of the mirrors, was mounted on translation stages with micrometer screw gauges and the cavity was aligned in the final, near-concentric cavity configuration (the rest of the assembly was mounted on a solid steel pillar via the cavity base). In this configuration, the free piezo holder ended up with a gap of hundreds of microns between piezo holder and base. A metal spacer was therefore inserted into that gap in order to reduce the required amount of glue and thus avoid a misalignment of the cavity during curing: if the glue shrinks in each dimension by some percentage of its length during curing, then the absolute length change is smaller for smaller layers.[16] In a final step, the free piezo holder was glued to the titanium base spanning the cavity length: the piezo holder was translated up, the spacer with glue on both sides inserted into the gap, and the piezo holder was lowered back onto the base until the cavity was realigned. The assembly was then left to cure at room temperature for two days, all the while monitoring the cavity finesse. At the start of the two days, the measured finesse was $60(1)\times10^3$ and no measurable drop was observed. Finally, the assembly was air-baked at 110 °C for another 1-2 days.[17] A finesse of $59(1)\times10^3$ was measured after the curing and bake was complete (see the finesse timeline in Fig. 4.3).

To complete the cavity structure assembly, lenses[18] were then attached to either side of the cavity to allow for mode matching of laser light sent into the cavity and collimation of the cavity output mode (Sec. 4.5). The lenses were glued to their holders using the glue EpoTek353ND-HYB-HV[19] and bolted to the cavity base (see Fig. 4.5).

14 Curing cycle (as recommended by the company): room temperature for approximately 5 h; ramp to 80 °C, stay for 7 h; ramp to 125 °C, stay for 18 h; cool down to room temperature (no forced cooling). The temperature was ramped at 1 °C/min.

15 Curing cycle: room temperature for approximately 1 day; ramp to 80 °C, stay for 7 h; ramp to 125 °C, stay for 18 h; cool down to room temperature (no forced cooling). The temperature was ramped at 0.5 °C/min.

16 Indeed, in a first gluing attempt, without metal spacer, the cavity misaligned due to the glue shrinkage during curing.

17 Curing cycle: ramp to 110 °C at 0.2 °C/min, stay for 17h, ramp down to room temperature at 0.1 °C/min. The peak temperature of 110 °C was chosen to lie below the previous curing temperature in order to reduce the risk of misalignment due to softening of the glue (the exact value of $T_g$ is not known).

18 Lattice Optics B-PX-8-20-780-866 (BK7 material, 8 mm diameter, f = 20.34 mm at 800 nm, AR coating at 780-866nm); surface figure: λ/10 at 632.8 nm; surface quality: 10-5 scratch-dig

19 Curing cycle: UV cure to fix lenses in place; then: ramp to 260 °C at 1 °C/min, stay for 15 h, cool down to room temperature (no forced cooling).

TRANSLATION STAGES: The cavity is mounted on a system of piezo-based translation stages[20] for 3D positioning of the cavity with respect to the trap. The stacking of the stages is visible in Fig. 4.6. A translation stage for vertical positioning was chosen over the tripod of screw gauges in the UIBK setup [42] to allow for a better repeatability and a decreased complexity of the positioning process. All stages have integrated resistive position encoders with a specified repeatability of 1-2 µm (this is in contrast to the stages in the UIBK setup, used for horizontal alignment, which do not have encoders; cf. Ref. [36] Sec. 4.12). Each of our stages can be operated in two positioning modes. For coarse positioning, there is the stick-slip mode. Here, a saw-tooth signal with an amplitude of tens of Volts, applied to a piezo stage from a separately purchased controller[21], effectuates a stick-slip motion with few-micron step size. The stick-slip mode, with a range of a few millimetres, was used to align the cavity waist with the ion (see Sec. 5.1). In the fine-positioning mode, a DC voltage is applied to a piezo stage, allowing for sub-nm displacements. The fine-positioning mode is used for positioning the ion in an antinode of the cavity standing wave. Here, a voltage of up to $\pm 9$ V from a battery—manually adjustable via a homebuilt potentiometer-based voltage divider, the so-called *"twiddle stick"*—is applied to the stage for translation along the cavity axis, allowing for a range of up to 1 µm, approximately. Regular adjustment of the cavity position via the twiddle stick is required in order to compensate for drifts caused by temperature changes. Especially after operating the atomic oven (Sec. 4.2), adjustments are needed until the relative position between cavity and ion has settled: assuming a usual ion-loading time of about 5-10 min, about 1 hour after the oven was turned off adjustments in intervals of 10-30 min are necessary. After about four hours, the position has settled.

TRAP-CAVITY ANGLE: For the final integration with the ion trap, a 4-5° deviation from 90° was intended for the angle between cavity axis and trap axis (south↔north). Following Ref. [83], such an angle, and the resulting projection of the trap axis onto the cavity axis, allows in principle for a selective coupling of two ions to the cavity field. By adjusting the ion-ion distance via the axial trap confinement (Sec. 4.2), either both ions can be coupled to cavity antinodes or one of the ions can be placed in a cavity antinode and the other one in a cavity node, thereby hiding it from the interaction with the cavity field. During

20 Attocube, ANPx311/RES/UHV for translation in the vertical (south↔north) dimension and along the cavity axis (east↔west), ANPx321/RES/UHV for horizontal translation perpendicular to cavity axis (front↔back). This latter translation stage has a larger travel range (15 mm) than the others (6 mm) and was chosen for the possibility of moving the cavity out of the way of optical access to the trap centre in the direction along the east↔west axis.

21 Attocube ANC350

the process of mounting the cavity on the translation stages, the angle was set in the following way. First, the angle between cavity axis and cavity base (see Fig. 4.5) was roughly estimated to be 4° by measuring the difference in heights of an input laser beam coupled to the cavity and the cavity output mode.[22] Using the scale imprinted on the cavity base (see Fig. 4.5), a value of 0° was set for the angle between the symmetry axis of the cavity base and vertical (south↔north) axis. A 4.1(1)° deviation from the 90° angle between cavity and trap axis was extracted in later measurements, as detailed in Sec. 5.1.

VACUUM INTEGRATION: The system of cavity and translation stages is mounted on the bottom CF100 flange of the vacuum chamber, together with various feedthroughs needed for the electrical connections (Sec. 4.3) and an atomic oven. Mounting of the translation stages and the atomic oven was performed by V. Krcmarsky. A photograph, taken before insertion into the vacuum chamber, is shown in Fig. 4.6. After integrating the cavity into the vacuum chamber, the combined setup was submitted to a final vacuum bake at 80°C for one week (see Sec. 4.3 and the upcoming thesis of V. Krcmarsky [84]). This relatively low temperature (vacuum-baking temperatures in ion-trapping experiments in Innsbruck are usually above 180°C) was chosen so as not to exceed the specified glass transition temperature $T_g \approx 95$ °C of the glue used in the piezo stacks[23] and reduce the risk of cavity misalignment during the bake.

### 4.1.3 *Cavity length control and lock*

CAVITY LENGTH CONTROL: Precise control over the cavity length is necessary in order to set and maintain the cavity-ion detuning. For this purpose, each mirror sits on a stack of shear piezos. There is a fast[24] and a slow[25] piezo stack, composed of one and four piezoelectric shear plates, respectively, which can be driven by a maximum of ±320 V. The fast stack supports the mirror with transmission coefficient $T_1$, the slow stack supports the mirror with transmission coefficient $T_2$. By measuring the voltage required to change the cavity length by one FSR, the range of the fast stack was estimated to be 2.1(3) nm/V and the range of the slow stack to be 5.8(4) nm/V. The uncertainty (mean deviation) is derived from multiple measurements and is dominated by piezo hysteresis. The piezos are each connected to two SHV feedthroughs via Kapton-insulated, wire-mesh-shielded cables. Both

22 It is not known what causes this angle, but the angle is the reason for the gap between piezo holder and base on one side of the cavity, observed during the gluing process.
23 Unfortunately, no information about the type of glue used in the piezo stacks was disclosed by the manufacturer. From the specified $T_g$, I suspect that the glue Epotek-353-ND was used.
24 Noliac NAC2402-H1.7-A01 UHV Version
25 Noliac NAC2402-H3.4-A01 UHV Version

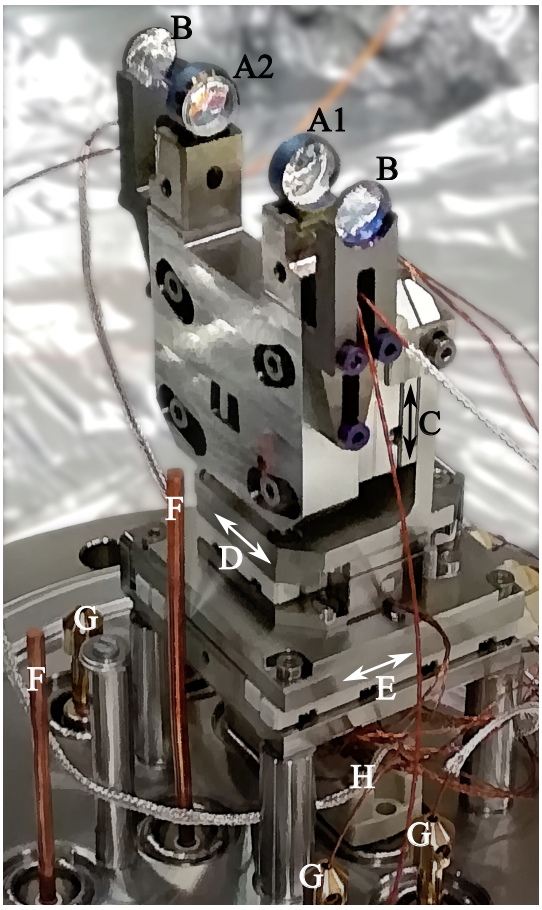


Fig. 4.6: **Photograph of the cavity assembly.** A1: cavity mirror with transmission coefficient $T_1$ glued to a mirror holder, glued in turn to the fast piezo stack; A2: cavity mirror with transmission coefficient $T_2$ glued to a mirror holder, glued in turn to the slow piezo stack; B: collimation lenses; C: south↔north translation stage; D: east↔west translation stage; E: front↔back translation stage; F: oven electrodes (oven not mounted); G: connectors to the secure high voltage (SHV) feedthroughs for the cavity piezos; H: connector to the D-sub 15 feedthrough for the translation stages. The wires for voltage control of the piezo stacks can be seen coming through slits in the titanium holders for the collimation lenses (B).

piezos are used for stabilising the cavity length, as explained in the next paragraph ("Cavity Lock"). Additionally, an offset voltage applied to the slow piezo is used for bringing the CMRT on resonance. This offset voltage can be manually adjusted via a potentiometer and is derived from a (homebuilt) high-voltage amplifier, capable of supplying $\pm 350$ V, which corresponds to a cavity length change of several FSRs. The output of the amplifier is filtered by a second-order low-pass filter with a cut-off frequency of around 5 Hz (homebuilt).

CAVITY LOCK: The cavity length is stabilised via the Pound-Drever-Hall (PDH) method [85] to a laser at 806 nm, the transfer-lock laser, which is in turn stabilised to an external reference cavity. The stabilisa-

tion of the 806-nm laser, as well as the reference cavity, are described in Sec. 4.4.5. The laser enters the cavity through the mirror with transmission $T_1$. The 806-nm wavelength lies far from any transition in $^{40}Ca^+$ to reduce AC Stark shifts on the atomic transitions.[26] Moreover, the cavity is locked to a $TEM_{01}$ mode and the ion is placed in the central intensity minimum to further reduce AC Stark shifts. A schematic of the cavity lock setup is shown in Fig. 4.7. A 7.2-MHz "local oscillator" signal from a function generator is sent to both an EOM[27] in the beam path before the cavity and to a mixer. The phase-modulated light from the EOM that is reflected from the cavity is detected with a photodiode, whose signal is mixed down with the local oscillator signal to generate the error signal. The error signal is filtered by a 50-kHz low-pass filter before being fed to a proportional-integral-derivative (PID) controller[28] with two outputs. The slow output is sent to the high-voltage amplifier that drives the slow piezo as described above, which amplifies the signal by a factor of 25. The fast output is applied to the fast piezo after passing a 2-kHz second-order low-pass filter (homebuilt). This filter was found to be necessary for suppression of acoustic resonances of the cavity and its mount.

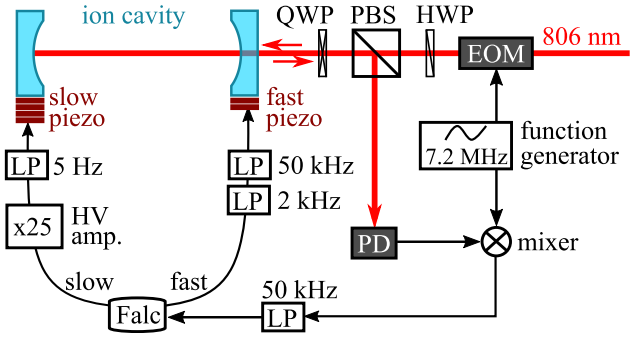


Fig. 4.7: **Setup for stabilising the ion-cavity length.** The cavity is locked via the PDH method to a laser at 806 nm, which is in turn locked to an external reference cavity (Sec. 4.4.5). Feedback from the fast output of a Toptica FALC110 PID module is applied to the fast piezo, the amplified slow output drives the slow piezo. PD: photo diode. LP: low-pass filter with cut-off frequency as indicated.

The performance of the lock was estimated in the following way. The cavity length was scanned across a $TEM_{01}$ resonance of the 806-nm locking laser via a triangular signal applied to one of the piezos and a time trace of the error signal was recorded (Fig. 4.8a). The sidebands at the known frequency of the local oscillator serve as a reference to convert the time trace to units of frequency. In a next step, the slope $D = 1.0(3)$ V/MHz of the scanned error signal was extracted from a linear fit to the central part of the error signal (Fig.

26 For a typical input power of the 806-nm laser of about 0.1 mW, the AC Stark shift induced by the resulting intracavity laser field on the $D_{5/2}$ manifold can be up to around 1 MHz (Sec. 5.1 includes a detailed description and a precise measurement).

27 QiOptiq PM-C-BB

28 Toptica FALC110; the derivative (D) part of the feedback is disabled

4.8b). The uncertainty is due to shot-to-shot fluctuations of repeated measurements. With the standard deviation of the locked (in-loop) error signal $\Delta U_{locked} = 9$ mV (Fig. 4.8c), the width of the frequency excursions of the lock was estimated as

*Measured cavity-lock jitter*

$$\delta\nu_{lock} = \frac{\Delta U_{locked}}{D} = 9(2)\ \text{kHz}.$$

This cavity-lock jitter, which is included in the numerical simulations presented in Ch. 6, introduces phase noise and effectively broadens the CMRT. Compared to the half width ($\kappa$) of about 0.33 MHz of the cavity at 806 nm, we find that the cavity can be locked to about 3% of its linewidth at 806 nm.

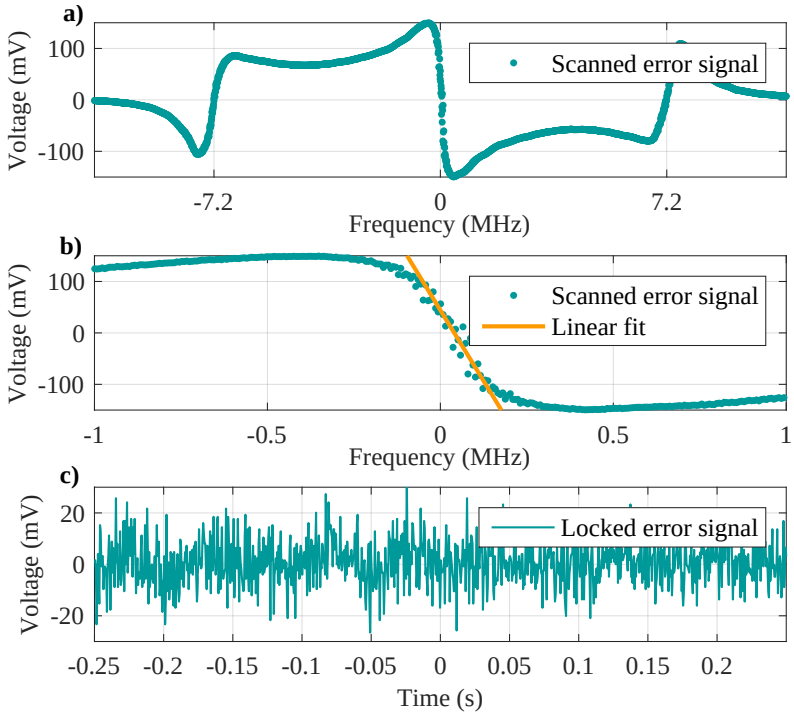


Fig. 4.8: **Estimating the in-lock frequency stability of the cavity. a)** Measured error signal when scanning the cavity across a $TEM_{01}$ resonance of the 806-nm locking laser. **b)** Linear fit to the central region of the error signal in (a). **c)** Measured time trace of the locked-cavity error signal.

## 4.2 ION TRAP

A linear Paul trap [86] is used to confine ions in three dimensions, combining long storage times with an excellent isolation of the ion from the environment. The axial direction of the trap, or trap axis, is the direction along which ion strings can form. Two tip electrodes, or *"endcaps"*, at both ends of the trap axis generate a static electric field in

order to confine the particle in that dimension. The radial direction is perpendicular to the trap axis in cylindrical coordinates. Confinement in that dimension is provided by an oscillating quadrupole field generated by four radial electrodes symmetrically arranged around the trap axis. Here, a radiofrequency (RF) voltage at frequency $\omega_{RF}$, applied between two diagonally opposite electrodes, gives rise to (harmonic) ponderomotive potentials in the radial directions.

The ion trajectory in the dynamic trap can be described by a set of Mathieu differential equations and consists of harmonic oscillations at frequencies $\omega_r$ (radial) and $\omega_z$ (axial), the secular motion, superposed with driven excursions at the RF frequency $\omega_{RF}$, called micromotion [64, 87]. If micromotion is neglected, the secular motion can be approximated by that of independent harmonic oscillators with frequencies $\omega_{r,z}$. As detailed treatments of trapped-ion dynamics are readily available in many places in the literature (e.g., Refs. [64, 73, 87]), the remainder of this section is dedicated to the specifics of the ion trap designed during this PhD work.

The geometry of our ion trap is based on a design used in several experimental setups in Innsbruck, including the UIBK setup [42]. A 3D-rendered image of our trap is shown in Fig. 4.9. As shown in the figure, the four blade-shaped radial electrodes have a length of 6 mm and a diagonal spacing of 1.6 mm, resulting in 0.8 mm radial ion-electrode distance. The endcaps are separated by 5 mm. Our trap has three pairs of what we refer to as compensation electrodes. Two of these pairs are held at non-zero DC voltages which act to cancel stray electric fields that displace the ion from the RF-null position. The third pair, between cavity mirror and ion, is held at ground and provides shielding of the trap centre from possible stray electric fields originating from surface charges on the cavity mirror or the cavity piezo. Finite element method (FEM) simulations of our trap with the Comsol Multiphysics software suggest a reduction of stray fields by a factor of ten compared to the case without any compensation electrodes in the direction of the mirrors. While no systematic measurements have been conducted to that end, no effects on the ion due to stray fields were registered at any point during the experiments presented in this thesis.

Top and bottom trap bases, which are electrically isolating, hold the trap electrodes in place. The material used here is sapphire as opposed to Macor in older trap designs, e.g., the UIBK setup [42]. Due to the higher heat-conductivity and lower RF-loss-tangent of sapphire, significantly less heat is generated when operating the trap [88]. The electrodes are made of titanium and are coated with a gold layer of 2-3 µm thickness via electroplating, which was performed by Kirill Lakhmanskiy at the UIBK.

The trap is attached at the top sapphire base to the top flange of the vacuum chamber via a rigid titanium structure (see Fig. 4.11). The top flange also contains the copper-wire feedthroughs (Sec. 4.3)

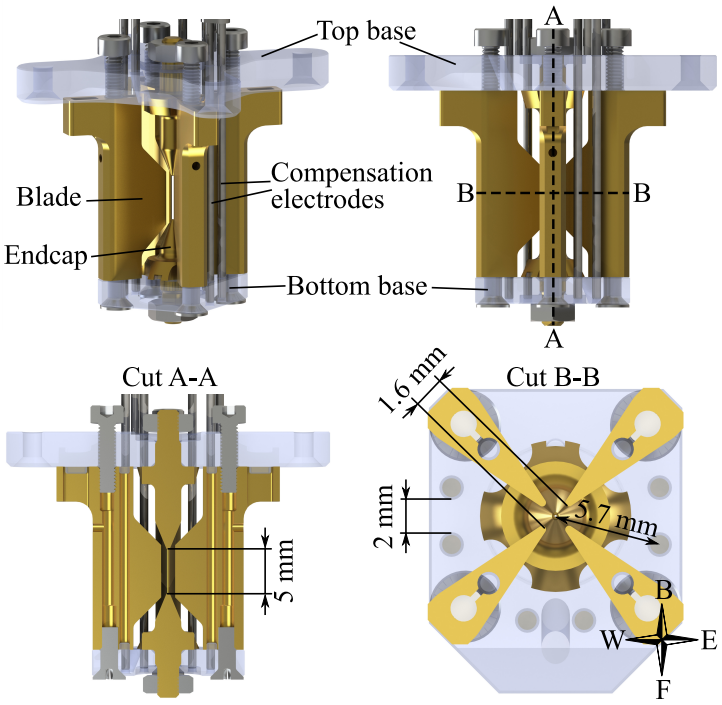


Fig. 4.9: **Drawing of the ion trap.** The four blade-shaped electrodes of the linear Paul trap generate the dynamic radial potential, the two endcap electrodes provide confinement along the axial dimension. The electrodes are made of gold-coated titanium and are bolted to a top and bottom base made of sapphire. Elongated pins in the top base allow for a precise alignment of the blades. The blades have a ROC of 0.2 mm. Two pairs of rod electrodes (front and east) are used for micromotion compensation, the third pair is grounded and provides shielding of the trap centre from the cavity mirror in that direction (east↔west).

for the electrical connections of the various trap electrodes. The trap was assembled and mounted on the flange by V. Krcmarsky [84]. A photograph of the integrated trap-cavity system under vacuum can be seen in Fig. 4.10.

One pair of diagonally opposite radial electrodes is driven with an RF signal of 23 MHz. A helical resonator attached to the electrodes amplifies the signal. The coupling between frequency source[29] and resonator coil is done via a sliding contact that is attached to a threaded Teflon cylinder screwed into the resonator coil. In this way, matching the impedance to the trap can be accomplished by simply screwing the Teflon cylinder further in or out while the grounding shield of the resonator can remain closed. The resonator was asssembled and characterised by V. Krcmarsky; more information can be found in his upcoming thesis [84]. Radial trap frequencies of $\omega_{r1}/2\pi = 2.40$ MHz and $\omega_{r2}/2\pi = 2.44$ MHz were measured via spectroscopy of the

*Trap frequencies*

29 Rohde&Schwarz SMC 100 A, amplified by an RF amplifier MiniCircuits LZY-22+

ion's motional sidebands on the 729-nm transition. The splitting is due to a constant voltage of 1.5 V applied from a battery to the other pair of radial electrodes. Non-degenerate radial modes are important for efficient Doppler cooling, as the symmetry break in the radial plane leads to radial motional modes that both have a projection onto the cooling beam's propagation direction [69]. Typical DC voltages applied to the endcaps are $1.0 \times 10^3$ V, resulting in a measured axial trap frequency of $\omega_z/2\pi = 0.92$ MHz. The voltages applied to the endcaps and compensation electrodes are generated by a stable high-voltage source[30] ($\Delta V/V \approx 10^{-5}$). Low-pass filters (made by our in-house electronic workshop) with a cut-off frequency of 1.6 Hz are present directly at the vacuum feedthroughs.

Typical ion lifetimes in our trap are on the order of one day. In order to load a single $^{40}Ca^+$ ion into the trap, a tube containing pure calcium—the calcium oven[31]—is resistively heated by a current of 3.6 A. The oven is mounted on the bottom flange in a rigid structure (visible in Fig. 4.1). Metal plating surrounding the oven shields the cavity mirrors and the trap electrodes from the calcium flux emitted from the oven as well as from the heat radiation (cf. Ref. [36] Sec. 4.12). The beam of calcium atoms is collimated by a hole in the metal shield and another hole in the bottom sapphire base before entering the trapping volume, where the atoms are ionised by laser light at 375 nm and 422 nm. A target of pure calcium, mounted above the top base, allows for the possibility of loading ions via laser ablation, but has not been tested yet.

## 4.3 VACUUM CHAMBER

The vacuum chamber (Fig. 4.11) enclosing the cavity and ion trap is made of 316 stainless steel. Its shape can be loosely described as a "spherical cube".[32] The chamber accommodates four CF100 flanges: front, back, bottom and top, whose openings allowed for convenient access to the chamber-insides during integration of trap and cavity into the chamber. The front flange consists of a CF100 viewport that allows for a clear view into the chamber and in principle for shooting an ablation laser onto the calcium target. The chamber back-side is fitted with a recessed (inverted) viewport[33] that allows the placement of an objective (Sec. 4.6) close to the ion trap while still keeping it outside the vacuum (distance trap centre to front surface around 58 mm). The objective collects the ion fluorescence for atomic state detection (see Secs. 3.4 and 5.3).

30 ISEG box EHS 82 20x-F
31 Alvatec special design AS-3-Ba30/Ca40-C (Barium 30 mg + Calcium 40 mg)
32 The chamber was manufactured by Kimball Physics and is a custom build based on the MCF600-sphcube model.
33 UKAEA; 40 mm clear aperture

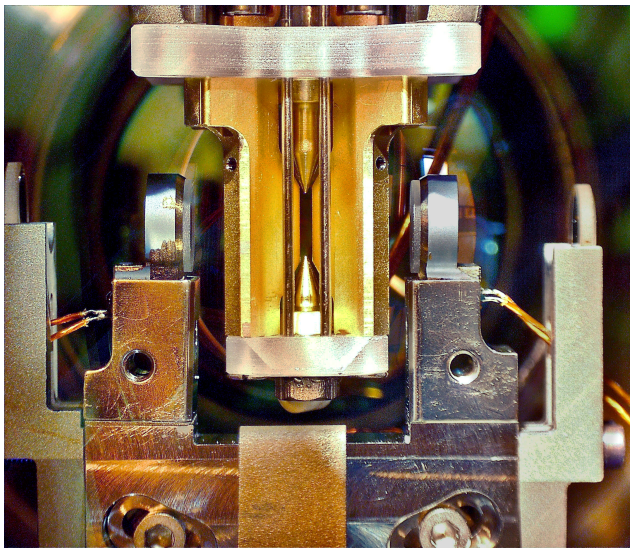

Fig. 4.10: **Photograph of the integrated trap-cavity system.** View through the front CF100 viewport, showing the linear Paul trap vertically mounted between the cavity mirrors. Also visible are the collimating lenses to either side of the cavity, as well as electrical wires leading to the piezos below the mirrors. The atomic oven is mounted beneath the metal plating visible at the bottom centre of the picture.

The bottom flange, on which the cavity assembly and oven are mounted, contains the vacuum feedthroughs for electrical connection to the translation stages[34], cavity piezos[35] and oven[36]. The top flange, to which the trap is attached, holds the feedthroughs for electrical connection to the various trap electrodes (RF[37] and DC[38] signals). The helical resonator sits on the top flange and is connected to one of the RF feedthroughs.

The east and west side of the chamber provide optical access to the cavity through two CF40 viewports[39]: laser light (mainly for the cavity lock, Sec. 4.1.3) can be coupled to the cavity through the east viewport, while the single-photon path from cavity to detectors runs through the west viewport (details on the optics surrounding the chamber are presented in Sec. 4.5). Four CF16 viewports are installed at an angle of 25° to each side of the east↔west axis, but have not been used as yet. The remaining facets of the chamber are mostly fitted with CF40 viewports, providing optical access for the various laser beams (Sec. 4.4). Details on the viewports and their coatings are provided in Ref. [84]. To lift the degeneracy of the Zeeman levels (Sec. 3.2), a pair of rings of permanent magnets is mounted on the bottom-front and top-back CF40 viewports (see Fig. 4.11). The magnets generate

34 SubD-15
35 SHV-5
36 One pair of copper pins with 2.4 mm diameter
37 Two copper pins with 6.4 mm diameter
38 Four pairs of copper pins with 1.3 mm diameter
39 UKAEA; specified surface flatness $\lambda/10$, scratch-dig 20-10

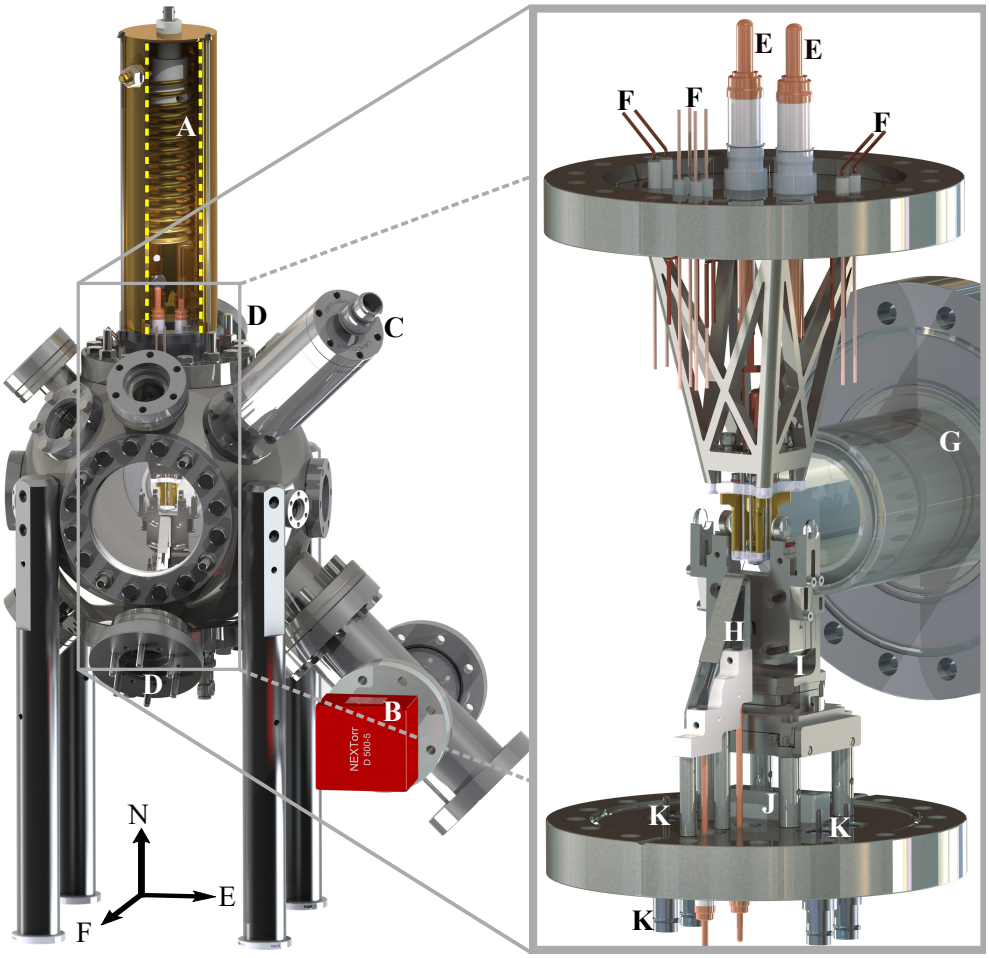


Fig. 4.11: **Model of the vacuum chamber containing the cavity and trap.** The chamber is viewed from the front. A: helical resonator; B: combined ion pump and non-evaporable getter (NEG); C: additional NEG intended as a backup (not yet activated); D: rings of permanent magnets; E: RF feedthroughs; F: DC feedthroughs; G: inverted viewport; H: atomic oven; I: cavity assembly on translation stages; J: connector to the SubD-15 feedthrough for the translation stages. K: SHV feedthroughs for the cavity piezos; Top, bottom, front and back flanges are CF100.

a magnetic field of 4.23 G at the trap centre, resulting in a Zeeman splitting within the $D_{5/2}$ manifold of $\delta_Z/2\pi = 7.1$ MHz.

The north-east side of the chamber is connected to a CF63 four-way cross carrying a combined ion pump and NEG[40], a CF40 all-metal valve, and a CF63 viewport in line-of-sight of the trap centre. The vacuum vessel is mounted onto a two-level breadboard support structure that is located inside a magnetic field shielding enclosure[41]. Sorbothane pads[42] between breadboard and optical table are intended for vibration isolation.

40 SAES NEXTorr D 500-5
41 Custom design, manufactured by Magnetic Shields UK
42 five cylinders of 3.8 cm height and 5 cm diameter, 70 Durometer

| WAVEL. | MAKE, MODEL | LABEL | PURPOSE |
|---|---|---|---|
| 375 nm | Toptica iBeam smart | 375 | photo-ionisation, non-resonant second stage |
| 423 nm | Toptica DL-Pro | 423 | photo-ionisation, resonant first stage |
| 397 nm | Toptica TA-SHG Pro | 397-$\pi$ | Doppler cooling, state detection |
| | | 397-$\sigma$ | optical pumping |
| 866 nm | Toptica DL-Pro | 866 | repumping from $D_{3/2}$ |
| 854 nm | Toptica DL-Pro | 854 | repumping from $D_{5/2}$ |
| 806 nm | Toptica DL-Pro | 806/transfer-lock laser | ion-cavity lock |
| 729 nm | Coherent 899 | 729-rad | qubit manipulation and sideband cooling of the radial |
| | | 729-ax | and axial mode |
| 393 nm | $M^2$ Solstis-1600-PSX-R with ECD-X doubling stage | 393/drive laser | drive laser for the CMRT |

Table 4.3: **Listing of all laser systems used in this work** for illuminating the ion or locking the cavity. For their directions in the setup, see Fig. 4.1.

The chamber containing cavity and trap was submitted to a one-week vacuum bake at a temperature of 80 °C, while pumping with a turbomolecular vacuum pump. Further details on the vacuum bake can be found in Ref. [84].

## 4.4 LASER SYSTEMS

An overview of the laser systems used in this work is provided in Table 4.3. The labels given in the table will be used throughout the remainder of this thesis. The orientation of all laser beams for illuminating the ion or locking the cavity are shown in Fig. 4.1. Some of the lasers (729 nm, 423 nm, 375 nm) are shared with another project in the same

lab, while others (transfer lock laser) were the focus of a Master's thesis [89]. I will therefore only present the portions of the beam paths that are used in our setup and have not been described in Ref. [89]. All optical fibres are polarisation-maintaining (PM) unless otherwise stated. The RF sources with which the AOMs in the beam paths are driven are described in Sec. 4.7. In the figures of this section, thick coloured lines represent free-space beam paths. The labels with "+2x" indicate AOM double-pass configurations, labels with "+1x" indicate single-pass AOMs, where the "+" sign stands for the $+1^{st}$ diffraction order and the $-1^{st}$ diffraction order will be marked with a "−" sign instead.

### 4.4.1 *Lasers for Doppler cooling, state detection and optical pumping (397 nm, 866 nm, 854 nm)*

The diode lasers producing the light at 397 nm, 866 nm and 854 nm are situated on the laser table. A conceptual schematic of their setups is presented in Fig. 4.12. A few ten microwatts of laser light is branched off at the lasers' outputs and sent via singlemode (SM) fibre to the WLM for frequency stabilisation (Sec. 4.4.2). The beams from the laser heads are decoupled from the optical setups using short optical fibres that also act as a mode cleaner. After passing various AOMs that allow for switching the beams on and off, laser light is sent via optical fibres to the experiment table. The $+1^{st}$ diffraction order is used in all AOMs unless otherwise stated.

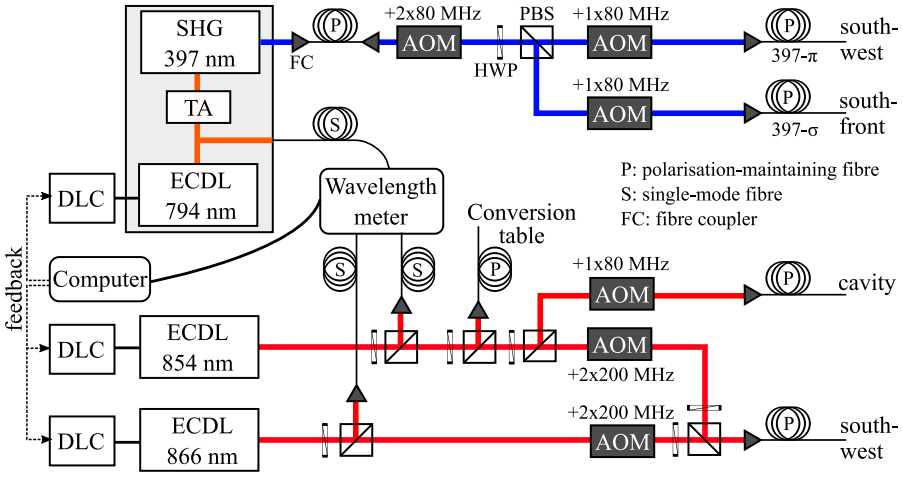


Fig. 4.12: **Conceptual schematic of lasers and beam paths for Doppler cooling, state detection and optical pumping.** The light at 397 nm is derived from fundamental light at 794 nm, created by an external-cavity diode laser (ECDL), amplified by a tapered amplifier (TA) and subsequently frequency doubled via second harmonic generation (SHG). A small fraction of light from each laser is sent to the WLM for frequency drift compensation. The lasers are controlled via digital diode-laser controllers (DLCs).

LASER AT 397 NM: The laser used for Doppler cooling, state detection and optical pumping on the $4^2S_{1/2} \leftrightarrow 4^2P_{1/2}$ dipole transition at 397 nm is a frequency doubled ECDL[43], whose fundamental laser is operating at 794 nm and amplified by a TA. A few ten microwatts of the fundamental light are sent via SM fibre to the WLM for measuring and stabilising its wavelength. A few tens of milliwatts of the available 1 W output power at 397 nm are guided via optical fibre to a setup of AOMs[44]. The light passes an AOM in double-pass configuration, shifting its frequency by +160 MHz, before being split into two paths. The first path contains the 397-$\pi$ light for Doppler cooling and state detection. After passing an 80-MHz single-pass AOM, light from the first path is guided via optical fibre to the experiment table, where it is overlapped with the repumping beams at the south-west side of the vacuum chamber. The overlapped beams reach the ion through a hole in the cavity base. The second path contains the 397-$\sigma$ light, which also passes an 80-MHz single-pass AOM and is guided to the south-front side of the vacuum chamber by another optical fibre. After passing a quarter-wave plate (QWP), the beam propagates through the chamber along the magnetic field axis. The light is $\sigma^-$-polarised and is used for optical pumping of the ion to the state $|u\rangle = |4^2S_{1/2}, m_j = -1/2\rangle$.

LASERS AT 866 NM AND 854 NM: Two ECDLs, at 866 nm and 854 nm, are used for repumping from the metastable $D_{3/2}$ and $D_{5/2}$ state manifolds, respectively (see Sec. 3.4.1). At the output of the 854 laser, a part of the light is branched off and directed to the conversion table. Another part of the 854 laser is sent to the cavity for its characterisation, described in Sec. 4.1.1. Here, an 80-MHz single-pass AOM[45] is used for switching the light on and off for the cavity ringdown measurements. Both the 854 and 866 laser fields are sent through 200-MHz double-pass AOMs[46] before being coupled to the same optical fibre and sent to the experiment table, where they are overlapped with the 397-$\pi$ beam.

### 4.4.2 *Wavelength meter and wavelength control*

The wavelength meter (WLM) used in this work is a HighFinesse WSU-10 with a specified absolute accuracy of 10 MHz and measurement resolution of 1 MHz[47]. In combination with an eight-channel mechanical switch, connected to the WLM via SM fibre, the wavelengths of all lasers (except for the 729, 375 and 423 lasers) are measured periodically at a rate on the order of 10 Hz. The WLM itself is connected

43 Toptica TA-SHG pro
44 Gooch & Housego 3080-125
45 Gooch & Housego 3080-125
46 Gooch & Housego 3200-124
47 Note that the values are specified for a device that is periodically calibrated, but a calibration was carried out only rarely during this PhD work.

to a computer via USB. For stabilising the wavelengths of the lasers at 397 nm (i.e., its fundamental at 794 nm), 866 nm and 854 nm, a control program, supplied with the device and run on the computer, is used to calculate error signals depending on the deviation from target wavelengths. Based on the error signal, the piezo voltage of an ECDL is programmatically adjusted by sending a command to the corresponding digital diode-laser controller[48] via ethernet. This all-digital control is in contrast to the usage of a digital-analog-converter (DAC), originally intended by the manufacturer, as in, e.g., Refs. [88, 90].

The feedback rate is limited by the rate at which the wavelengths are measured. The WLM lock can therefore correct for frequency drifts but is not able to narrow an ECDL's free-running linewidth of typically few hundred kHz. Considering the natural linewidth $\Gamma_{P_{1/2}} = 22.4$ MHz of the $P_{1/2}$ state, the lasers are sufficiently narrow. The drift rate of the WLM was measured by recording the wavelength of the 729 laser, which was locked to a stable reference cavity with an absolute drift of at most a few kHz over the measurement period. Over 21 hours, the WLM drifted about 3 MHz. A calculation of the mean phonon number $\bar{n}$ after Doppler cooling[49] shows that a frequency drift of twice that amount would at most increase $\bar{n}$ by 2 for any given motional mode of the ion (provided the initial detuning of the 397 cooling laser is not much smaller than the optimal detuning $\Delta = \Gamma_{P_{1/2}}/2$ for Doppler cooling). Considering the durations of less than one hour of the experiments presented in this thesis, the lasers are sufficiently stable. Moreover, ground-state cooling, whose performance is not significantly affected by the WLM lock, is performed for the experiments in this thesis.

### 4.4.3 *Photo-ionisation lasers (423 nm and 375 nm)*

The creation of singly-charged $^{40}Ca^+$ is done via two-step photo-ionisation. An ECDL[50] at 423 nm resonantly excites the $4s^2\ {}^1S_0 \leftrightarrow 4s4p\,{}^1P_1$ transition of $^{40}Ca$. A photon from a free-running 375-nm diode laser[51] provides the energy to excite the atom above the ionisation threshold of 6.1 eV [91]. The lasers and optical setups are situated on an optical table of the neighbouring *Qusim* experiment. The two lasers are overlapped on a 50:50 beam splitter (BS). Light from one port of the BS is guided to the south-back of our experiment via optical fibre (the other port is used by the *Qusim* experiment), where a TTL-controlled shutter can be used to block the light.

48 Toptica DLC Pro
49 The calculation is based on the expression for the Doppler-cooling limit in Ref. [66] (p. 20).
50 Toptica DL Pro
51 Toptica iBeam smart

### 4.4.4 *Quadrupole laser (729 nm)*

A Titanium-Sapphire (Ti:Sa) laser with a short-term linewidth of 1 Hz [92] is used to coherently drive the states of the $S_{1/2} \leftrightarrow D_{5/2}$ quadrupole transition. The laser and the setup for its stabilisation are located at the *Qusim* experiment; detailed descriptions can be found in Refs. [69, 92]. About 40 mW of laser light is guided via optical fibre to our experiment table, where a TA amplifies the light to 0.5 W.[52] Another optical fibre decouples the amplified light from a setup of AOMs used for switching the light on and off and for changing and scanning its frequency. A schematic drawing of the 729 setup on our experiment table is shown in Fig. 4.13. The laser light is sent through a 270-MHz double-pass AOM[53] ($+1^{st}$ diffraction order, the actual RF driving signal is 226.5 MHz for addressing the $|S_{1/2}, m_j = -1/2\rangle \leftrightarrow |D_{5/2}, m_j = -3/2\rangle$ transition), allowing for frequency changes of tens of MHz for spectroscopy of the $S_{1/2} \leftrightarrow D_{5/2}$ transition. This AOM is driven by a phase-coherent RF source (Sec. 4.7) and can be used for setting the measurement basis in the ion-state tomography. Subsequently, the $+1^{st}$ diffraction order of either one of two AOMs[54] is coupled to an optical fibre. The AOMs are set up such that the $0^{th}$ diffraction order of the first AOM is coupled into the second AOM, and at any given time only one of them is active. In this way, the light reaches the ion via one of two optical fibres. The beam from one fibre (729-rad) propagates from front to back such that it overlaps only with the ion's radial modes of motion. The beam from the other fibre (729-ax) propagates from south-east to north-west such that it overlaps both with the ion's radial and axial modes of motion.

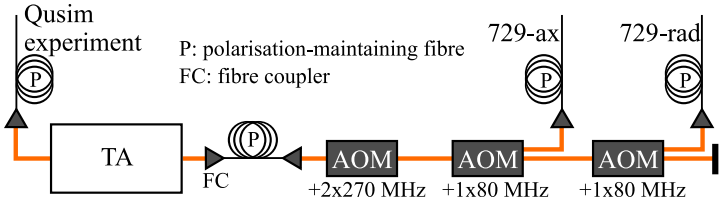


Fig. 4.13: **Conceptual schematic of the quadrupole-laser beam path.** Light at 729 nm from the quadrupole laser setup at the *Qusim* experiment is directed via optical fibre to our experiment table, where it is amplified by a TA. The $+1^{st}$ diffraction order of either one of two AOMs is coupled to an optical fibre.

52 No fibre-noise cancellation is performed on our side, so the laser linewidth is > 1 Hz once it reaches our table (no characterisation measurement has been performed to determine the linewidth at this point).

53 Brimrose 270-100

54 Gooch & Housego 3080-125

### 4.4.5 *Drive laser (393 nm) for the CMRT and transfer-lock laser (806 nm)*

The drive laser at 393 nm for the CMRT is a frequency-doubled Ti:Sa laser[55] whose frequency is locked to an external ultralow expansion (ULE) reference cavity in a vacuum chamber[56], as reported in the Master's thesis of H. Hainzer [89]. An ECDL at 806 nm is stabilised to the same reference cavity and, via a transfer lock scheme, the length of the cavity surrounding the ion—herein after referred to as ion-cavity—is in turn locked to this laser (Sec. 4.1.3). A schematic drawing of their setups is shown in Fig. 4.14.

SETUP: After passing an optical fibre, light at 393 nm is sent through the $-1^{st}$ diffraction order of a 150-MHz double-pass AOM[57] allowing for frequency changes of tens of MHz for spectroscopy of the CMRT and setting the frequency to the Raman resonance. An AOM[58] in single-pass configuration ($-1^{st}$ diffraction order) is used for further suppression of unwanted light when the AOMs are switched off. In order to generate the two phase-stable frequency components for the bichromatic CMRT (Sec. 3.3), this second AOM can be driven with two frequencies simultaneously, derived from phase-coherent direct digital synthesisers (DDSs). Both first-order shifted beams are coupled to the same optical fibre, sending the light to the north-back of the experiment.

As shown in Fig. 4.14, light from the transfer-lock laser at 806 nm is divided into two paths. One path is used for frequency-locking the laser to the ULE reference cavity. A double-pass AOM[59] in this path is used for tuning the locking point. The other path is directed to the ion-cavity, providing the transfer-lock laser field to which the ion-cavity is locked. A single-pass AOM[60] in this path was used for cavity ringdown measurements at the wavelength of the transfer-lock laser (Sec. 4.1.1).

The resonance frequency of the CMRT depends on the AC Stark shift induced by the drive laser, which is proportional to the intensity. Intensity fluctuations of the drive laser would therefore lead to a decreased efficiency of the CMRT. A homebuilt sample-and-hold circuit is used to actively stabilise the intensity of the drive-laser pulses between subsequent executions of the experimental sequence. The error signal for the stabilisation is derived from the signal of a photodiode in transmission of the vacuum chamber (outside the south-front viewport) and feedback is applied to the RF-amplifier driving the double-pass

55 MSquared Solstis-1600-PSX-R combined with an MSquared ECD-X external cavity resonant doubler accessory module; the Ti:Sa is optically pumped by a Lighthouse Photonics Sprout laser at 532 nm.
56 The ULE-cavity setup was bought from Stable Laser Systems.
57 Brimrose QZF 150-30
58 Brimrose QZF 80-20
59 Gooch & Housego 3200-124
60 Gooch & Housego 3080-125

AOM (Fig. 4.14). With the sample-and-hold in place, a drift of the laser intensity of 0.7(3)% was measured over a duration of 15 min, using the aforementioned photodiode.

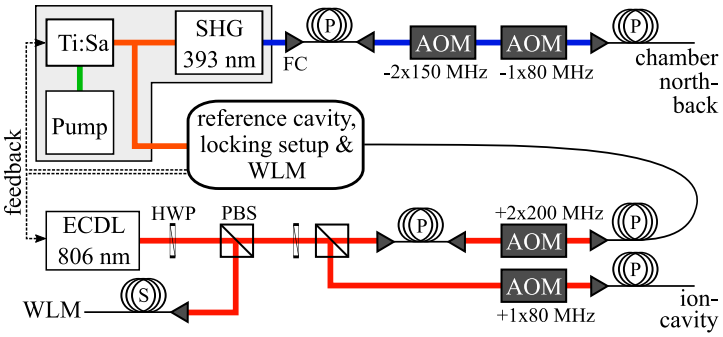


Fig. 4.14: **Conceptual schematic of the drive-laser and transfer-lock-laser beam paths.** The drive laser at 393 nm is a frequency-doubled Ti:Sa laser whose frequency is locked to a ULE reference cavity. An ECDL at 806 nm, used for locking the ion-cavity, is stabilised to the same reference cavity. Reference cavity and locking setup are described in Ref. [89].

FREQUENCY STABILISATION AND REFERENCE CAVITY: Both the drive laser and the ion-cavity need to be stabilised to within a fraction of the minimum linewidth of the CMRT, given by the natural linewidth $\kappa = 70(2)$ kHz of the ion-cavity at 854 nm. Moreover, drive laser and ion-cavity need to meet the Raman resonance condition, i.e., have the same detuning $\Delta$ from the excited state $|e\rangle$, and maintain that resonance over the timescale of the experiment. Achieving the required frequency stability of the drive laser and the transfer-lock laser was the goal of the Master's thesis of H. Hainzer [89]. The approach is to lock both lasers to a ULE reference cavity. In Ref. [89], in-lock linewidths of 87(1) Hz (FWHM) for the fundamental of the drive laser and 180(3) Hz for the transfer-lock laser were measured over a timescale of 12 s.

The purpose of a common frequency reference for both the drive laser and the transfer-lock laser is to reduce relative frequency drifts between the two arms of the CMRT, so that the Raman resonance condition can be maintained over long timescales. An absolute drift rate of 720 Hz/hr of the reference cavity was observed in Ref. [89], which translates to a relative drift rate of the same amount between the 806-nm laser and (frequency doubled) drive laser. The half width of the CMRT is on the order of 100 kHz. The drift of the reference cavity therefore causes the two arms of the CMRT (ion-cavity and drive laser) to move off Raman resonance by a half linewidth in a time of about 140 hours: significantly longer than the timescale of the experiments presented here.

The linewidth of the transfer-lock laser stated above was measured at a wavelength of 785 nm, the wavelength originally intended for locking the ion-cavity. However, during construction of the ion-cavity

(Sec. 4.1.2) the transmission profile of the ion-cavity mirrors shifted, rendering the natural linewidth of the ion-cavity at 785 nm too broad for locking it with the required stability. With the reflective coating of the reference cavity centred around 780–785 nm [89], a suitable wavelength had to be found where the linewidths of both ion-cavity and reference cavity are narrow enough. At 806 nm, the ion-cavity could be locked with RMS frequency excursions as low as 9(2) kHz (measured over a timescale of 0.5 s, see Sec. 4.1.3). Natural linewidths of 3.5(1) MHz and 0.63(5) MHz were measured for the reference cavity and ion-cavity, respectively, at 806 nm via spectroscopy of the cavities' transmission profiles.

## 4.5 PHOTON DETECTION PATH

Detected photons are the ones that, after being emitted by the ion into the cavity, first exit the cavity via the mirror with transmission $T_2$ (Sec. 4.1) into what we call the cavity output mode. The photons then pass some passive optical elements with probability $P_{el}$, are coupled into a few-meter-long SM optical fibre with an efficiency $P_{fc}$ and are finally detected with a single-photon detector that has an efficiency $P_{det}$. The detection-path efficiency is therefore $P_{path} = P_{el}P_{fc}P_{det}$, and the total detected photon probability is given by $P_{tot} = P_S P_{path}$. As a reminder, the photon collection probability $P_S$ is the probability for obtaining a photon in the cavity output mode, as introduced in Ch. 2.

This section contains the characterisation of $P_{path}$ for the experiments presented in Ch. 6, in which the limits to the photon-collection probability $P_S$ are experimentally investigated. Furthermore, the setup for analysing the photon's polarisation state is described, which is used in the ion-photon entanglement experiment presented in Sec. 6.4. For the experiment of Ch. 7 (distribution of ion-photon entanglement over 50 km of optical fibre), which was carried out prior to the experiments of Ch. 6, photon path, detectors and polarisation analysis were different and are described in the chapter itself.

A schematic drawing of the cavity output path is shown in Fig. 4.15. After exiting the cavity, photons pass the following optical elements: an in-vacuum collimating lens, a vacuum viewport, a zero-order HWP, a zero-order QWP, a mirror, a lens with focal length $f = -50$ mm and three optical filters[61]. Combined, these elements have a transmission of $P_{el} = 0.97(1)$, measured with laser light at 854 nm and a powermeter. The filters are necessary for blocking the laser light at 806 nm, used for locking the ion-cavity, and to reduce background counts due to ambient stray light.

*Cavity-photon polarisation analysis*

For the ion-photon entanglement experiment of Sec. 6.4, a PBS on a magnetic post is added into the photon path for measuring the photon's polarisation state, introducing another 1% of loss [i.e. $P_{el}$ is

61 2x Semrock FF01-834/LP-25, 1x Semrock FF01-850/10-25

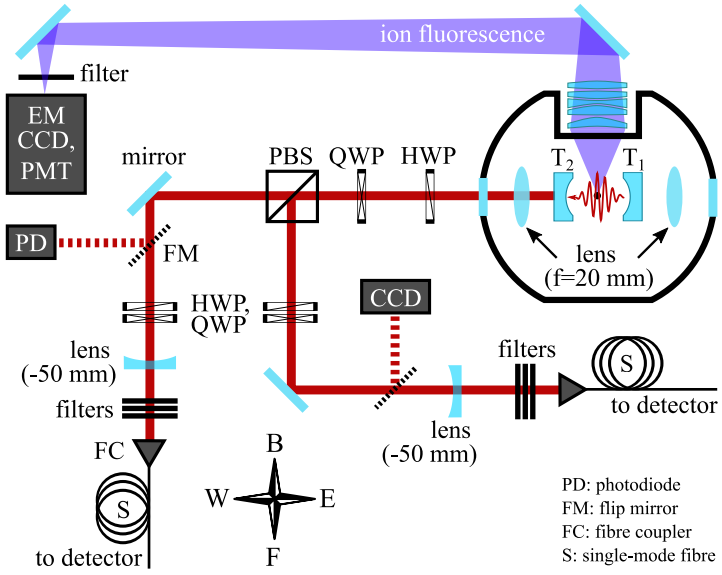


Fig. 4.15: **Cavity output path and setup for ion fluorescence detection.** Detected photons are the ones that leave the cavity through the mirror with transmission $T_2$ and follow the beam path indicated by the thick red line to the west side of the vacuum chamber. The photodiode can be used for detecting laser light coupled to the cavity [as needed for characterisation of the cavity (Sec. 4.1.1) or the beam path]; the charge-coupled device (CCD) can be used for determining the order of the TEM mode that is excited in the cavity. Ion fluorescence is collected by the objective in the back and focused at a distance of about 1.5 m onto the EM CCD camera and PMT, which are separated by a 50:50 BS (not shown).

reduced by 0.01 over its previous value to 0.96(1)]. The HWP and QWP are on motorised rotation mounts[62] for setting the measurement basis when performing quantum state tomography [36, 93]. The axes of the PBS and the optical axes of the waveplates were determined using laser light at 854 nm sent through the cavity. To ensure a high degree of linear polarisation in this calibration step, a Glan-Thompson polariser was temporarily inserted into the beam path between polarisation optics and vacuum chamber. A maximum extinction of $1 \times 10^{-3}$ was measured for laser light transmitted through the polarisation analysis setup and $1 \times 10^{-2}$ for the reflected port.

*Cavity-mode fibre coupling*

Photons are coupled to SM fibres[63] for which maximum fibre-coupling efficiencies of 0.82(3) and 0.81(3) were measured for the transmitted and reflected port, respectively. The fibre-coupling efficiencies were measured with laser light at 854 nm coupled through the cavity (thus matching the single-photon's path), measuring the power at the fibre inputs and outputs with photo diodes. The error bars are due to fluctuations of the light intensity transmitted through the cavity. When opening and closing the Mu-metal shield surrounding

62 Standa MPR16-1 with 8SMC5-USB
63 fibres: Thorlabs 780HP; fibre-couplers: Schäfter&Kirchhoff 60FC-4-M5-10

the vacuum chamber, optical elements and fibre in-coupling stage, slight additional drifts (likely caused by changes in temperature) lead us to estimate the fibre-coupling efficiencies $P_{fc}$ to be $0.81(3)$ for the transmitted port and $0.80(3)$ for the reflected port.

*Single-photon detectors*

Photons are detected with super-conducting nano-wire single-photon detectors (SNSPDs)[64], which are SM-fibre coupled. The detector efficiencies were determined[65] during installation of the system by the manufacturer using calibrated avalanche photodiodes (APDs)[66]. The detector in the transmitted port of the PBS has an efficiency $P_{det} = 0.87(2)$ and free-running dark counts of $0.3(1)$ per second at 854 nm. The detector in the reflected port of the PBS has an efficiency $P_{det} = 0.88(2)$ and free-running dark counts of $0.5(1)$ per second at 854 nm. The detector efficiencies are polarisation dependent and the above values correspond to optimal polarisation settings. The waveplates after the PBS in the photon paths set the optimal polarisation of photons generated via the CMRT. The calibrated efficiencies were cross-checked by us via comparison with an independently calibrated APD[67]. This APD, which is further used for the measurements described in Secs. 5.2.1 and 7.4, has an efficiency of $0.39(1)$ and free-running dark counts of $10(1)$ per second. For the measurements described in Sec. 7.4, a second APD is used with the same efficiency and dark counts of $11(1)$ per second.

*Measured detection-path efficiency ($P_{path}$)*

The overall detection-path efficiency evaluates for both paths to $P_{path} = 0.68(3)$. This value for $P_{path}$ is valid for all the experiments presented in Ch. 6 (performed with or without PBS), as the PBS does not change $P_{path}$ to within the measured precision.

CAVITY OUTPUT MODE: The cavity-output spatial mode was characterised in order to be able to match it to the modes of the SM fibres leading to the SNSPDs. The $TEM_{00}$ mode profile of 854-nm laser light sent through the cavity was measured with a beam profiler[68] at two points in the cavity output path. Specifically, the intensity distributions were measured along two orthogonal dimensions (x,y) and a Gaussian fit (Fig. 4.16) yielded the beam diameters ($1/e^2$) displayed in Table 4.4. Here, $D_1$ are the diameters closer to the cavity and $D_2$ are the diameters at a distance $d = 17(1)$ cm further down the beam path. Taking the average between the x and y directions, a divergence $\Theta = 2\arctan(\frac{D_2 - D_1}{2d}) = -0.0017(2)$ is calculated from the measured diameters.

The lenses with focal lengths $f = -50$ mm before the fibre couplers (Fig. 4.15) were added to the setup following simulations of the optical

64 Scontel
65 The calibration was performed with the fibres later used in the experiment already attached to the detectors (the other end of the fibres is then directly plugged to the fibre couplers, see Fig. 4.15).
66 Excelitas
67 Laser Components
68 Thorlabs BC106-VIS

beam path using the Zemax OpticsStudio software. Here, the fibre-coupling optimisation tool was used, with which the optimal position of the lenses (37 mm from the fibre inputs) could be determined, given a mode-field diameter of 5 µm of the fibres (at 850 nm). The thus installed lenses allowed for an increase in the fibre-coupling efficiencies from about 0.5(1) to the previously stated values.

| | x | y |
|---|---|---|
| $D_1$ (µm) | 1083(5) | 1047(6) |
| $D_2$ (µm) | 850(4) | 707(3) |

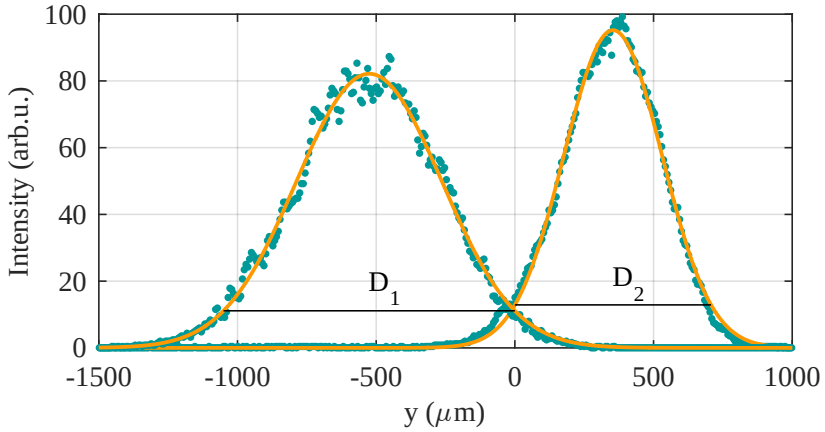


Table 4.4 & Fig. 4.16: **Characterisation of the cavity output mode.** The $1/e^2$-diameters $D_{1,2}$ of the cavity output mode were extracted from Gaussian least-square fits to intensity distributions measured along two dimension $x, y$. In the figure, the measured and fitted mode profiles along $y$ are shown (plotted with an arbitrary $y$-offset). The slight difference in the divergence of the $x$ and $y$ direction is likely caused by an astigmatism originating from cavity light approaching the in-vacuum lens at an angle and off-centre.

## 4.6 SETUP FOR FLUORESCENCE DETECTION AT 397 NM

For quantum state tomography of the ion-photon entangled state (Sec. 6.4 and Ch. 7), the electronic state of the ion is determined via detection of the ion fluorescence at 397 nm (Sec. 3.4), collected by a 5-lens objective[69] at the back side of the vacuum chamber. At the on-axis working distance of 58 mm between trap centre and the first lens surface, the numerical aperture (NA) is 0.289, which corresponds to a collection efficiency of 2.5% of the full $4\pi$ solid angle [69, 94]. The light is focused at a distance of about 1.5 m onto the EM CCD camera[70]

69 custom-made by Silloptics, Germany; for more information see [94] Sec. 3.6.
70 Andor iXon Ultra 897

and PMT (Fig. 4.15), each situated at one port of a 50:50 BS. A bandpass filter[71] before the BS blocks stray light from reaching the devices and the PMT is further protected by an adjustable slit aperture. For the experiments of this thesis, for a single ion, a maximum count rate of about $15 \times 10^3$ counts per second is measured by the PMT when saturating the $S_{1/2} \leftrightarrow P_{1/2}$ transition. While only the PMT signal is used for detecting the state of the ion, the EM CCD camera is used for monitoring the ion number during loading (verifying that only a single ion is in the trap) and for positioning the ion in the cavity waist (Sec. 5.1). Using the procedure described in Ref. [69], which relies on the known distances between ions in strings, and a camera pixel size of $16 \times 16\ \mu m^2$, a magnification of 18.7(1) is determined for our imaging setup. One pixel on the camera images thus corresponds to 0.86(2) µm.

## 4.7 EXPERIMENT CONTROL

Most of the experimental apparatus is controlled from a computer—the *Control PC*—on which the C++ program *TrICS* (trapped-ion control software, developed in-house) is used to compile the experimental sequences and interact with the control electronics. For details about *TrICS*, see the PhD thesis of D. Heinrich [90]. For the sake of a better overview of the experiment control, the following description is divided in three parts: laser pulse control, digital laser-control, and data acquisition and trap control. A graphical representation is provided in Fig. 4.17, with the terms used in that figure to be defined in the following paragraphs.

LASER PULSE CONTROL: All laser pulses are generated with AOMs; the pulse parameters (amplitude, length, phase) are controlled via the RF signals driving the AOMs. Except in special cases, the RF is supplied by a rack of DDSs, connected via a Bus cable to a PCI expansion card[72] in the *Control PC*. The timing and length of these RF pulses are controlled by TTL signals applied to RF switches[73] that connect the DDSs to RF amplifiers which are in turn connected to the AOMs. These TTL signals are generated by the *"Pulse Box"*, a field-programmable gate array (FPGA)-based pulse sequencer developed by Paul Pham and Philipp Schindler [95]. Via Ethernet and TTL channels, the *Pulse Box* is connected to the *Control PC* where the TTL signals are processed by another PCI expansion card[74].

For the generation and characterisation of ion-photon entanglement, the RF signals for the 393 single-pass AOM (generating the bichromatic

71 Semrock 390/18
72 National Instruments PCI 6533 (NI DIO-32 HS)
73 Mini-Circuits ZASWA-2-50DR+
74 Nation Instruments PCI 6733

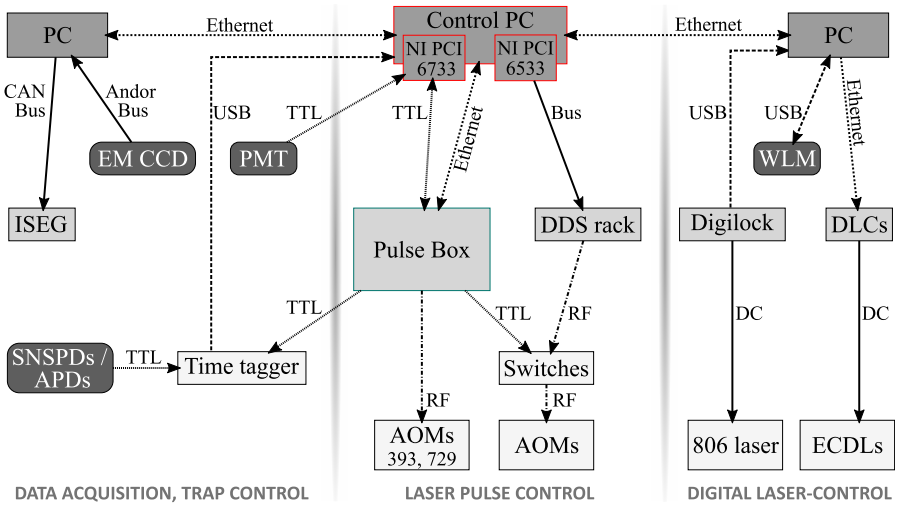


Fig. 4.17: **Experiment control and data acquisition.** Boxes represent the electronic devices, arrows the form and direction of communication. For a better overview, the schematic and description in the main text are divided in three parts. Acronyms are defined in the main text.

drive field) and the 729 double-pass AOM (setting the measurement basis for the ion state tomography) are supplied by two phase-stable DDSs in the *Pulse Box* which are referenced to a 10-MHz GPS signal. These DDSs provide the ability to set the relative phase of the RF pulses, as well as maintain and control a fixed phase relationship between the pulses.

DIGITAL LASER CONTROL: A second PC is used for communication with the WLM. This PC is connected to the *Control PC* via Ethernet, receiving the setpoint wavelengths for the ECDLs (see Sec. 4.4.2) from *TrICS*. The error signals calculated by the WLM control-software (installed on the second PC) are sent via Ethernet to the digital diode-laser controllers (DLCs) which adjust the ECDLs' piezo voltages. A digital locking module[75], connected to the second PC via USB, is used for stabilising the frequency of the 806 laser to the reference cavity (see Sec. 4.4.5 and Ref. [89]).

DATA ACQUISITION AND TRAP CONTROL: Experimental data includes the detection events of cavity photons registered by photon detectors and, in the case of ion-photon entanglement, the ion fluorescence signal detected by the PMT. Cavity photons are detected with SNSPDs (APDs in Ch. 7) whose TTL signals are sent to a time tagger[76] that is connected to the *Control PC*. At the beginning of the experimental sequence as well as for every drive-laser pulse, the time

75 Toptica Digilock110
76 Swabian Time Tagger 20

tagger also receives TTL triggers from the *Pulse Box*, allowing for a correlation between the experimental sequence and the detection events. The ion fluorescence, detected by the PMT, is acquired by one of the PCI expansion cards in the *Control PC*.

A computer-controlled high-voltage source[77], connected via Controller Area Network (CAN Bus) to a third PC on the local network, is used for supplying the DC voltages for the ion trap. The EM CCD camera communicates via its proprietary Andor Bus with the same PC.

77 ISEG box EHS 82 20x-F

# 5 KEY METHODS

This chapter gives an overview of key methods used for preparing the experiments presented in Chapters 6 and 7 and for analysing the measurement outcomes. Methods for measuring key experimental parameters are presented, essential for a meaningful comparison between experimental data and simulations. Finally, numerical simulations of our ion-cavity photon-generation process are summarised.

In Sec. 5.3, text from Ref. [38] has been reprinted with modifications.

## 5.1 POSITIONING THE ION IN THE CAVITY WAIST

Achieving the maximum photon-collection probability of our setup requires achieving the maximum ion-cavity coupling strength $g$ [Eq. (3.1)]. For this, the ion needs to be placed in the cavity waist, i.e., the centre of the cavity, and at an antinode of the cavity vacuum field. In the early stages of the experiment, including the experiment presented in Ch. 7, measurements of the photon collection probability $P_S$ suggested a significantly smaller $g$ than expected from the measured cavity geometry (see Sec. 4.1.1 for the cavity characterisation). Subsequently, using the method described in this section, the ion was discovered to be approximately one Rayleigh range (0.56 mm) away from the location of the cavity waist along the cavity axis, causing a reduction in $g$ by approximately $1/\sqrt{2}$ . Correcting for this offset was one of the prerequisites for achieving the efficiencies reported in Ch. 6.

The relative position of the cavity waist to the ion is determined by coupling light at 806 nm to a mode of the cavity and probing the intracavity field with an ion. The cavity is locked to the laser and the ion is translated along the trap axis through a cavity mode by changing the balancing of the endcap voltages. Due to a slight deviation from a 90° angle and the resulting overlap between trap axis and cavity axis (see Sec. 4.1.2 for the reason of this overlap), the ion passes several fringes of the intracavity standing wave on its trajectory, as illustrated in Fig. 5.1. The resulting position-dependent AC Stark shift, which is proportional to the intensity of the intracavity field, is measured on the $|4^2S_{J=1/2}, m_j = -1/2\rangle \leftrightarrow |4^2D_{J=5/2}, m_j = -5/2\rangle$ quadrupole transition with the laser at 729 nm. The position of the ion with respect to the centre of the cavity is then extracted from a comparison between calculated and measured fringe pattern of the standing wave, taking into account the Hermite-Gauss mode pattern of the cavity mode, as explained in the following.

The free-space electric-field spatial distribution of Hermite-Gauss $TEM_{mn}$ modes, in either the $x$ or $y$ transverse dimensions and with an axial distance $z$ from the waist with radius $w_0$, is given by [43]

$$E_n(y,z) = \sqrt{\frac{1}{2^n n!}}\frac{w_0}{w(z)} H_n\left(\frac{\sqrt{2}y}{w(z)}\right) \times \exp\left[-y^2\left(\frac{1}{w(z)^2} + i\frac{k}{2R(z)}\right) - ikz - i(n+1/2)\arctan\left(\frac{z}{z_R}\right)\right]. \tag{5.1}$$

Here, $R(z) = z[1 + (z_R/z)^2]$ is the ROC of the beam's wavefronts (the other parameters are defined in Sec. 2.1.1). Due to resonant enhancement of the input laser power $p_{in}$, the circulating power inside a cavity is given by $p_{circ} = p_{in}\ \beta 4T_1[\mathcal{F}/(2\pi)]^2$ [79]. The factor $\beta < 1$ accounts for the fraction of input light that is coupled to the mode excited in the cavity. The spatial distribution of the electric field inside the cavity can then be written as

$$E_{cav}(y,z) = \sqrt{\frac{2}{c\epsilon_0}\frac{p_{circ}}{\pi w_0^2}}[E_n(y,z) + E_n(y,-z)], \tag{5.2}$$

with $\epsilon_0$ the vacuum permittivity. The Rabi frequency of the $D_{5/2} \leftrightarrow P_{3/2}$ transition at 854 nm, with dipole moment $\mu_{D_{5/2}}$ [Eq. (2.13)], is given by $\Omega_{D_{5/2}} = \frac{\mu_{D_{5/2}} E_{cav}}{\hbar}$. The AC Stark shift of the 806-nm intracavity field on the $D_{5/2}$ level is estimated to be $\delta_{AC} = \frac{|\Omega_{D_{5/2}}|^2}{4\Delta}$, with $\Delta/2\pi = 39$ THz the frequency difference between the laser at 806 nm and the $D_{5/2} \leftrightarrow P_{3/2}$ (854-nm) transition (any effect on the $S_{1/2} \leftrightarrow D_{5/2}$ transition at 729 nm is negligible in comparison).

Fig. 5.2 shows measurements of $\delta_{AC}$ for an input power $p_{in} = 0.08$ mW as a single Doppler-cooled ion is placed at different positions along the trap axis and corresponding points in a cavity $TEM_{00}$ mode. Each ion position corresponds to a certain combination of voltages on the trap endcaps. The relative distances are measured with the EM CCD camera (calibrated via known distances between ions in strings; see Sec. 4.6). An arbitrary offset was added to the position data, approximately centring the plot around the cavity axis.

Let $y$ be the dimension perpendicular to the cavity axis ($z$) and at the angle $\alpha$ to the trap axis. A simulation of the intracavity field via Eq. (5.2), with the $(y,z)$ coordinates rotated by $\alpha$ around the $x$-axis, is shown as an orange line in Fig. 5.2. For the simulation, the parameters $z = z_d = 0.56(1)$ mm, $\alpha = 4.1(1)°$ and $\beta = 0.20(1)$ are used, which yield the best match with the measured data. These values were found by manually adjusting the model parameters, determining the given confidence intervals by eye. The parameter $z_d$ corresponds to the distance of the ion from the waist. The values used for $T_{1,2}$

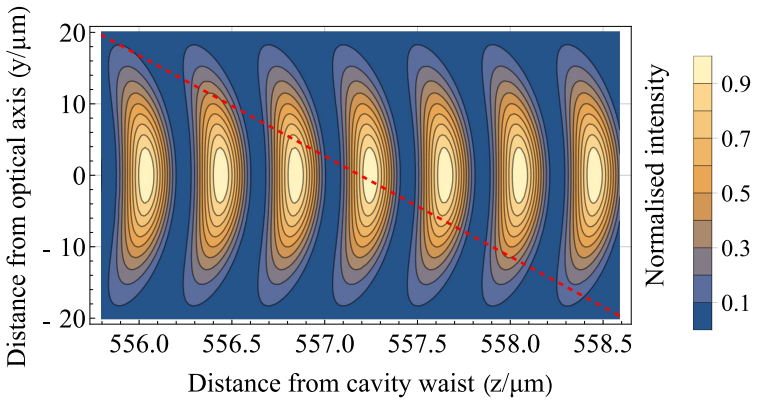


Fig. 5.1: **Simulated intracavity standing wave and orientation of the trap axis.** The intensity pattern of a cavity $TEM_{00}$ mode at 806 nm, calculated from Eq. (5.2) and normalised, is shown one Rayleigh range away from the cavity waist. The method presented in Sec. 5.1 consists in measuring the AC Stark shift suffered by a transition in a single ion at various points along the trap axis (red dashed line), to map out the cavity mode pattern along that dimension.

and L [contained within $p_{circ}$ in Eq. (5.2)] at 806 nm can be found in Table 4.1. The quantities $w(z)$ and $z_R$ are determined from a cavity waist of $w_0^{806} = 12.0(1)$ μm at 806 nm, calculated from the measured cavity length and mirror ROC (Sec. 4.1.1). The parameter $\beta$ can be independently estimated from the fraction of transmitted power to input power via the equaiton $p_t/p_{in} = \beta 4 T_1 T_2 [\mathcal{F}/(2\pi)]^2$ [79]. By measuring $p_t$ and $p_{in}$, a value of $p_t/p_{in} = 0.13(1)$ was determined, from which $\beta = 0.21(3)$ is obtained, in agreement with the value used in the simulation shown in Fig. 5.2. Remarkably, the effect of the wavefront curvature $R(z)$ (see Fig. 5.1) is visible in the data of Fig. 5.2: the period of the measured fringe pattern is compressed on one side of the optical axis and expanded on the other side. Including the corresponding term of Eq. (5.1) in the model was a crucial step in getting the simulations to match the measured data.

Correcting for the found displacement $z_d$ along the cavity axis (via the east↔west translation stage) indeed resulted in the cavity being centred on the ion and achieving the maximum expected $g$ in the experiment, as suggested by the comparison of experimental data to theory presented in Ch. 6. Furthermore, the position of the cavity seems not to have moved since, such that the steps outlined above had to be done only once.

## 5.2 SETTING UP THE CMRT

As detailed in Sec. 2.2.3, our photon-generation process corresponds to a cavity-mediated Raman transition (CMRT). Here, a two-photon Raman resonance is established between drive laser and cavity at a common detuning $\Delta$ from the excited state $|e\rangle$ (Fig. 3.1). Establishing

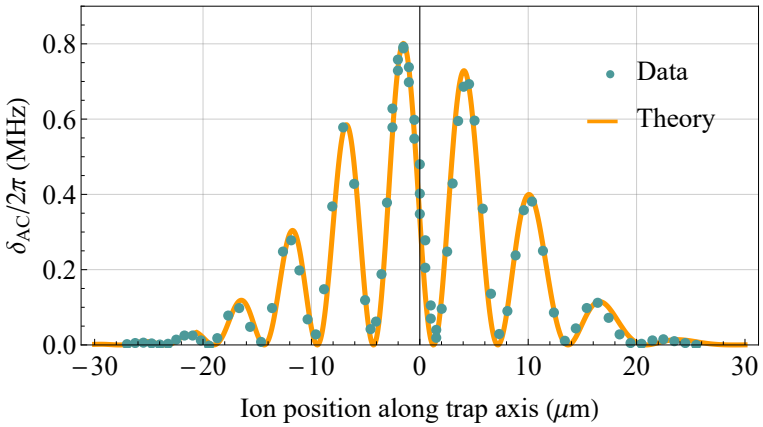


Fig. 5.2: **Mapping the intracavity field with an ion.** The AC Stark shift $\delta_{AC}$, induced by the intracavity 806 laser on the $S_{1/2} \leftrightarrow D_{5/2}$ transition, is measured for different ion positions along the trap axis and corresponding points in the cavity standing wave of a $TEM_{00}$ mode. By comparing the measured data to the model of Eq. (5.2), the position of the ion relative to the cavity waist could be determined, as well as the angle between the axes of cavity and trap. Error bars of the datapoints are smaller than the point size.

this resonance is achieved by first stabilising the frequency of the drive laser and the cavity length to the reference cavity (Sec. 4.4.5), after which the Raman resonance is found by probing the spectrum of the Raman transition, as outlined in this section and also described in Ref. [61]. The section further contains a description of the methods for determining $\Omega$ and $\Delta$, as well as the experimental procedure for setting up the bichromatic CMRT introduced in Sec. 3.3.

### 5.2.1 *Raman spectroscopy and identifying transitions*

Consider the experimental configuration shown in Fig. 3.1 and described in Ch. 3, i.e., a $\sigma^-$-polarised drive-laser beam propagating along the magnetic field axis and perpendicular to the cavity. In that configuration, three cavity-mediated Raman transitions can be driven from the initial state $|u,0\rangle$ to the $D_{5/2}$ manifold: first, to $|g_1,1\rangle$, where the photon emitted into the cavity has vertical (V) polarisation; second, to $|g_2,1\rangle$, where the photon emitted into the cavity has horizontal (H) polarisation; third, to $|m_j{=}{-}1/2,1\rangle$, where the photon emitted into the cavity is V polarised. After initialising the ion the the state $|u\rangle$ via optical pumping, cavity-mediated Raman spectroscopy is performed by scanning the frequency of the drive laser while keeping the detuning of the cavity from the excited state $|e\rangle$ fixed. The three transitions mentioned above can then be observed as peaks in the detected photon rate. Fig. 5.3 shows such a spectrum for a Doppler-cooled ion, as it is routinely obtained before an experiment by scanning the frequency of the 393 double-pass AOM and detecting photons in the cavity output. The peaks corresponding to the transitions $|u,0\rangle \rightarrow |g_1,1\rangle$ and

$|u,0\rangle \rightarrow |g_2,1\rangle$ are of similar height due to the similar strength of the respective CMRTs[1], as detailed in Sec. 3.3. With a Clebsch-Gordan coefficient of only $\sqrt{1/15}$ (see Fig. 3.2) and a polarisation projection $\zeta = \sqrt{0.5}$, the $|u\rangle \rightarrow |D_{5/2}, m_j{=}{-}1/2\rangle$ transition has the lowest probability. The three main transitions are separated by the Zeeman splitting of the $D_{5/2}$ manifold. In the absence of sideband cooling and due to the overlap between the drive-laser's propagation direction with the ion's motional modes, both blue and red motional sidebands of the ion are also clearly visible in the spectrum.

Polarisation analysis was done in the cavity output, sequentially, by rotating a HWP to determine if the single APD[2] measures H or V photons. The relatively low photon probabilities and high background level in Fig. 5.3 (compared to Ch. 6) are due to generally not optimised parameters and the use of the APD instead of two SNSPDs. About one quarter of the background in Fig. 5.3 is due to APD dark counts, the rest can be attributed to ambient light[3].

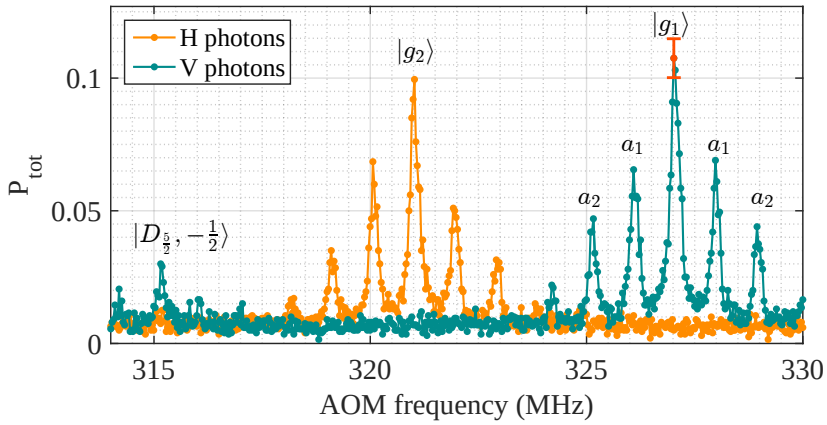


Fig. 5.3: **Cavity-mediated Raman spectroscopy.** The detected photon probability $P_{tot}$ is plotted as a function of the frequency shift imparted by the 393-nm double-pass AOM on the drive laser. With the ion initialised in $|u\rangle = |S_{1/2}, m_j{=}{-}1/2\rangle$ and a $\sigma^-$-polarised drive laser, three main transitions are visible, with final states in the $D_{5/2}$ manifold as indicated. First- and second-order axial sidebands ($a_1$ and $a_2$) are also visible, as indicated for one of the transitions. At the position of the small peaks next to second-order axial peaks, third-order axial and first-order radial sidebands overlap. Each data point represents the average of 2 000 photon-generation attempts. Error bars are omitted for clarity (except for an exemplary point in right peak, corresponding to one standard deviation based on Poissonian counting statistics). The connecting lines are a guide for the eye.

1 Resolving the slightly lower probability of the $|u\rangle \rightarrow |g_2\rangle$ transition and a comparison to theoretical calculations would require more statistics and a careful calibration of the drive-laser strength vs. AOM frequency, which is beyond the scope of this section.

2 Laser Components, see Sec. 4.5

3 For the experiments presented in Ch. 6 the detectors were better shielded from ambient light.

### 5.2.2 *Calibration of drive strength Ω and detuning Δ*

The frequency of the Raman resonance depends on the intensity of the drive laser due to the AC Stark shift induced by the drive laser on the $|u\rangle \leftrightarrow |e\rangle$ transition. A measurement of the AC Stark shift allows for calibrating the Rabi frequency of the drive laser Ω for a known Δ.

DETUNING Δ: The detuning $\Delta/2\pi = -403(1)$ MHz of the CMRT is determined by probing the $|u\rangle \leftrightarrow |e\rangle$ atomic resonance at 393 nm with the $\sigma^-$-polarised drive laser. More specifically, the frequency of the drive laser is scanned across the atomic resonance and the probability for pumping the ion to the $D_{5/2}$ manifold is measured via the electron shelving technique (see Sec. 3.4.1). The laser frequency is measured with the WLM with a resolution of 1 MHz. The laser intensity is set to well below saturation. The $|u\rangle \leftrightarrow |e\rangle$ atomic resonance frequency is then extracted from a fit to the measured excitation spectrum. The detuning Δ corresponds to the difference between the atomic resonance frequency and the frequency of the drive laser on Raman resonance (for vanishing AC Stark shift).

DRIVE STRENGTH Ω: In the case of a single-frequency drive laser, its Rabi frequency Ω is determined by measuring the AC Stark shift $\delta_{AC}$ imparted by the laser onto the state $|u\rangle$ and therefore onto the Raman resonance frequency:[4]

$$\Omega = \sqrt{4\delta_{AC}\Delta} \tag{5.3}$$

Specifically, two spectra of the CMRT are measured. One spectrum is measured at a drive-laser Rabi frequency Ω, from which the AC-Stark-shifted Raman resonance frequency $f_R$ is extracted. Another spectrum is measured using a drive-laser Rabi frequency for which the laser-induced AC Stark shift is smaller than the measurement resolution. From this second spectrum the un-shifted Raman resonance frequency $f_0$ is extracted, such that the AC Stark shift is determined as $\delta_{AC} = f_R - f_0$. With the known value for the detuning Δ, the Rabi frequency Ω is then determined via Eq. (5.3).

In the case of a bichromatic drive laser, with frequency components of strengths $\Omega_1$ and $\Omega_2$, the AC Stark shift due to the total Rabi frequency $\Omega = \sqrt{\Omega_1^2 + \Omega_2^2}$ is approximately given by $\delta_{AC} = \Omega_1^2/4\Delta_1 + \Omega_2^2/4\Delta_2$. In the context of this thesis the detunings are given by $\Delta_1 = \Delta$ and $\Delta_2 = \Delta - \delta_Z$, where $\delta_Z/2\pi = 7.1$ MHz is the Zeeman splitting of the $D_{5/2}$ manifold. At the time of performing the experiments of this thesis, a mechanism for measuring the individual drive strengths was

4 Eq. (5.3) is a first-order approximation based on the full expression for the AC Stark shift induced on an energy level of an atomic dipole transition: $\delta_{AC} = -\Delta/2 - \sqrt{\Omega^2 + \Delta^2}/2$. The approximation is valid for $\Delta \gg \Omega$, as in our case.

still missing. The total Rabi frequency is therefore estimated using the same formula as for the single-frequency case [Eq. (5.3)] (assuming the same detuning $\Delta$ for both drive components).[5]

### 5.2.3 *Setting up the bichromatic CMRT*

Preparing the experiment for the generation of ion-photon entanglement requires setting the ratio $\Omega_1/\Omega_2$ for which both Raman transitions are driven with equal probabilities, i.e., they are "balanced". In this case, the temporal wavepackets of the generated horizontally and the vertically polarised photons are identical and the maximally entangled state of Eq. (3.3) is generated [56].

The method for balancing the transitions consists in performing a scan of the drive-laser pulse length and plotting the photon detection probability in the H/V polarisation basis, as shown in Fig. 5.4. The measurement is performed without recording the time tags of photon detection events and is evaluated on the fly[6], taking around 3 min to complete. The powers of the two drive-laser fields are varied and the measurement repeated until the two probability curves overlap, estimating the quality of the overlap by eye. Note that the detection-paths for the two polarisations have equal efficiencies to within their calibration uncertainties (see Sec. 4.5), where the latter are on the order of the error bars shown in Fig. 5.4. Therefore, once the probability curves are balanced in the H/V basis, changing to the V/H measurement basis does not significantly change the observed balancing (in case of unequal detection-path efficiencies, the sum of the measured probabilities in the H/V and V/H bases would need to be balanced).

The balancing achieved in an actual experimental run, following this initial calibration step, is evaluated via post-processing of the experimental results, by comparing the temporal shapes of the generated H and V photons and their integrated probabilities (Sec. 6.4).

The frequency difference in the bichromatic drive field is set to the Zeeman splitting between the states $|g_1\rangle$ and $|g_2\rangle$. The frequencies of the $|u\rangle \leftrightarrow |g_{1,2}\rangle$ transitions are found via spectroscopy on the 729-nm transition. The centre frequencies of the corresponding excitation spectra are extracted from Gaussian fits to within an uncertainty of 0.1 kHz. This uncertainty is on the same order as the dominant source of frequency fluctuations in the 729-nm transition: the nearby elevator causes magnetic-field changes that correspond to frequency changes in the $|u\rangle \leftrightarrow |g_1\rangle$ transition of up to 0.3 kHz. These frequency changes

5 Using, for example, the Rabi frequencies given in Sec. 6.4, $\Omega_1/2\pi = 14.2$ MHz and $\Omega_2/2\pi = 16.8$ MHz, and $\Delta_2 = 2\pi(403 - 7.1)$ MHz, would result in $\delta_{AC}/2\pi = 0.303$ MHz. In comparison, assuming the same detuning $\Delta_1 = \Delta_2 = \Delta$ for both frequency components yields $\delta_{AC}/2\pi = 0.300$ MHz, translating to an error of less than 1% in the estimation of the total Rabi frequency.

6 At the time of performing the measurement, no routine for on-the-fly processing of time-tagged data had been implemented yet.

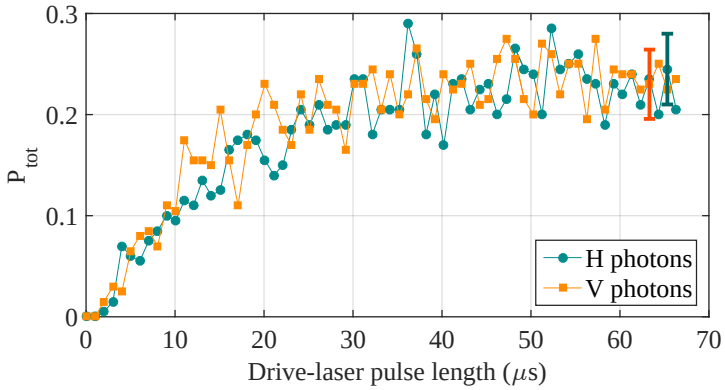


Fig. 5.4: **Balancing the bichromatic Raman transition.** The single-photon detection probability is presented as a function of the drive-laser pulse length. Example data is plotted, taken prior to the experiment presented in Sec. 6.4, used for on-the-fly assessing the balancing of the bichromatic Raman transition. Each data point represents the average of 200 photon-generation attempts. Error bars, shown for two measurement points at the right end of the plot, correspond to one standard deviation based on Poissonian counting statistics. The connecting lines are a guide for the eye.

translate to changes in the frequency splitting of the states $|g_1\rangle$ and $|g_2\rangle$ of around 0.1 kHz.

## 5.3 TOMOGRAPHY OF THE ION-PHOTON ENTANGLED STATE

To reconstruct the ion-photon state, which is of the form $|\Psi(\theta)\rangle = 1/\sqrt{2}\left(|g_1\rangle|V\rangle + e^{i\theta}|g_2\rangle|H\rangle\right)$ (see Sec. 2.2.3), a full state tomography of the two-qubit system is performed, as in Ref. [34]. The tomography consists in measuring correlations between the photon's polarisation and ion's electronic qubit state.

QUBIT MEASUREMENTS: On the photon polarisation-qubit side, the state is projected to one of six states (horizontal, vertical, diagonal, anti-diagonal, right circular and left circular). This is equivalent to performing projective measurements in three bases described by the Pauli spin-1/2 operators. For example, horizontal and vertical are the eigenstates of the Pauli $\sigma_z$ operator [96]. For the entanglement experiment presented in Sec. 6.4, the polarisation-analysis setup described in Sec. 4.5 is used. The setup includes two detectors, one at each output of the PBS. For the experiment presented in Ch. 7, the polarisation-analysis setup, described in Sec. 7.2, includes a single detector.

To perform an ion qubit measurement, the $|g_1\rangle$ electron population is first mapped to the $|u\rangle$ state via a 729-nm $\pi$-pulse[7]. That is, the D-manifold qubit, consisting of states $|g_1\rangle$ and $|g_2\rangle$, is mapped into an optical qubit with logical states $|u\rangle$ and $|g_2\rangle$. In order to measure

7 The $\pi$-pulse has a duration of 8.1 μs (10 μs) in the experiment of Ch. 6 (Ch. 7).

which of these states the electron is in, the standard electron shelving technique, described in Sec. 3.4.1, is used: in the case of the $|u\rangle$-state outcome, scattered 397-nm photons from the ion are collected with the objective and detected with the PMT (Sec. 4.6). A detection time of 2000 µs (1500 µs) is used in Sec. 6.4 (Ch. 7), which, at a signal-to-noise ratio of around 15,[8] is sufficient to distinguish bright (scattering) and dark (non-scattering) ions with an error of less than 1% (see Ref. [66] Appendix A2). An example histogram of these fluorescence counts is presented in Fig. 5.5. The aforementioned measurement process implements a projective measurement into the eigenstates of the $\sigma_z$ basis. For measurements in the $\sigma_x$ ($\sigma_y$) basis, the $\pi$-pulse is directly followed by an additional 729-nm $\pi/2$-pulse[9] on the $|u\rangle \leftrightarrow |g_2\rangle$ transition with a zero ($\pi/2$) phase relative to the preceding $\pi$-pulse, rotating the ion-qubit measurement basis.

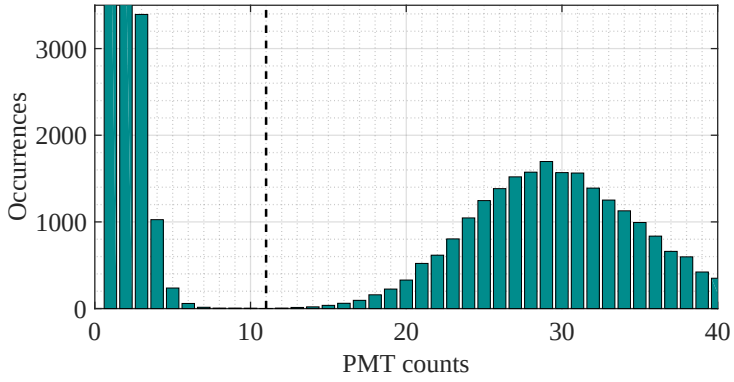


Fig. 5.5: **Histogram of PMT counts.** The histogram contains the counts of the complete state tomography of Sec. 6.4. Here, a detection time of 2000 µs is used and a detection threshold of 11 counts (vertical dashed line) to distinguish between bright and dark state. The y-axis is truncated at 3500. The occurrences in the first and second bin are 9600 and 8000, respectively.

STATE CHARACTERISATION: For each of the nine possible joint measurement bases (choice of photon basis and ion basis), the numbers of events corresponding to one of the four possible outcomes of these 2-qubit measurements are recorded (there is therefore a total of 36 possible outcomes). The number of events recorded for each outcome is then divided by the total number of events recorded for the given basis (divide each number by the sum of four) yielding estimates of the outcome probabilities. These probabilities are used to reconstruct the two-qubit density matrix by linear search with subsequent maximum likelihood method [97].

8 The scattering rate for an ion the the bright ($|u\rangle$) state is usually around 15 kHz and around 1 kHz for an ion in the dark ($|g_2\rangle$) state, where the latter is caused by ambient and laser light scattered into the PMT.

9 The $\pi/2$-pulse has a duration of 5.2 µs (5.0 µs) in the experiment of Ch. 6 (Ch. 7).

The state quality is quantified in terms of fidelity

$$F = \left[ \mathrm{Tr} \sqrt{\sqrt{\rho}\rho_{\mathrm{max.ent.}}\sqrt{\rho}} \right]^2 , \tag{5.4}$$

where $\rho$ is the reconstructed density matrix and $\rho_{\mathrm{max.ent.}}$ is the density matrix of the nearest maximally entangled pure state. This nearest state is found by exposing a perfect Bell state to single-qubit unitary rotations and searching for a state that provides the best fidelity with the experimentally obtained one.[10] The search involves the phase $\theta$, which is set by the relative phase between the two drive fields of the Raman process $\theta_{\mathrm{Raman}}$ and depends on the definition of the basis in the data analysis [36]. As the relation between $\theta$ and $\theta_{\mathrm{Raman}}$ has not been calibrated, the value of $\theta$ is not known in advance in the experiment. See Ref. [36] Ch. 8 for an experiment in which $\theta$ is tuned and calibrated.

For statistical analysis (determining error bars in quantities derived from the reconstructed density matrix), the Monte-Carlo approach [98] is used. We numerically generate M = 200 sets of 36 event numbers with Poissonian distribution and mean value equal to the experimental value for each of the 36 possible outcomes. Simulated outcome probabilities are derived from these simulated event numbers in the same way as is done for the experimental counts. In a final step, M density matrices are reconstructed via the maximum likelihood method for the simulated data and for each one the quantities of interest are calculated (fidelity, purity). The error bars given for the experimental results represent one standard deviation in the widths of the distributions of these quantities over M simulated data sets. The error bars are given centred around the experimental results (found via the maximum likelihood method explained above).

EFFECT OF BACKGROUND COUNTS: A background count is defined as a detector click that did not result from a cavity photon. The limit of the fidelity due to background counts is modelled in the following way. First, the number of background counts in the experiment is estimated by counting the detector clicks in a time window outside the drive-laser pulses (but within the same time-tag file that contains the photon-detection events used for the state tomography). The number of background counts is then added equally to the simulated measurement outcomes of an ideal Bell state (i.e., the background counts are treated as white noise). For the thus constructed outcomes, the density matrix of the closest maximally entangled state is then found in the same way as described above for the experimental data. Finally, the density matrix of this "noisy" state is used to calculate the fidelity with the ideal Bell state via Eq. (5.4).

10 Note that unitary rotations do not change the amount of entanglement in the system.

## 5.4 NUMERICAL SIMULATIONS

For a quantitative prediction of the photon-collection probability $P_S$ and to model the temporal dynamics of the system, for a given set of parameters of the CMRT, we numerically solve a model based on a master equation of the form of Eq. (2.15). The Hamiltonian comprises all 18 releveant electronic states in $^{40}Ca^+$ (see Fig. 3.2a, including all Zeeman sublevels) and two frequency-degenerate modes of the cavity (for H- and V-polarised photons). The Liouvillian includes cavity decay, the atomic decay channels of all dipole transitions, as well as dissipation due to the frequency jitter of the cavity lock (see Sec. 4.1.3). The latter introduces phase noise, which is included via a collapse operator onto the $D_{5/2}$ manifold at a rate of 0.01 MHz (see Sec. 4.1.3), effectively broadening the CMRT. The linewidth of the drive laser, at merely 87(1) Hz [89], is neglected in the simulations.

The simulation code is based on the *quantumoptics toolbox* in Matlab [99] and has been developed over many years by T. Northup and the cavity-QED team at the UIBK. A detailed description, including the specific Hamiltonian for $^{40}Ca^+$ as well as the interaction terms and the collapse operators, can be found in the PhD thesis of B. Brandstätter [56] (Ch. 3).

In the context of the experiments presented in Ch. 6, the system is driven by a $\sigma^-$-polarised laser field on the $S_{1/2} \leftrightarrow P_{3/2}$ transition. In the case of ion-photon entanglement, a second drive field is included in the simulations, in accordance with the bichromatic drive scheme outlined in Sec. 3.3. In both cases, the time evolution of the system's density matrix $\rho(t)$ is calculated via numerical integration of the master equation. From $\rho(t)$, the expectation values of an observable $\hat{o}$ can be calculated via the trace [56]

$$\langle \hat{o} \rangle = \mathrm{Tr}[\hat{o}\rho(t)]. \tag{5.5}$$

The expected temporal shapes (wavepackets) of generated H- and V-polarised photons are thus extracted from the expectation values of the photon number states in the cavity $\langle a_H^\dagger a_H \rangle$ and $\langle a_V^\dagger a_V \rangle$. A comparison of simulated and measured wavepackets is presented in Sec. 6.3 for V-polarised photons and Sec. 6.4 for photons polarisation-entangled with the ion. The presented simulated collection probabilities $P_S$ are calculated by integrating the simulated photon wavepackets.

# Part III

# EXPERIMENTAL RESULTS, SUMMARY AND OUTLOOK

# 6

# SATURATING THE UPPER BOUND ON THE PHOTON EFFICIENCY

Having established the theoretical framework (Chapters 2 and 3), as well as introduced and characterised the experimental setup (Ch. 4), we are now in a position to make predictions of, and experimentally investigate, the efficiency limits to photon collection of the apparatus. In this chapter, first, the upper bound on the photon-collection probability is evaluated for our cavity and atomic parameters (Sec. 6.1). Then, after introducing the laser-pulse sequence for the experiments of this chapter (Sec. 6.2), experimental results are presented on the generation of single photons not entangled with the ion (Sec. 6.3) and single photons entangled with the ion (Sec. 6.4). Furthermore, we investigate the ability of a trapped ion to serve as a multiphoton source by generating and detecting multiple sequential photons (Sec. 6.5). In the rest of this chapter, the effect of different parameter regimes on the photon-collection probability are studied in theory: different values of the output mirror transmission $T_2$ (Sec. 6.6), higher ion-cavity coupling strengths in principle attainable in our current setup (Sec. 6.7), and, lastly, combinations of parameter improvements in future systems (Sec. 6.8).

This chapter contains the results published in Ref. [38].

## 6.1 EFFICIENCY LIMITS IN OUR SYSTEM

For our cavity properties presented in Table 4.1 [$\lambda = 854$ nm, $w_0 = 12.31(8)$ µm, $\alpha_{\text{loss}} = 26(4)$ ppm and $T_2 = 90(4)$ ppm] and the atomic parameters introduced in Sec. 3.2 [$(\gamma_g, \gamma_u, \gamma_o)/2\pi = (0.55, 10.7, 0.46)$ MHz], Eq. (2.31) yields $P_S^{\text{bound}} = 0.75(3)$, the highest possible collection efficiency for a single $^{40}Ca^+$ ion in the setup. The corresponding maximum possible probabilities for photon emission into the cavity and photon escape from the cavity are $P_{\text{in}} = 0.970(2)$ and $P_{\text{esc}} = T_2/(T_2 + \alpha_{\text{loss}}) = 0.78(3)$, respectively [see Sec. 2.2.2 for how $P_{\text{in}}$ relates to Eq. (2.31)].

In order to achieve this upper bound, a polarisation projection of $\zeta = 1$ is required, or correspondingly $g/2\pi = 1.25(1)$ MHz [Eq. (3.1)] and $C = 0.98$, achievable only with an experimental configuration in which the propagation direction of the drive laser and the magnetic field axis are parallel to the cavity axis. However, as explained in Sec. 3.2, the experimental configuration in this thesis is such that the cavity axis is perpendicular to the drive laser and magnetic field, resulting in $\zeta = \sqrt{0.5}$, $g/2\pi = 0.88(1)$ MHz and $C = 0.49(1)$. Accordingly,

*Highest possible collection probability of our system ($P_S^{exp.max}$)*

the maximum probability for emission into the cavity is reduced to $P_{in} = 0.940(2)$ and Eq. (2.31) yields $P_S^{exp.max} = 0.728(30)$: the upper bound on the collection probability for pure polarised photons in the experiments reported in this thesis. As a reminder, this upper bound is valid for a CMRT in which the cavity couples the $|g\rangle \leftrightarrow |e\rangle$ transition, which has the highest Clebsch-Gordan coefficient of all the transitions $|D_{5/2}\rangle \leftrightarrow |P_{3/2}\rangle$. Photons generated via this CMRT are vertically (V) polarised.

For the generation of ion-photon entanglement, additionally to the CMRT with final atomic state $|g\rangle = |g_1\rangle$, a second CMRT is driven with corresponding final state $|g_2\rangle$, as explained in Sec. 3.3. As a reminder, photons generated via this second CMRT have horizontal (H) polarisation. For that transition, the maximum photon-collection probability is $P_S^H = 0.717(30)$. This upper bound is slightly lower than $P_S^{exp.max}$ due to the lower ion-cavity coupling strength $g$ on the $|g_2\rangle \leftrightarrow |e\rangle$ transition compared to the $|g_1\rangle \leftrightarrow |e\rangle$ transition (see Sec. 3.3).

To summarise, the maximum probabilities for collecting photons via each Raman process, when generated separately in our system, calculated using Eq. (2.31), are $P_S^{exp.max} = P_S^V = 0.728(30)$ and $P_S^H = 0.717(30)$, for the V and H photon, respectively. While we do not have an analytic expression for the maximum probability for obtaining a maximally entangled ion-photon state, numerical simulations suggest that the value tends to the mean of $P_S^V$ and $P_S^H$, given by $(P_S^V + P_S^H)/2 = 0.72(3)$, as the total Rabi frequency tends to zero.

## 6.2 LASER PULSE SEQUENCE

The laser pulse sequences for the experiments presented in this chapter are summarised in Fig. 6.1. First, a 50-µs "initialisation" laser pulse at 393 nm is applied, measured by a photodiode in transmission of the ion-trap chamber, which allows for intensity stabilisation of the subsequent 393-nm drive-laser pulse via a sample-and-hold system (Sec. 4.4.5). The initialisation pulse is followed by 1000 µs of Doppler cooling. Next, sideband-resolved laser cooling at 729 nm is performed on the ion's axial mode ($\omega_z/2\pi = 0.92$ MHz) and two radial modes ($\omega_{r1}/2\pi = 2.40$ MHz and $\omega_{r2}/2\pi = 2.44$ MHz), yielding mean phonon numbers of $\bar{n} = 0.5(2)$ in each motional mode. After preparing the ion in the initial state $|u\rangle = |S_{1/2}, m_j = -1/2\rangle$ via optical pumping, a drive-laser pulse is applied, which ideally triggers the emission of a photon by the ion into the cavity.

For the photon-train experiment presented in Sec. 6.5, the drive laser pulse, preceded by optical pumping, is repeated 15 times, generating a train of photons. For all other experiments, the drive-laser pulse is applied only once.

For the ion-photon entanglement experiment of Sec. 6.4, an additional step of detection of the ion qubit (and photon polarisation state) is carried out for characterisation of the ion-photon entangled state. Measurement of the ion-qubit state is performed by mapping the Zeeman qubit, encoded in superstitions of $|g_1\rangle$ and $|g_2\rangle$, to the $^{40}Ca^+$ optical quadrupole qubit via laser pulses at 729 nm, followed by fluorescence state detection, as detailed in Sec. 5.3.

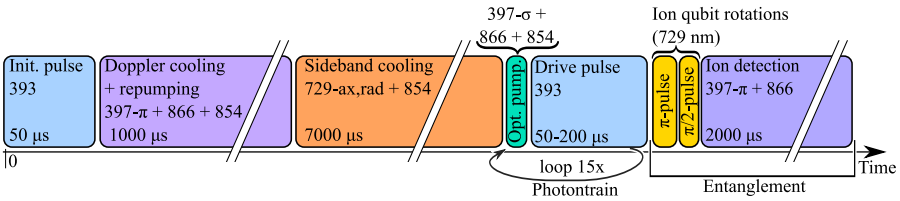


Fig. 6.1: **Laser-pulse sequence for the experiments of Ch. 6.** An initialisation laser pulse for intensity stabilisation of the drive laser is followed by Doppler cooling. Next, the ion is cooled close to the ground state of each of its three motional modes and prepared in the initial state $|u\rangle$ via optical pumping (10 µs of $\sigma^-$-polarised 397-nm light combined with 866 nm; 854 nm for repumping from the $D_{J=5/2}$ manifold). For the multiphoton experiment presented in Sec. 6.5, the drive-laser pulse, preceded by optical pumping, is repeated 15 times ("photontrain"). In the case of ion-photon entanglement (Sec. 6.4), the single drive-laser pulse is bichromatic and ion-qubit rotations as well as ion state detection are performed. The length of the $\pi$-pulse on the $|u\rangle \leftrightarrow |g_1\rangle$ transition is 8.1 µs, the length of the $\pi/2$-pulse on the $|u\rangle \leftrightarrow |g_2\rangle$ transition is 5.2 µs. See Table 4.3 for designations of the laser fields, Fig. 3.2 for corresponding atomic transitions and Sec. 5.3 for details on the lasers pulses for reconstructing the ion-photon entangled state. This figure has been modified from Fig. 9 of Ref. [38].

## 6.3 SINGLE-PHOTON RESULTS

In the first experiment, time-tagged photon detection events are recorded for three drive-laser Rabi frequencies $\Omega/2\pi$ = [14(1), 24(1), 46(1)] MHz. The temporal profiles of the detected single photons are shown in Fig. 6.2. These single-photon wavepackets are presented as a probability density $p_d(t) = N_d/(k \cdot \delta_t)$, where $N_d$ is the number of detection events registered in a time bin $\delta_t$ and $k$ is the number of attempts to generate a photon. The total detected probability $P_{tot} = P_S P_{path}$ is calculated by integrating the wavepacket and plotted in the inset of Fig. 6.2.

As can be seen from Fig. 6.2, excellent agreement is found between the experimental data and numerical simulations (see Sec. 5.4), supporting the validity of both the calibration procedures and the characterisation of the experimental setup. All parameters in the simulations are independently measured or estimated via calibration

experiments: see Sec. 4.1 for measurements of the cavity parameters and Sec. 5.2 for the calibration of the drive-laser strength $\Omega$ and detuning $\Delta$. There are therefore no free parameters within calibration uncertainties. Specifically, the following parameters produce the simulated curves of Fig. 6.2: $g_0/2\pi = 1.53$ MHz, $\Delta/2\pi = -403$ MHz, cavity lock jitter $\delta\nu_{\text{lock}}/2\pi = 0.01$ MHz, $\Omega/2\pi = (14.8, 24, 46)$ MHz. In order to match the experimental data, the simulated curves are multiplied by adjusted path efficiencies $\widetilde{P}_{\text{path}} = (1, 0.99, 0.97) \times P_{\text{path}}$ (see Sec. 4.5 for the calibration of $P_{\text{path}}$). The simulations include a time-dependent drive-laser pulse of symmetric trapezoidal shape, with 6 µs rise and fall times to account for the pulse shape generated in the experiment.

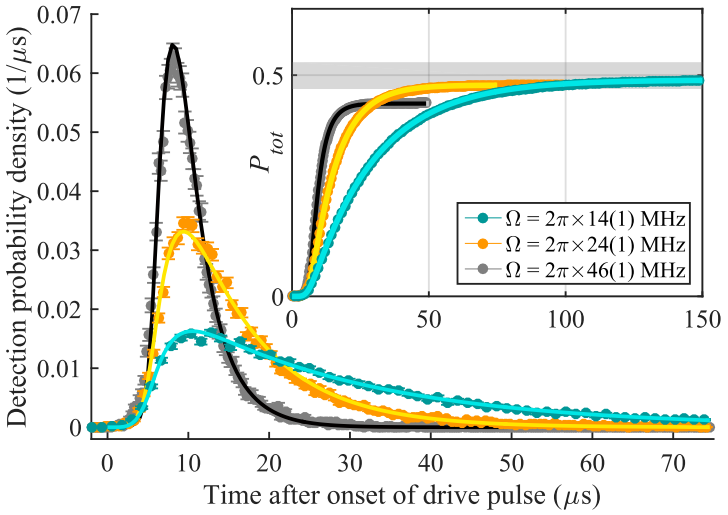


Fig. 6.2: **Single-photon wavepackets and efficiency.** Histograms of photon arrival times for different Rabi frequencies of the drive laser, normalised by the number of attempts $k = 50\,000$ and by the time-bin widths $\delta_t = (1.2, 0.6, 0.3)$ µs. **Inset**: Integrated wavepackets, yielding efficiencies $P_{\text{tot}} = [0.490(3), 0.478(3), 0.437(3)]$, averaged over a measurement time of 8 min. All plots: dots are experimental data, lines correspond to numerical simulations. Error bars correspond to one standard deviation based on Poissonian photon-counting statistics. Grey shaded area: $P_S^{\text{exp.max}} \times P_{\text{path}}$, i.e., maximum achievable total efficiency from the analytic model [calculated via Eq. (2.31)] given our detection-path efficiency. This figure has been reproduced from Fig. 3 of Ref. [38].

For $\Omega/2\pi = 14$ MHz, the lowest drive strength, the highest detected probability is obtained: $P_{\text{tot}} = 0.490(3)$. Here, out of the 50 000 photon-generation attempts, 24 358 cases led to exactly one photon being detected in the time interval of the drive laser pulse. In 28 cases a second photon was detected, consistent with the background light level of 5 per second, measured in a time-window outside the drive-laser pulses. After factoring out the independently measured path efficiency $P_{\text{path}} = 0.68(3)$, this detected single-photon probability corresponds to a collection probability of $P_S^{\text{exp}} = 0.72(3)$ out of the cavity. The value of $P_S^{\text{exp}}$ is consistent with the prediction of the numerical model $P_S^{\text{num}} =$

*Highest measured collection probability ($P_S^{exp}$)*

0.72(3) and with the maximum analytical value $P_S^{exp.max} = 0.73(3)$, where the errors in both predicted values are due to the uncertainties in the measured values of $T_2$ and $\alpha_{loss}$. We thus conclude that, to within the calibration uncertainty of the detection path, we reach the maximum collection probability in our system given only by atomic quantities and the cavity parameters of transmission, loss, waist and direction.

Significant improvements in $P_S$ would have to involve changing the cavity properties and could not be achieved by, e.g., further reducing the spatial localisation of the ion, modifying the temporal or spectral properties of the drive laser or choosing a different drive scheme. Numerical simulations show that improving the cavity length stability could at most increase $P_S$ by 0.01. Further discussion on ways to improve the efficiency by changing the setup is postponed until Sec. 6.7.

Numerical simulations show that decreasing $\Omega/2\pi$ from our lowest chosen value (14 MHz) by a factor of $1/3$ would increase the achievable collection probability by at most 0.3%. As this increase is below the statistical resolution of our presented measurements, no systematic studies have been performed in that regime. In general, the collection probability saturates as $\Omega$ tends to 0, as detailed in Sec. 2.2.3, and any slight improvements come at the cost of increasingly high stability requirements for the laser frequency and cavity lock. As $\Omega$ is increased, the photon-collection probability $P_S$ is reduced because of the increased probability for spontaneous scattering: the effective spontaneous decay rate $\gamma_{eff}$ increases faster with $\Omega$ than the coherent coupling rate $\Omega_{eff}$, leading to a higher probability of the state ending up, via spontaneous decay, in $|g,0\rangle$ or $|o,0\rangle$. While increasing $\Omega$ decreases $P_S$, a stronger drive produces photons that are temporally shorter, which could be advantageous for experiments demanding higher photon rates. Schemes to shape and chirp the drive-laser pulse [100, 101] could be used to minimise the reduction in $P_S$ that occurs for faster driving (larger $\Omega$).

Fig. 6.3 shows numerical predictions of $P_S$ for our experiment for a range of drive strengths $\Omega$. As described above, the collection probabilities saturate for decreasing values of $\Omega$ and drop off as $\Omega$ is increased. The simulations were performed for three different sizes of the cavity lock jitter $\delta\nu_{lock}/2\pi = (0, 0.01, 0.1)$ MHz. The cavity jitter reduces the maximum achievable efficiency. For increasing values of $\Omega$ the effect of the cavity jitter on $P_S$ becomes less and less pronounced. Here, the short evolution time of the photon generation process (short photon wavepackets) imposes less stringent requirements on the frequency stability of the CMRT. Also plotted are the measured values for $P_S$, which correspond to the total detected probabilities $P_{tot}$ in Fig. 6.2 divided by the measured path efficiency $P_{path} = 0.68(3)$ (Sec. 4.5).

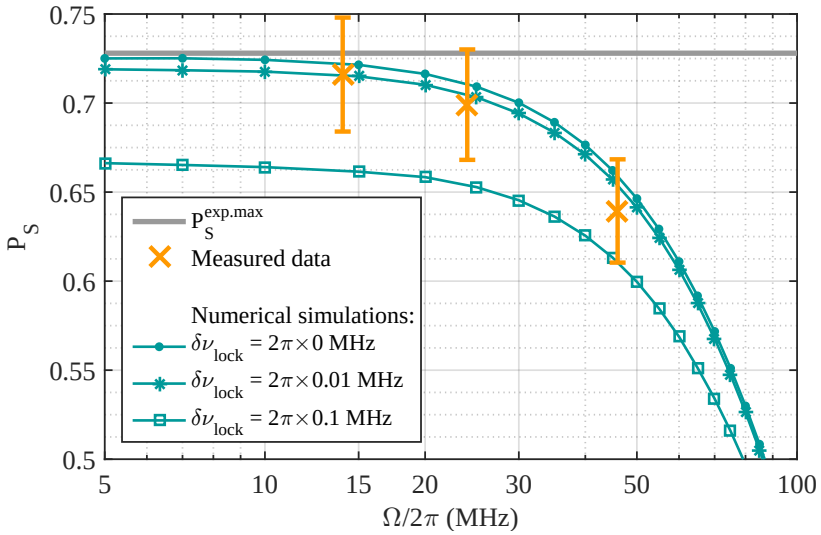


Fig. 6.3: **Photon-collection probability $P_S$ for different drive strengths $\Omega$.** The measured data points correspond to the total detected probabilities $P_{tot}$ in Fig. 6.2, divided by the measured path efficiency $P_{path} = 0.68(3)$. The numerical simulations were performed for three different values of the cavity lock jitter $\delta\nu_{lock}$ and otherwise same experiment parameters as used in Fig. 6.2 (including the time-dependent shape of the drive-laser pulse). The horizontal grey line indicates the upper bound $P_S^{exp.max}$, as calculated in Sec. 6.1 from Eq. (2.31).

## 6.4 ION-PHOTON ENTANGLEMENT

Entanglement between the photon and ion is generated via the bichromatic CMRT described in Sec. 3.3, resulting in entanglement between photon polarisation and ion qubit state of the form $|\Psi(\theta)\rangle = \frac{1}{\sqrt{2}}(|g_1\rangle|V\rangle + e^{i\theta}|g_2\rangle|H\rangle)$. An upper bound of 0.72(3) for the probability of collecting photons in the bichromatic Raman process was suggested in Sec. 6.1.

The bichromatic CMRT is set up according to the method detailed in Sec. 5.2: the individual Rabi frequencies $\Omega_1$ and $\Omega_2$ are set by varying the powers of the two drive-laser fields until the probability for detecting photons is balanced in the H/V polarisation basis, to within statistical uncertainty. A total Rabi frequency $\Omega = \sqrt{\Omega_1^2 + \Omega_2^2} = 2\pi \times 22(1)$ MHz is determined by measuring the AC Stark shift induced on the 729-nm transition by the combined CMRT fields.

For quantum state tomography, 45 000 attempts were made to generate an ion-photon entangled state over a ten-minute experimental run. In 20 788 cases at least one photon-detection event occurred during the drive-laser pulse. In the four cases where more than one detection event occurred during a drive-laser pulse, the event that occurred first was taken as the result. The measured detection probability of the

ion-photon entangled state is therefore $P_{tot} = 0.462(3)$, which, given the detection-path efficiency, corresponds to a collection probability of $P_S = 0.69(3)$ at the cavity output. This measured value of $P_S$ is consistent with the value 0.70(3) predicted by master-equation simulations for a bichromatic drive field with Rabi frequencies $\Omega_1/2\pi = 14.2$ MHz and $\Omega_2/2\pi = 16.8$ MHz. These values for $\Omega_{1,2}$ are consistent with the measured value of $\Omega$ above and predict photon wavepackets that closely match the ones observed in the experiment. Fig. 6.4b presents photon wavepackets for the cases where H and V photons were detected (ignoring the detected state of the ion qubit), yielding total integrated probabilities of $P_H = 0.239(4)$ and $P_V = 0.224(4)$, respectively. The imbalance of these probabilities is beyond the statistical resolution of the calibration step outlined in Sec. 5.2.

The tomographically reconstructed density matrix of the ion-photon state $\rho$ (Fig. 6.4c) has a fidelity of $F = \mathrm{Tr}(|\Psi\rangle\langle\Psi|\rho) = 0.966(5)$ with the maximally entangled state $|\Psi(\theta = 0.91)\rangle$ and a purity $\mathcal{P} = \mathrm{Tr}(\rho^2) = 0.948(9)$. The statistical uncertainties here are obtained via the Monte-Carlo method [98] based on photon-counting statistics, as detailed in Sec. 5.3. The measured state fidelity is not significantly limited by the imbalanced polarisation components nor by background photon counts. Specifically, the (unitary) simulations of Fig. 6.4b predict a fidelity with respect to a maximally entangled state of 0.9992, while background counts at the measured rate of 20 counts per second further limit the maximum achievable fidelity to 0.9974(7). See Sec. 5.3 for how the fidelity with the nearest maximally entangled state is found and how background counts are measured and modelled.

It is straightforward to show that the maximum fidelity of an arbitrary state $\rho_{arb}$ with any pure state is given by the square root of the purity of $\rho_{arb}$, that is, $F \leqslant \sqrt{P}$. Our experimental state saturates the aforementioned bound up to a difference $\sqrt{P} - F = 0.008(7)$, and therefore our total state infidelity $[1 - F = 0.034(5)]$ is almost entirely due to the lack of purity. Possible causes of the lack of purity in the experimental state are the cumulative effects of imperfections in the 729-nm laser pulses used in the ion-qubit state analysis as well as imperfections in the polarisation analysis of the photon. A detailed error budget at the percent level is beyond the scope of this work, requiring, e.g., improved measurement statistics for verification.

## 6.5 MULTIPHOTON STATES

A promising application of a near-deterministic interface between photons and quantum emitters is to generate the entangled multiphoton states that enable scalable quantum computing [102–104], as recently demonstrated for up to five sequential photons from a quantum dot [104], or long-distance quantum networking [28, 105, 106]. While the trapped-ion platform has great potential to enable the aforementioned

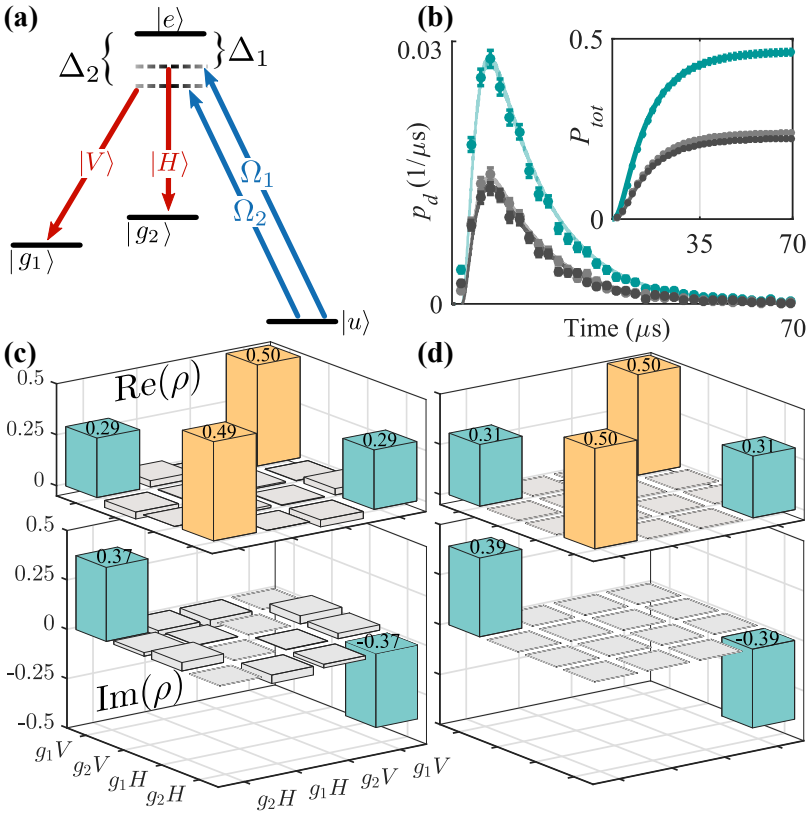


Fig. 6.4: **Generation and characterisation of the ion–photon entangled state. (a)** Atomic level scheme showing the bichromatic CMRT that generates the ion-photon entangled state $|\Psi(\theta)\rangle = \frac{1}{\sqrt{2}}(|g_1\rangle|V\rangle + e^{i\theta}|g_2\rangle|H\rangle)$. The frequency difference of the detunings $\Delta_1$ and $\Delta_2$ is equal to the Zeeman splitting between $|g_1\rangle = |D_{J=5/2}, m_j = -5/2\rangle$ and $|g_2\rangle = |D_{J=5/2}, m_j = -3/2\rangle$. **(b)** Wavepackets in the H/V (grey/black) polarisation basis and their sum (teal). The photon counts of all three ion-basis measurements were added up. Dots with error bars: measured data; lines: numerical simulations. Error bars represent one standard deviation, based on Poissonian photon statistics. **Inset:** integrated probabilities, yielding 0.224(4) for H and 0.239(4) for V. **(c) Data:** Real (top) and imaginary (bottom) part of the tomographically reconstructed density matrix ρ. **(d) Theory:** Real (top) and imaginary (bottom) part of the density matrix of $|\Psi(\theta = 0.91)\rangle$. This figure has been reproduced from Fig. 4 of Ref. [38].

applications, the generation and detection of photon trains has so far been limited by low single-photon detection efficiencies, in comparison to those achieved in the present work.

We report now on an experiment in which each experimental sequence consists of one instance of sideband cooling followed by 15 attempts to generate a vertically polarised photon, without further cooling. The experimental sequence, which was already described in Sec. 6.2, is sketched in Fig. 6.1. The 15 attempts (15 Raman laser pulses, each lasting 200 μs) are spaced by only 60 μs, during which time only electronic state re-initialisation, via repumping and optical

pumping, is performed. By limiting the sideband cooling time in this way, the total laser-pulse sequence for attempting to generate a train of 15 photons is reduced by an order of magnitude (from 125 ms to 12.5 ms) compared to the case of generating a single photon (Sec. 6.3).

A total of 30 000 attempts are made to generate trains of 15 photons over a 12-min experiment. During approximately 50% of the experiment duration, no photon-generation attempts are made due to the reprogramming time of the Pulse Box (Sec. 4.7). The 15 detected single-photon wavepackets are presented in Fig. 6.5a and reveal no statistically significant differences across the train, as shown in Fig. 6.5b. When averaged over all 15 wavepackets, the detected single-photon probability is $P_{tot} = 0.471(4)$. The measured probabilities for detecting $n$ sequential photons, beginning with the one in the first time window in the train, are presented in Fig. 6.5c and are fit with an exponentially decaying sequential photon probability of $[0.474(2)]^n$. Over the experiment we observe 90 instances of single photons in each of the first eight windows, 20 instances of single photons in the first ten windows, and one instance of all 15 time windows being full. Significant further improvements in the multiphoton detection rates in our system should be possible by increasing the attempt rate, e.g., by using periodic fast ground-state cooling techniques (requiring a few tens of microseconds) [107, 108].

Ultimately, the limit to the rate at which single photons can be collected from our system is set by the decay rate $\kappa/2\pi = 70$ kHz of our 2-cm-long cavity. Recall that, for a given quantum emitter, the cavity waist and unwanted photon loss $\alpha_{loss}$ determine the required optimum output-mirror transmission $T_2^{opt}$ for maximal photon-collection probability. After that optimisation, the cavity length $l$ remains a free parameter. Since $\kappa$ is proportional to $1/l$, the shorter the cavity, the higher the value of $\kappa$, and therefore the higher the potential rate of single-photon production. Integrating trapped ions with fibre cavities of sub-mm length is a promising path to increase the single-photon generation rate, and significant progress has been recently made in that direction [35, 78].

The first step towards generating entangled photon trains in an ion-cavity system would be to perform coherent manipulation of the ion qubit after photon generation, instead of the incoherent re-initialisation performed here. That step should be straightforward to achieve using the existing tools (729-nm laser) for manipulating the ion qubit available in the present work. The second step would be to reduce spontaneous scattering events during the photon generation process (re-initialising the ion in state $|u\rangle$), which destroy entanglement between sequentially generated cavity photons from a single ion. Indeed, in our current experimental configuration, these spontaneous scattering events would already strongly limit the probability with which two sequentially entangled photons could be generated.

Those same spontaneous scattering events also limit the extent to which the emitted photons are indistinguishable, as we [53] and others [109] have recently studied in an ion-cavity system. Sec. 6.7 presents schemes to increase the fraction of emitted cavity photons without prior spontaneous emission in our existing system from the current value of 0.52 to over 0.8, which we expect to allow for the observation of entanglement between several sequential photons. Detailed numerical simulations are required to determine the exact number of sequentially entangled photons that could be observed in our current system, for a given detection probability, and we leave this for future work. Schemes to further reduce the effects of spontaneous scattering in future experimental systems are discussed in Sec. 6.8.

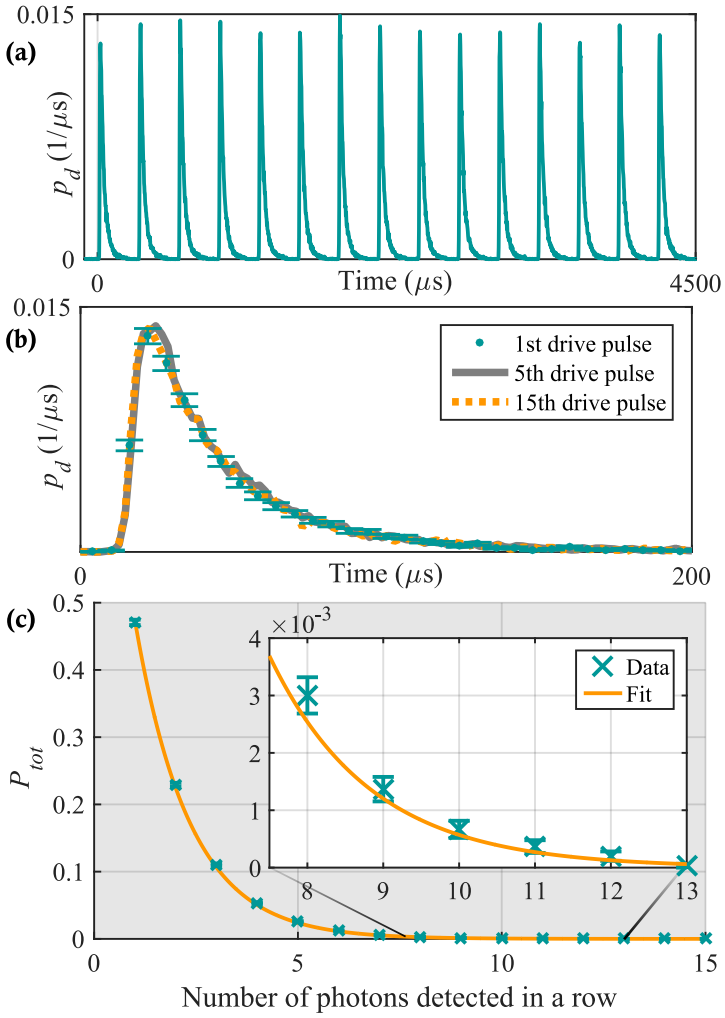


Fig. 6.5: **Photon trains: generation and detection of sequential photons.** **(a)** Measured wavepackets of 15 consecutive photon-generation attempts for $\Omega/2\pi \approx 12$ MHz. **(b)** Temporal overlap of the first, fifth, and fifteenth wavepacket in (a). **(c)** Probability of detecting a photon in $n$ consecutive wavepackets, starting from the first wavepacket, for a single-photon probability of 0.47. Orange line: weighted fit of the form $p^x$, with $p = 0.474(2)$ the best fit value. This figure has been reproduced from Fig. 5 of Ref. [38].

## 6.6 CHOICE OF THE TRANSMISSION $T_2$

In Sec. 2.2.2, the optimised upper bound $P_S^{opt}$ [calculated via Eq. (2.34)] was introduced, which requires the optimum output-mirror transmission $T_2^{opt}$ [calculated via Eq. (2.33)]. As a reminder, the optimised upper bound arises from a trade-off relation in the equation for $P_S^{bound}$ [Eq. (2.31)] between the probability for photon emission into the cavity ($P_{in}$) and the escape probability ($P_{esc}$) with respect to $T_2$.

Allowing for a different transmission $T_2$ of our outcoupling mirror, without changing the unwanted cavity loss $\alpha_{loss}$, cavity waist $w_0$ or the propagation direction of the drive laser, would only lead to a relatively small increase in $P_S^{bound}$: a value of $T_2^{opt} = 216$ ppm would increase $P_S^{bound}$ from 0.73 to 0.78 at the expense of reducing $P_S^{pure}$. In general there is a trade-off here. The probability $P_S^{pure}$ for obtaining a transform-limited photon (i.e., without prior decay to the initial state, see Sec. 2.2), has an upper bound that requires the optimum output-mirror transmission $T_2^{opt.pure} = 61$ ppm for our experiment, resulting in $P_S^{pure} \leqslant 0.39$. With our $T_2 = 90(4)$ ppm we get in between the upper bounds of both $P_S$ and $P_S^{pure}$, as can be seen in Fig. 6.6.

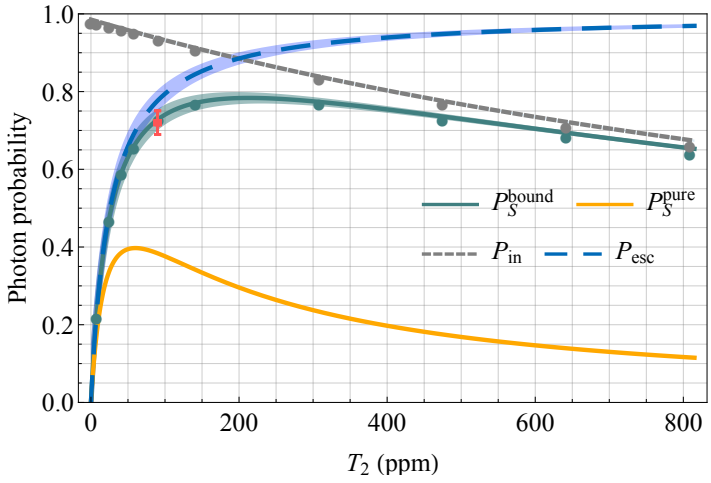


Fig. 6.6: **Predicted photon probabilities in our system as a function of the output-mirror transmission $T_2$.** Lines: analytical calculations, where $P_S^{bound}$ and $P_S^{pure}$ are calculated via Eq. (2.31) ($j = 0$ for $P_S^{pure}$) for the parameters summarised in Sec. 6.1. Shaded areas around $P_S^{bound}$ and $P_{esc}$ represent the uncertainties in the measured cavity parameters. Red dot with error bars: experimentally measured efficiency $P_S^{exp}$; error bars are due to the uncertainty in the efficiency of detector and photon path. Dots: numerical simulations (see Sec. 5.4). The numerically calculated efficiencies converge towards the analytic calculations for $\Omega/\Delta \ll 1$. Slight deviations for higher $T_2$ between analytic and numerical results are due to the finite evolution time used in the numerical simulations. This figure has been reproduced from Fig. 7 of Ref. [38].

## 6.7 POSSIBLE EFFICIENCY IMPROVEMENTS IN THE EXISTING SETUP

In this section, schemes are presented to enhance performance in our system without changing properties of the optical cavity. These schemes seek to increase the ion-cavity coupling strength $g$ which in turn increases the cooperativity [Eq. (2.25)]. Scheme A is our experimental benchmark: the experimental configuration of this thesis, where $g_{exp}/2\pi = 0.88(1)$ MHz. In scheme B, the drive laser propagates parallel to the magnetic field axis and cavity axis, achieving a factor of $\sqrt{2}$ larger polarisation projection $\zeta$ onto the dipole of the $|g\rangle \leftrightarrow |e\rangle$ transition, compared to Scheme A. Schemes C and D correspond to coupling two and three ions, respectively, in superradiant entangled states to the cavity, in addition to scheme B. Enhanced cavity coupling via superradiance has been demonstrated for two entangled ions [57] and it should be feasible to near-maximally couple three ions to our cavity. Fig. 6.7 compares the performance of schemes A-D, as a function of the normalised ion-cavity coupling strength $g/g_{exp}$. No significant improvement in $P_S^{bound}$ is evident: the value achieved in scheme A is already close to saturation ($P_{esc}$). In contrast, schemes B–D would enable significant improvements in $P_S^{pure}/P_S^{bound}$: the fraction of photons in the cavity output mode generated without prior spontaneous decay of the emitter can be significantly increased. Minimising spontaneous emission is important for schemes to generate sequentially entangled photons, as discussed in Sec. 6.5, and for the indistinguishability of the generated photons [53].

## 6.8 FUTURE SYSTEMS

We saturate the maximum probability for obtaining a photon in the output mode of the optical cavity $P_S^{exp.max}$, up to the statistical uncertainty in our data of a few percent (Sec. 6.3). Consequently, significant improvements in this parameter can only be achieved by changing properties of the cavity ($w_0$, $\alpha_{loss}$) or quantum emitter. We now present three parameter combinations for future experimental systems that would enable a significant improvement: specifically, over 0.9 for both $P_S^{bound}$ and $P_S^{pure}/P_S^{bound}$, where the latter is the fraction of photons occurring without re-initialisation events (Sec. 2.2). As a basis for the calculations we take the parameters of $w_0$, $\alpha_{loss}$ and emitter structure from our present system, assuming a polarisation projection $\zeta = 1$, unless otherwise indicated. The first parameter combination consists of a 10 times lower value of 2.7 ppm for $\alpha_{loss}$ combined with a value of 25 ppm for $T_2$. Such a low $\alpha_{loss}$ was reported in Ref. [110]. The second parameter combination consists of a 3 times smaller value of 3.9 μm for $w_0$ combined with a value of 252 ppm for $T_2$. Macroscopic cavities with waists down to 2.44 μm have been realised [111], albeit with far higher losses than ours. The third parameter combination

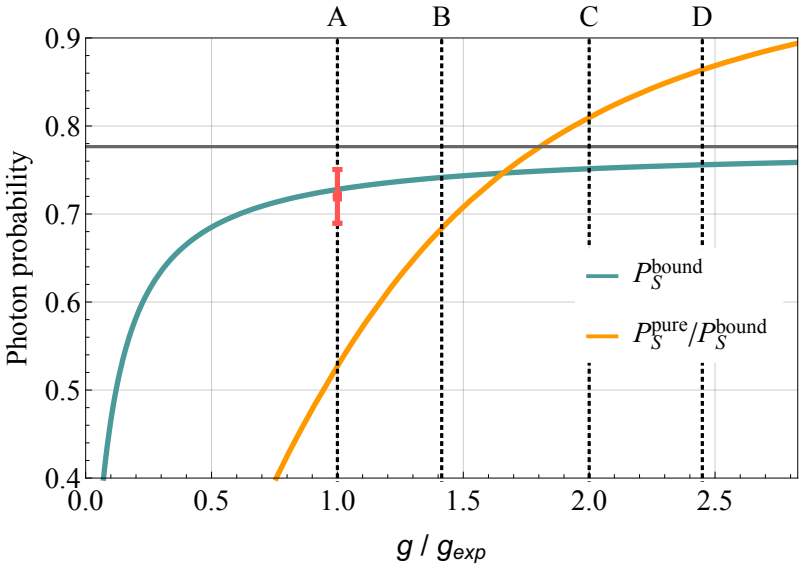


Fig. 6.7: **Possible efficiency improvements in our existing ion-cavity system.** Theoretical predictions for $P_S^{bound}$ and $P_S^{pure}/P_S^{bound}$, calculated via Eq. (2.31), with $j = 0$ for $P_S^{pure}$, when increasing the ion-cavity coupling strength $g$ over its current value $g_{exp}$. Labels A–D represent possible schemes in our system. Theoretical predictions use mean values for experimental parameters. Scheme A corresponds to the current experimental configuration, where $\zeta = \sqrt{0.5}$. Scheme B corresponds to changing the orientation of the drive-laser beam and magnetic field axis to be parallel to the cavity axis, such that $\zeta = 1$. Schemes C and D correspond to coupling two and three ions, respectively, in superradiant entangled states to the cavity, in addition to scheme B. Red dot with error bars: measured efficiency for a drive-laser field with $\Omega = 14$ MHz (Sec. 6.3). Horizontal grey line: photon escape probability through the cavity output mirror $P_{esc} = T_2/(T_2 + \alpha_{loss}) = 0.78$. This figure has been reproduced from Fig. 8 of Ref. [38].

consists of ten ions maximally coupled to the cavity in superradiant entangled states, and a value of 252 ppm for $T_2$. Superradiant states of two emitters coupled to a cavity have been demonstrated [57] and systems where the emitter string is parallel to the cavity axis [112, 113] offer a path to coupling many entangled single emitters to a single cavity mode. Indeed, it should be feasible to maximally couple up to three ions in superradiant states to our existing cavity, allowing for a significant improvement in $P_S^{pure}/P_S^{bound}$, as detailed in Sec. 6.7.

## 6.9 CONCLUSION

The results of this chapter present a significant advance in the collection efficiency $P_S$ of photons entangled with an ion. This advance was made possible by a cavity with a microscopic waist, total unwanted photon loss of 26(4) ppm and an outcoupling-mirror transmission that achieves close to the optimal compromise between photon emission

into the cavity and escape into the output mode. These are the key parameters which, together with the level structure of the quantum emitter, determine the optimal design for emitter-cavity systems with maximum photon collection efficiency. We have shown that our efficiency saturates, to within a few percent, the maximum value allowed by our cavity and emitter parameters. We thus could not achieve significantly higher efficiencies by, e.g., further optimising the photon generation scheme, changing to another scheme or further reducing the ion's spatial extent. Significant improvements would require a different value for the outcoupling-mirror transmission combined with either a smaller waist, lower unwanted losses or cavity-coupled superradiant states of multiple ions, or some combination of all these approaches.

The comparison between measured probabilities and theoretical limits presented in this chapter is relevant for quantum emitters beyond trapped ions, in particular, for the design of future systems optimising photon collection from, and absorption in, quantum matter.

# 7

# LIGHT-MATTER ENTANGLEMENT OVER 50 KM OF OPTICAL FIBRE

The first major result obtained during this PhD work was the distribution of ion-photon entanglement over 50 km of optical fibre. In order to overcome the limited (few-kilometre) travel range of 854-nm photons in the fibre, the setup presented in Ch. 4 was combined with a photon frequency-conversion stage, converting the generated photons to telecom wavelength. The conversion stage translates the frequency of incoming light at 854 nm to 1550 nm via difference frequency generation. The design, construction and characterisation of the conversion stage is reported in the PhD thesis of M. Meraner [41].

This chapter contains the results published in Ref. [39] and is organised as follows. After a short motivation for long-range quantum networks, the key challenges for distributing light-matter entanglement over long distance are outlined. This is followed by an overview of the experimental setup, including a brief description of the method and setup used for the photon frequency conversion. Next, the experimental results are presented which include the tomographically reconstructed entangled state of the ion qubit and photon polarisation qubit after 50 km, as well as an analysis of the achieved fidelity and photon distribution efficiency. Finally, in the light of these results, the prospects for 100-km ion-ion entanglement are discussed as well as a path to increase the rate.

## 7.1 MOTIVATION AND CHALLENGES

MOTIVATION: Envisioned quantum networks consist of distributed matter-based quantum nodes, for the storage, manipulation and application of quantum information. The nodes are interconnected with photonic links to establish entanglement between them [13]. While the most ambitious form of a quantum network is a collection of remote quantum computers, far simpler networks with a handful of qubits at each node could already enable powerful applications in quantum-enhanced distributed sensing, timekeeping, cryptography and multiparty protocols [14].

Entanglement has been achieved between two atoms in traps a few ten metres apart [114], between two ions in traps a few metres apart [31] and recently between two nitrogen-vacancy centres 1.3 km apart [115]. In these experiments, photon-matter entanglement is first generated, then detection of one or two photons heralds remote matter-matter entanglement (entanglement is "swapped" from matter-light to

matter-matter). A current goal is to significantly scale up the distance over which quantum matter can be entangled to a hundred kilometres or more, which are practical internode spacings to enable large-scale quantum networks.

Trapped ions are particularly powerful systems to enable quantum networking and the envisioned applications. For example, a complete set of tools for deterministic universal manipulation of quantum information encoded into registers of trapped ions is readily available and of a quality near fault-tolerant thresholds [94, 116, 117], as required for arbitrary distance quantum networking via the quantum repeater approach [27, 118]. Key quantum-networking functionalities have been demonstrated between ions over a few metres, including remote state teleportation [119] and multi-ion protocols [32]. Trapped ions are also some of the most sensitive measurement probes yet developed. For example, many ion species, including the one used in this work, contain optical atomic clock transitions; therefore, entangling them over distance enables the ideas presented in Refs. [16] and [120] to be explored.

In this work, entanglement between a trapped-ion qubit and a photon that has travelled over 50 km of optical fibre is achieved. The quality of the entanglement is sufficiently high to allow for a clear violation of a Bell inequality, as required for some of the most challenging device-independent quantum network applications [121]. Furthermore, when modestly optimised, the achieved rate is expected to allow for entanglement distribution between 100-km-spaced trapped ions at rates over 1 Hz.

CHALLENGES: Some key challenges to entangling matter over such distances are now described. First, the aforementioned matter systems emit photons at wavelengths that are strongly absorbed in optical waveguides (such as optical fibre), limiting the internode distance to a few kilometres. For example, in the present work 854-nm photons are collected from a trapped atomic ion. While the losses of ~3 dB per km suffered by 854-nm photons through state-of-the-art optical fibre allow for few-kilometre internode distances, the probability for transmission over 50 km of fibre would be $10^{-15}$. Single-photon frequency conversion to the telecom C band (1550 nm) offers a powerful solution: this wavelength suffers the minimum fibre-transmission losses (~0.18 dB per km, yielding 10% transmission over 50 km) and is therefore an ideal choice for a standard interfacing wavelength for quantum networking. Photons from solid-state memories [122], cold gas memories [123, 124], quantum dots and nitrogen-vacancy centres [125] have been converted to telecom wavelengths. Frequency conversion of photons from ions has very recently been performed, including to the telecom C band (without entanglement) [126], to the telecom O band with entanglement over 80 m [127] and directly to an atomic Rubidium line

at 780 nm [128]. The use of photon conversion to extend the distance over which light-matter and matter-matter entanglement can be distributed had not previously been achieved (at the date of publication of Ref. [39]).

A second challenge to long-distance matter entanglement is to preserve entanglement when such long photonic channels are involved. Uncontrolled decoherence processes that act on the photon as it travels along its path, and those that act on the quantum matter during the photon travel time, can easily destroy entanglement. For example, the entanglement-carrying photon signal, which attenuates exponentially with distance in any lossy waveguide, can be overwhelmed by added photon noise from the photon-frequency-conversion process or dark counts of the photon detectors. The inter-node photon travel time also imposes a minimum coherence time for matter, which for 50 km of optical fibre is already significant at 250 µs (and 500 µs to allow for the classical signal of a successful herald to return). Moreover, quantum-networking applications require distributed entanglement of a quality above certain thresholds, for which the required matter coherence times and photon signal-to-noise ratio are far more challenging [129].

A third challenge comes again from the photon travel time. The shortest time required to entangle remote matter (or indeed light) in two places is the light travel time between them. The 500-µs wait time over 50 km of optical fibre yields a maximum attempt rate of only 2 kHz: one must wait 500 µs to learn if an individual attempt to distribute remote entanglement has been successful. To achieve practical entanglement distribution rates in the face of such a restriction, one can work on achieving a high probability for individual attempts to succeed and/or run many attempts in parallel (as discussed later).

## 7.2 SETUP AND METHODS: INTRODUCING THE PHOTON FREQUENCY CONVERSION

A simplified overview of the experimental setup is provided in Fig. 7.1. The components of the ion-cavity node have already been described in Ch. 4 (see Sec. 4.1 for the cavity, Sec. 4.2 for the ion trap and Sec. 4.4.5 for the drive laser). Ion-photon entanglement is generated via the bichromatic CMRT introduced in Sec. 3.3. The directions of all laser beams and of the magnetic field are as described in Ch. 4 (the same as for the experiments presented in Ch. 6).

The bichromatic CMRT yields an entangled state with a frequency-degenerate photon qubit (the two polarisation components have the same frequency to within the cavity linewidth), providing a significant benefit for long-distance networking: the phase of the light-matter entangled state does not depend on the time at which the photon detection event occurs at a given distance from the ion [34]. Photon detection time fluctuates due to the intrinsic finite temporal extent

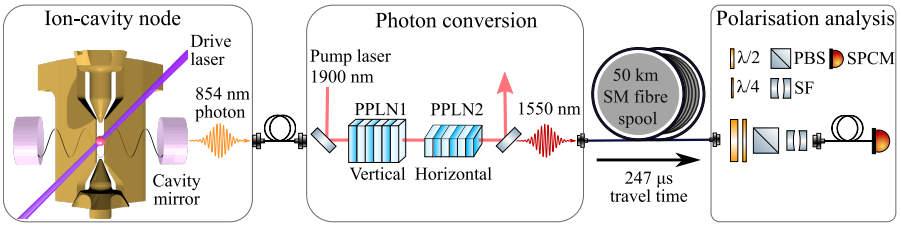


Fig. 7.1: **Simplified experiment schematic of the 50-km experiment.** From left to right: A photon at 854 nm is generated via the bichromatic CMRT (Sec. 3.3) in the ion-cavity setup described in detail in Ch. 4. The photon is thus polarisation-entangled with two electronic qubit states of the ion. Note that the direction of the drive beam is actually as described in Sec. 4.4.5 (perpendicular to the cavity axis and at 45° to the trap axis). The photon is then wavelength-converted to 1550 nm using difference frequency generation, involving ridge-waveguide-integrated periodically poled Lithium Niobate (PPLN) chips and a strong (1 W) pump laser at 1902 nm, as described in our paper [40]. The photon then passes through a 50-km SM-fibre spool. Finally, the photon is polarisation-analysed using waveplates, a PBS and a solid-state APD. Several spectral filters (SF; see main text) reduce noise from the conversion stage. This figure has been modified from Fig. 1 of Ref. [39].

of the photon wavepacket and for changes of the optical path length, which could be significant over tens of kilometres of deployed optical fibre. Our photons are generated over several tens of microseconds, with a corresponding bandwidth of tens of kilohertz. This unusually narrow bandwidth allows for strong frequency filtering, which we exploit in the photon conversion process, and could have further benefits in future deployed networks, e.g., to enable co-propagating classical and quantum light. Furthermore, the corresponding photon coherence length is potentially thousands of metres, allowing for essentially path-length-insensitive entanglement swapping between remote ions via Hong-Ou-Mandel interference [31, 130, 131].

*Photon frequency conversion*

Single-mode-fibre-coupled photons from the ion are injected into a polarisation-preserving photon-conversion system which was previously characterised using classical light [40]. A $\chi^{(2)}$ optical nonlinearity is used to realise difference frequency generation, whereby the energy of the 854-nm photon is reduced by that of a pump-laser photon at 1902 nm, yielding 1550 nm. Two commercially available PPLN ridge waveguide crystals[1] are used, which we will interchangeably refer to as *"chips"*, one to convert each polarisation.

While the ridge waveguides support all polarisations, only one polarisation component is converted per chip. In our system, each chip converts the vertically polarised component of the fields. A Fresnel

1 produced by NTT electronics

rhomb between the chips (equivalent to a broadband HWP) rotates horizontal to vertical polarisation of all three fields (854 nm, 1902 nm, 1550 nm), such that the second chip converts the polarisation component that is orthogonal with respect to the first chip. An estimated pump power of 0.2 W (vertically polarised) is required inside each chip for maximum conversion efficiency. A total of 1 W of pump light is sent to the input to the first chip, where the polarisation is set such that a balanced and maximum conversion efficiency is achieved in each of the chips.

A network of filters is used to extract the single telecom photon at the output of the conversion setup. The filters consist of a short-pass[2] for reducing the pump power, as well as a volume holographic Bragg grating[3], an etalon[4], and a 1550-nm bandpass filter[5] for reducing the 1550-nm noise photons from anti-Stokes Raman (ASR) scattering. The total fibre-coupled efficiency (fibre in, fibre out) of the conversion setup is 0.25(2), for an added white noise of 40(1) photons per second (also fibre coupled), within the filtering bandwidth of $2 \times 250$ MHz[6] centred at 1550 nm. The measurement and effect of background counts (noise) is further discussed in Sec. 7.4.1.

The 854-nm line in $^{40}Ca^{+}$ is almost unique amongst trapped-ion transitions in its potential for efficient and low-noise single-step frequency conversion to the telecom C band. In Ref. [40], results from a detailed study of the photon noise introduced by our photon convertor is presented. In summary, the dominant source of photon noise around 1550 nm is ASR scattering of the pump laser: the process whereby pump-laser photons at 1902 nm gain energy (get up-shifted to telecom wavelength) by scattering with energetic phonons inside the conversion waveguide. The ASR scattering (added photon noise) in our converter is spectrally white at telecom wavelength and can thus be reduced by narrowing the filtering bandwidth. In Ref. [40], we achieve a detected few counts per second added photon noise for a filtering bandwidth of 250 MHz, far broader than the ion-photon linewidth of about 0.1 MHz (this means that narrower filtering would be possible but is unnecessary). The initial ion-photon wavelength of 854 nm implies a broad spectral separation between pump-laser wavelength and 1550 nm, allowing for minimal ASR noise at the telecom wavelength. As discussed in Sec. 7.4.1, imperfections introduced by the converter in the ion-photon entangled state are consistent (to within statistical uncertainty) with the independently measured effects of detector dark counts and added photon noise. This means that no other source of error (e.g., imperfect polarisation preservation)

2 optical depth of 5 for 1902 nm, cut-off at 1600 nm
3 reflection bandwidth 0.2 nm, corresponding to 25 GHz at 1550 nm
4 250 MHz linewidth, 12.5 GHz FSR
5 12 nm bandwidth
6 Two transmission peaks of the etalon fall within the reflection bandwidth of the Bragg grating

could be distinguished to within statistical uncertainty. For a detailed analysis of the polarisation preservation of the converter, see Ref. [40].

*50-km fibre and polarisation analysis*

Following conversion, the telecom photon is injected into a 50.47-km SM fibre spool[7] with losses of 0.181 dB per km [10.4(5)% measured transmission probability]. The spool's environment is not actively stabilised, except for being inside a plastic box which is itself inside our air-conditioned lab. Polarisation dynamics in an unspooled fibre could be actively controlled using methods developed in the field of quantum cryptography (see, e.g., Ref. [132]). Finally, free-space projective polarisation analysis is performed and the photon is detected using a telecom solid-state APD[8] with an efficiency of 0.10(1) and free-running dark-count rate of 2 counts per second.

## 7.3 LASER PULSE SEQUENCE

The 247-µs photon travel time through the fibre limits the maximum attempt rate for generating a photon from the ion to 4 kHz. The attempt rate would be limited to 2 kHz if the fibre was stretched out away from our ion to force an additional delay for the classical signal ("detector click") to return. In the experiment, photon generation is (drive-laser pulses are) performed every 453 µs, until photon detection occurs, yielding an attempt rate of 2.2 kHz.

The laser pulse sequence, sketched in Fig. 7.2, is as follows. First, a 30-µs "initialisation" laser pulse at 393 nm is applied, measured by a photodiode in transmission of the ion-trap chamber, which allows for intensity stabilisation of the subsequent 393-nm drive-laser pulse via the sample-and-hold system described in Sec. 4.4.5. The initialisation pulse is followed by 1500 µs of Doppler cooling. Next, a loop starts in which single photons are generated. This loop consists of an additional Doppler cooling phase (50 µs), optical pumping to the state $|u\rangle = |S_{1/2}, m_j = -1/2\rangle$ via circularly polarised 397-$\sigma$ laser light (60 µs), and a 393-nm drive-laser pulse (30 µs). This is followed by a wait time for the photon to travel through the 50-km fibre and a subsequent photon detection window.

Measurement of the ion-qubit state is performed conditional on the detection of a 50-km photon within a 30-µs time window: the Zeeman ion qubit is mapped to the $^{40}Ca^{+}$ optical quadrupole qubit via laser pulses at 729 nm, followed by fluorescence state detection, as described in Sec. 5.3.

7 Corning SMF-28 ultra, Fiontec
8 InGaAs ID230 from IDQuantique

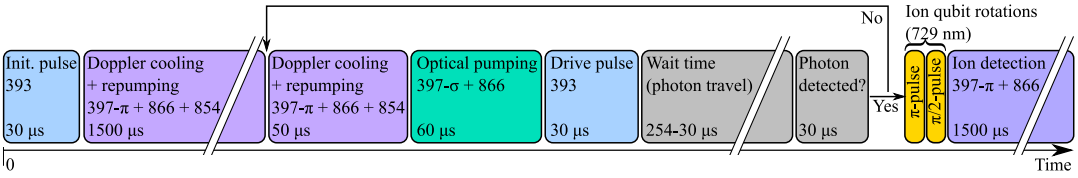


Fig. 7.2: **Laser-pulse sequence for the 50-km experiment.** The start of the sequence consists of an initialisation laser pulse for intensity stabilisation and of Doppler cooling. The loop, conditioned on the detection of a photon, consists of additional Doppler cooling, optical pumping, a (photon-generation) drive-laser pulse, a wait time as the photon travels through the 50-km fibre to the detector and a detection window. If a photon is detected, ion-qubit manipulation and state detection are performed, otherwise the loop repeats. The $\pi$-pulse is 10 µs long, the $\pi/2$-pulse is 5 µs long. This figure has been modified from Fig. 2 of the Supplementary Material of Ref. [39].

## 7.4 RESULTS

Quantum state tomography is performed to reconstruct the two-qubit (ion-qubit and photon-polarisation-qubit) state, as described in Sec. 5.3. All error bars on quantities derived from the tomographically reconstructed states (density matrices) are based on simulated uncertainties due to finite measurement statistics.

A strongly entangled ion-photon state is observed over 50 km (Fig. 7.3), quantified by a concurrence [133] C=0.75(5) and state fidelity F=0.86(3) with a maximally entangled state (for which C=1). Simulating a CHSH Bell-inequality test [134] on our tomographic data yields a value of 2.30(13), thereby exceeding the classical bound of 2 by 2.4 standard deviations. Using a shorter detection window (first 2/3 of the full photon wavepacket) increases the signal-to-noise ratio and yields F=0.90(3) and CHSH Bell-inequality violation by 4.8 standard deviations at the expense of an efficiency decrease of only 10% (the efficiency is further discussed in Sec. 7.4.2). The quality of our light-matter entangled state therefore surpasses this stringent threshold for its subsequent application.

### 7.4.1 *Imperfections in the entangled state*

In the following, it will be shown that the 50-km ion-photon-state infidelity can be explained by background detector counts and imperfections in the initial entangled state between ion and 854-nm photon. First, a summary of the sources of infidelity in the 50-km entangled state is presented, followed by a detailed analysis of the effect of background counts on the experimentally reconstructed quantum state.

In order to determine possible sources of infidelity, three independent experiments were performed, corresponding to state tomography of the ion-photon state at three different points in the photon path.

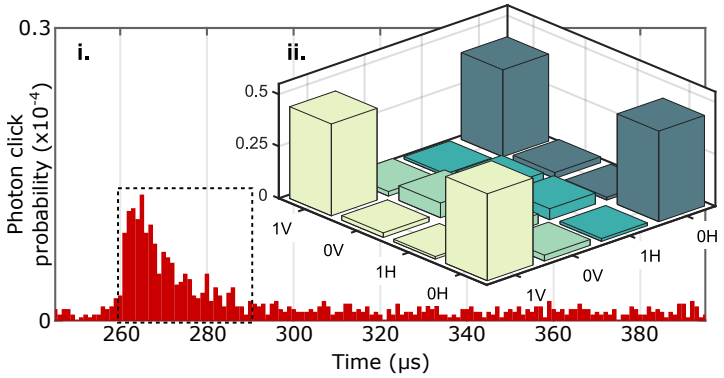


Fig. 7.3: **Observation of ion-photon entanglement over 50 km of optical fibre. (i)** 2D red bar chart: histogram of photon detection times (photon wavepacket in dashed box), following the generation of an 854-nm photon with a 30-μs drive-laser pulse approximately 250 μs earlier, repeated at 2.2 kHz. Ion-photon state tomography is performed for photon detection events recorded in the dashed box (total contained probability $P = 5.3 \times 10^{-4}$). **(ii)** 3D bar chart: absolute values of the experimentally reconstructed density matrix of the telecom-photonic-polarisation qubit and ion-qubit state ($|0\rangle = |g_2\rangle$, $|1\rangle = |g_1\rangle$). This figure has been reproduced from Fig. 2 of Ref. [39].

First, the ion-854-nm-photon state was characterised immediately at the cavity output using the free-space polarisation analysis and two SM-fibre-coupled 854-nm APDs (one at each port of the PBS) described in Sec. 4.5. A fidelity $F = 0.967(6)$ (with respect to a maximally entangled state) was measured at this point. With a purity $P = \mathrm{Tr}(\rho^2) = 0.94(1)$, where $\rho$ is the reconstructed state at 854 nm, the total state infidelity $[1 - F = 0.033(6)]$ is almost entirely due to a lack of purity. The same possible causes of the lack of purity can be given as for the entanglement experiment presented in Sec. 6.4 (imperfections in the 729-nm laser pulses used in the ion-qubit state analysis as well as imperfections in the polarisation analysis of the photon).

Second, the ion-1550-nm-photon state was characterised immediately after conversion, using only a 1-m telecom fibre instead of the 50-km spool. This is referred to as the 0-km distance, for which $F = 0.92(2)$ was measured. The observed drop in fidelity after the conversion stage is accompanied by a drop in the photon signal-to-noise ratio. Here, the noise consists to comparable rates of telecom-detector dark counts and conversion noise. The signal is reduced by the finite conversion-setup efficiency and the lower efficiency of the telecom detector compared to the ones at 854 nm.

Third, the ion-1550-nm-photon state is characterised after 50 km of travel (main result). To within statistical uncertainty, the drop in fidelity, going from the 0-km telecom value to after the 50-km spool, can be entirely explained by our telecom-photon-detector dark counts (2 counts per second). The reconstructed state fidelities are summarised

in Table 7.1 (bottom row "Experiment"). In the following, details on how we model the effect of background counts are given.

EFFECT OF BACKGROUND COUNTS: The effect of background-photon detector counts—defined as a detector clicks that didn't result from a photon from the ion—is analysed as follows. The background-count rate is extracted from the measured counts in the tomography experiments by looking outside the time window in which the generated photon arrives, yielding 2.0(1) counts per second (cps) for the 1550-nm photon at 50 km and 10(1) cps for the 854-nm photon, which are both in agreement with the telecom [1.9(2) cps] and 854-nm [10(1) cps and 11(1) cps] detectors' dark-count rates (measured independently). For the 1550-nm photon at 0 km we get a background of 4.0(1) cps, where the additional 2-cps background[9] is produced by the photon-conversion pump laser via ASR scattering, as reported in [40]. This added noise is attenuated at the same rate as the photons from the ion over the 50 km fibre and thus becomes a small contribution to the background compared to the intrinsic detector dark counts (which do not attenuate over distance).

The effect of background counts on the fidelity is simulated numerically. Specifically, the expected background-count probability in our photon time window is treated as white noise and added equally to all expected measurement-outcome probabilities for a perfect maximally-entangled Bell state, as also described in Sec. 5.3. Then a new "noisy-state" density matrix is reconstructed via Maximum Likelihood tomography. We call this approach *"Model 1"*, which simulates the effect of measured background counts only, and find that it explains the majority of the infidelity in the 50-km state, as can be seen from the values in Table 7.1.

| FIDELITY IN % | 854 nm, 0 km | 1550 nm, 0 km | 1550 nm, 50 km |
|---|---|---|---|
| MODEL 1 | 99.5 | 96 | 86 |
| MODEL 2 | - | 93 | 83 |
| EXPERIMENT | 96.7(6) | 92(2) | 86(3) |

Table 7.1: **Comparison of modelled and measured ion-photon entangled state fidelities.** Model 1: ideal Bell state subjected to background counts during photon-qubit measurement. Model 2: Experimentally reconstructed 854-nm state affected by background counts.

In addition to the background counts, *Model 2* takes the measured, imperfect 854-nm ion-photon state into account. That is, the tomo-

9 The 40 noise photons per second in the conversion setup, mentioned in Sec. 7.2, are estimated from these additional 2-cps background counts, taking into account the detector efficiency of 0.1 and PBS before the detector.

graphically reconstructed ion-854-nm photon state is used as the state to which background counts are added, in the same way as in Model 1. The results, shown in Table 7.1, indicate that background counts and imperfections in the initial 854-nm state explain the state infidelities to within statistical uncertainty.

Since the imperfections measured in the ion-photon state after conversion are consistent with those expected from added photon noise and detector dark counts, any other sources of imperfections (e.g., polarisation contrast loss; see [40] for a detailed analysis) cannot be resolved above the 1% infidelity level.

### 7.4.2 *Photon distribution efficiency*

The total probability that a drive-laser pulse leads to the detection of a photon after 50 km is $P = 5.3 \times 10^{-4}$, corresponding to a click rate of approximately 1 cps at the attempt rate of 2.2 kHz. Photon loss mechanisms that limit this probability in the experiment are discussed now.

The total probability of obtaining an on-demand free-space photon out of the cavity is $P_S = 0.5(1)$. This value is inferred from the measured efficiency with which we detect SM-fibre-coupled (ion-entangled) photons at 854 nm (before the conversion stage), after correcting for the measured efficiency of the first fibre-coupling stage and the known 854-nm-photon detector efficiency. The uncertainty in $P_S$ is dominated by the uncertainty in the efficiency of the first fibre-coupling stage. Both the efficiency and uncertainty of this fibre-coupling stage were improved for the experiments presented in Ch. 6 (see Sec. 4.5).

The overall efficiency of the frequency-conversion setup, including spectral filtering, is 0.25(2), measured with classical 854-nm light. For a detailed description, see Ref. [40]. Transmission through the 50-km fibre is measured to be 0.104(5). Together with an efficiency of 0.10(1) of the telecom photon detector, all the efficiencies listed above lead to a total expected probability of $6.5(1.5) \times 10^{-4}$ for detecting a photon after 50 km. This expected probability is consistent to within one standard deviation with the measured value of $5.3 \times 10^{-4}$. An overview of the efficiencies of all stages is provided in Table 7.2.

Several efficiency improvements have been implemented since the results presented here. The telecom APD was replaced by an SNSPD from Scontel with an efficiency of 0.77 at telecom and 0.8 dark counts per second. The efficiency of the first fibre-coupling stage was improved to 0.81(3) (Sec. 4.5). The probability $P_S$ was improved to 0.72(3) (Ch. 6). Combined, these improvements are sufficient to achieve a total 50-km efficiency of about 1%. See Sec. 7.5 for further efficiency improvements implemented in the ion-cavity node.

Additional improvements could be made in the efficiency of the photon conversion stage, which is currently limited by unwanted

| LOCATION IN THE PHOTON PATH | EFFICIENCY |
|---|---|
| On-demand photon out of cavity ($P_S$) | 0.5(1) |
| 1st single-mode-fibre coupling | 0.5(1) |
| Telecom conversion (incl. filters) | 0.25(2) |
| 50-km fibre transmission | 0.104(5) |
| Telecom photon detector | 0.10(1) |
| EXPECTED 50-KM DETECTION PROBABILITY | $6.5(1.6) \times 10^{-4}$ |

Table 7.2: **Photon losses in the 50-km photon distribution experiment.** See Fig. 7.1 for the respective locations in the experimental setup.

excitation of higher-order spatial modes in the involved PPLN ridge waveguides [40]. A total device efficiency of 0.5 should be within reach with more careful attention to coupling into the waveguides and minimising other passive optical losses (e.g., avoiding unnecessary fibre joints). Finally, lower-loss telecom fibres than the one used here are available (loss of 0.16 dB/km, Corning SMF-28 ULL) with a corresponding 50-km transmission of 0.16. Any improvement in fibre technology will further increase that value.

## 7.5 IMPLEMENTED EFFICIENCY IMPROVEMENTS

The experimental results of this chapter were obtained before the ones presented in Ch. 6. The results of the current chapter include a total detected probability of $P_{tot} = 0.08(1)$ for ion-entangled photons at 854 nm (calculated from the values in Table 7.2) as opposed to $P_{tot} = 0.462(3)$ presented in Ch 6. In the following, four key technical advances are summarised, implemented after obtaining the results presented in the current chapter, that enabled the performance presented in Ch. 6.

First, using the method described in Sec. 5.1, the ion was discovered to be approximately 0.5 mm away from the position of the cavity waist along the cavity axis. By correcting this imperfection, we estimate a reduction in the cavity effective mode area $A_{eff}$ at the point of the ion by a factor of two and corresponding increase in cooperativity $C$ [Eq. (2.25)] by the same factor.

Second, 3D ground-state cooling of the ion's motional state was carried out for the experiments of Ch. 6, compared with only Doppler cooling in the current chapter. The effect of being outside the ground state on cavity-photon generation in our system is described in Sec. 3.4.2. The coupling of our 393-nm drive-laser to the axial mode ($\eta = 0.13$) causes the most significant reduction of the Rabi frequency $\Omega_n$. The difference between photon generation with a Doppler-cooled and a sideband-cooled ion can be seen clearly in a Raman spectrum

(see Sec. 5.2), as shown in Fig. 7.4. On the carrier, the photon generation efficiency is increased after sideband cooling, due to the effect explained in Sec. 3.4.2. In the case of only Doppler cooling, first and second-order axial sidebands at multiples of $\pm 0.92$ MHz, as well as first-order radial sidebands at $\pm 2.4$ MHz, are clearly visible in the spectrum shown in Fig. 7.4. The suppression of red sidebands and reduction of blue sidebands after sideband cooling (most pronounced for the axial sidebands due to their larger Lamb-Dicke parameter) are a clear sign of an ion cooled close to the ground state of motion [61].

The third technical advance concerns the Rabi frequency $\Omega$ of the drive laser: the value used to achieve the highest efficiency in Ch. 6 ($\Omega/2\pi = 14$ MHz) is significantly lower than the value used for the 50-km entanglement distribution (where $\Omega/2\pi \approx 27$ MHz), thereby further reducing spontaneous scattering to the states $|g,0\rangle, |o,0\rangle$ (the states are defined in Sec. 3.2). The effect of the drive strength $\Omega$ on the photon-generation efficiency was investigated in Sec. 2.2.3 and Sec. 6.3.

As a fourth technical advance, the detection-path efficiency $P_{path}$ was increased: the SM-fibre coupling of the cavity output mode was improved from 0.5(1) to 0.82(5) (see Sec. 4.5), and the detector efficiency was improved from 0.4 to 0.87(2) for 854-nm photons and from 0.10(1) to 0.77 for 1550-nm photons by moving from APDs to SNSPDs.

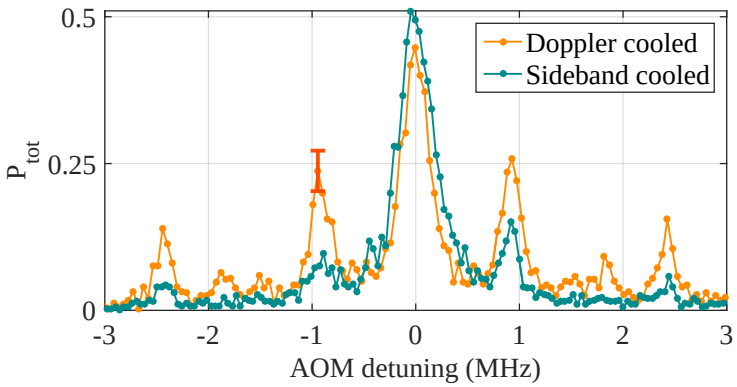


Fig. 7.4: **Raman spectrum after Doppler cooling and after sideband cooling.** A Raman spectrum (Sec. 5.2) of the $|S_{1/2}, m_j = -1/2\rangle \leftrightarrow |D_{5/2}, m_j = -5/2\rangle$ ($|u\rangle \leftrightarrow |g\rangle$) transition, centred on the carrier resonance, is shown after Doppler cooling and after sideband cooling. As a reminder, $P_{tot}$ is the probability for detecting a cavity photon per drive-laser pulse. Each data point represents the average of 200 photon generation attempts. Error bars are omitted for clarity (except for an exemplary point in the red sideband, corresponding to one standard deviation based on Poissonian counting statistics). The connecting lines are a guide for the eye. Note that this spectrum was taken with two SNSPDs instead of the single APD used for obtaining the spectrum shown in Fig. 5.3.

## 7.6 DISCUSSION

### 7.6.1 *Memory time*

One of the functions played by matter in a quantum network is as a memory to store established entanglement, while entanglement is being made or processed in other parts of the network. Decoherence processes in the matter qubit will limit the distance over which it is possible to distribute quantum entanglement (the distance a photon could possibly travel in the coherence time of the matter qubit). In our 50-km experiment, the ion qubit is already stored for the 250-μs photon travel time through the 50-km fibre, with no statistically significant reduction in the ion-photon entanglement quality. This was achieved by installing a mu-metal shield around the ion-trap vacuum chamber to attenuate ambient magnetic-field fluctuations.

Additional tomographic measurements are performed to see the rate at which ion-photon entanglement, stored in our ion-trap network node, deteriorates due to decoherence in the ion qubit. Increasing wait times are introduced between detection of the telecom-photon polarisation state (0-km fibre travel distance) and measurement of the ion-qubit state during state tomography. This is equivalent to introducing an additional storage time for the ion qubit. The results show that strong entanglement is still present after 20-ms wait time [$F = 0.77(4)$, $C = 0.57(8)$], the longest wait time employed. This already opens up the possibility of distributing entanglement over several thousands of kilometres and the time to perform hundreds of quantum-logic gates on one or multiple ion qubits [135].

A dominant source of decoherence of our ion qubit are uncontrolled fluctuating energy-level shifts due to intensity fluctuations of the 806-nm laser field used to lock the cavity around the ion. Further attention to minimising the absolute size of these fluctuations should lead to entanglement storage times of more than 100 ms. Beyond this, the ion qubit could be transferred to hyperfine clock transitions within different co-trapped ion species that offer coherence times of many seconds and longer [136].

### 7.6.2 *Ion-ion entanglement over 100 km*

The rates for future 100-km-spaced ion-ion entanglement, based on heralded photon-detection and using our methods, are now discussed. The experimental scheme is sketched in Fig. 7.5. A modestly optimised version of the experimental system presented in this chapter is now considered (see dashed box in Fig. 7.5) that achieves an on-demand detected 50-km photon click probability of $P = 0.01$ and operates at an attempt rate of $R = 2$ kHz (the two-way light travel time). By duplicating our optimised system, and following a two-photon-

click heralding scheme [130], the probability of heralding a 100-km spaced ion-ion entangled state would be $H_2 = \frac{1}{2}P^2 = 5 \times 10^{-5}$, at an average click rate of $H_2 \times R = 0.1$ cps (comparable with the first rates achieved over a few metres [137] of 0.03 cps). Following instead a one-photon-click heralding scheme [130], the probability of heralding a 100-km spaced ion-ion entangled state would be $H_1 = 2P \times 0.1 = 0.002$, with an average click rate of $H_1 \times R = 4$ cps, where 0.1 is the reduced photon-generation probability at each node (as required for this scheme). The factor 40 improvement ($H_1/H_2$) of the one-photon scheme over the two-photon scheme comes at the expense of the need to interferometrically stabilise the optical path length across the 100-km network.

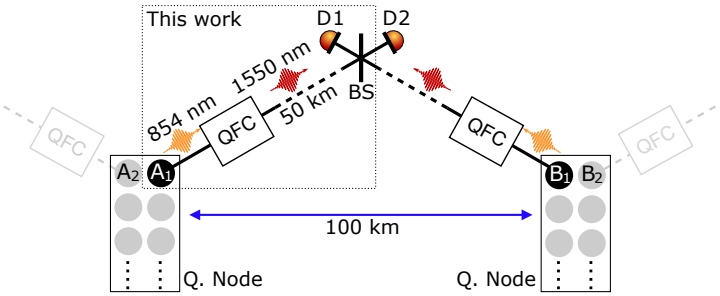


Fig. 7.5: **Path to 100-km matter-matter entanglement.** This work: quantum frequency conversion (QFC) converts a photon, emitted on-demand from and entangled with an ion qubit ($A_1$) in node A, to the telecom C band at 1550 nm. The photon then travels through 50 km of optical fibre before detection (D1 or D2). Future work: the current system is duplicated and the two photonic channels are interfered on a beam splitter (BS). Single or two-photon detection heralds the projection of ions $A_1$ and $B_1$ into an entangled state. Deterministic intra-node quantum logic and measurement between, e.g., $B_1 \leftrightarrow B_2$ and $A_1 \leftrightarrow A_2$ can swap the entanglement over larger distances (quantum repeater). Additional qubits in nodes are available for entanglement purification. This figure has been reproduced from Fig. 3 of Ref. [39].

An approach to significantly increase the remote entanglement heralding rate is multimode quantum networking, where many photons are sent, each entangled with different matter qubits. In this way, by running many such processes in parallel, the probability of at least one successful heralding event occurring can be made arbitrarily high. In our setup, for example, multiple ions can be trapped and it may be possible to produce a train of photons, each entangled with a different ion. In this case, a higher rate of photon production can be achieved, as the time between photons in the train is not limited by the light travel time. Furthermore, multimode networking could be realised using inhomogeneously broadened solid-state quantum memories [138]. Such memories could be connected with ions in a quantum network via a photon conversion interface [139] to form a powerful hybrid system for long distance quantum networking.

### 7.6.3 *Network of clocks*

The 50-km photon in our experiments is entangled with the 729-nm optical-qubit clock transition in $^{40}Ca^{+}$, over which a fractional frequency uncertainty of $1 \times 10^{-15}$ has been achieved (comparable with the Cs standard) [140]. Furthermore, $^{40}Ca^{+}$ can be co-trapped with $Al^{+}$ [141], which contains a clock transition for which a fractional systematic frequency uncertainty at the $1 \times 10^{-18}$-level was recently achieved [30]. Transfer of the remote $^{40}Ca^{+}$ entanglement to a co-trapped $Al^{+}$ ion could be done via quantum-logic techniques [142]. As such, our work provides a direct path to realise entangled networks of state-of-the-art atomic clocks over large distances [16]. Entangling clocks provides a way to perform more sensitive measurements of their average ticking frequencies [16] and to overcome current limits to their synchronisation [120].

# 8

# SUMMARY AND OUTLOOK

SUMMARY: This work contributes to the goal of improving control over the interaction of light and matter, at the single particle level. In particular, the thesis focused on improving the efficiency with which a single photon can be collected from a trapped ion and the distance over which ion-photon entanglement can be distributed. Both parameters are key requirements for envisioned quantum technologies like the quantum internet.

In the beginning of the thesis, the theoretical framework describing single-photon generation in the context of cavity QED was introduced, including theoretical efficiency limits that are set by the cavity and emitter parameters. Furthermore, the particular photon-generation scheme used in this thesis, based on a cavity-mediated Raman transition (CMRT), was presented, followed by a description of its implementation within the level structure of $^{40}Ca^{+}$.

The experimental setup was presented with a focus on the optical cavity, the careful design and construction of which represents a crucial ingredient for achieving the efficiencies reported in this thesis. Key aspects of the cavity are its near-concentric configuration and resulting microscopic waist [12.31(8) μm], its low [26(4) ppm] unwanted photon loss and the careful choice of the outcoupling-mirror transmission [90(4) ppm]. The latter allows for a close-to-optimal compromise between the probabilities of photon emission into the cavity and escape into the output mode. A detailed description of the methods used for characterising and constructing the cavity was given, hopefully serving as a useful reference for those performing similar work in the future.

Experimental results were presented on the generation of single photons using the new system, including the generation of ion-photon entanglement via a bichromatic CMRT. A maximum probability of 0.490(3) was measured for detecting a photon emitted by the ion and triggered by a drive-laser pulse. From this detected probability a photon-collection probability—the probability for obtaining a photon in the cavity output—of 0.72(3) could be inferred. That performance corresponds, to within a few percent, to operation at the theoretical efficiency limit to photon collection introduced previously, calculated to be 0.73(3) for our setup. Photons generated via a bichromatic CMRT and entangled with the ion were detected with a probability of 0.462(3), consistent with predictions of numerical simulations. This efficiency compares to the previous state of the art for a trapped ion of 0.057(2), achieved with another ion-cavity system in Innsbruck [34].

Having saturated the theoretical efficiency limit to photon collection, we could not achieve significantly higher efficiencies by, e.g., further optimising the photon generation scheme, changing to another scheme or improving the localisation of the ion wavepacket in cavity standing wave. Significant efficiency improvements in the photon-collection probability would require a different value for the outcoupling-mirror transmission combined with either a smaller cavity waist, lower unwanted cavity losses or cavity-coupled superradiant states of multiple ions, or some combination of all these approaches.

As an application of the newly constructed ion-photon interface and a further result of this thesis, the distribution of ion-photon entanglement was demonstrated over 50 km of optical fibre. For this purpose, the photonic qubit's natural wavelength at 854 nm was converted to 1550 nm via difference frequency generation. A fidelity of $F = 0.86(3)$ with a maximally-entangled state was measured, shown to be limited by background counts. The achieved distance of distributing light-matter entanglement is a step forward in long distance quantum networking, opening up the possibility of building long-distance fiber-based quantum networks.

In terms of the practical implementation of our ion-cavity system in future quantum networks, its main limitations are the rate with which ion-photon entanglement can be generated and the indistinguishability of the generated photons. Few-kHz rates for generating ion-photon entanglement were achieved in the experiments of this thesis, limited by the duration of the photon wavepackets. The long photon wavepackets are a consequence of our weak driving of the system in order to minimise the amount of spontaneous scattering and operate the system at the efficiency limit. Furthermore, the amount of spontaneous scattering events preceding photon generation, even as the drive strength tends to zero, significantly limits the indistinguishability of the photons generated in the current setup. Ways of improving both the rate and the indistinguishability were presented, ultimately requiring a higher ion-cavity coupling strength, which would allow for a higher probability and rate of photon emission into the cavity as opposed to scattering into free space.

OUTLOOK: Improvements in photon-collection efficiency from quantum matter are of fundamental importance since the process underpins widespread techniques for measuring the state of the quantum matter. A deterministic collection would constitute maximally efficient and minimally disruptive information transfer. An interesting future prospect for the interface presented in this thesis is to use it to access new regimes in the measurement of trapped-ion qubits, which is currently done via the electron shelving technique during which large numbers of photons are scattered. Using the near-deterministic photon collection achieved in this dissertation, it may be possible to

reliably determine the ion state whilst only scattering a few photons and thereby minimally disrupting the ion's motional state. Besides reducing the need for re-cooling, motionally non-destructive ion-qubit state readout could be feasible, opening new possibilities for the storage and engineering of quantum information in motional degrees of freedom. Indeed, at the time of writing this thesis first measurement are being carried out in that direction (by V. Krutyanskiy).

Another intriguing outlook is to combine the multiqubit quantum-logic capabilities of the trapped-ion platform with the high-efficiency photon generation achieved in this work, to generate many-body light-matter quantum states as a resource for quantum communication [14, 106] or computation [143]. Indeed, the detection of (unentangled) multiphoton states demonstrated in this thesis is a first step in that direction. At the time of writing this thesis, a project headed by a PhD student in our group (M. Canteri) is in progress, which aims at generating a three-photon entangled state via entanglement swapping using three ions in the trap.

One of the original motivations for building the setup described in this thesis was to use it as a node in an elementary quantum network. At the time of writing this thesis, experiments are being performed with the goal of entangling two ions, separated by 400 m, across the UIBK Technik campus: an ion in the setup of this work with an ion in the setup of Ref. [34] (most recently described in Ref. [144]). Ultimately, the envisioned network is to also include the fibre-cavity setup described in [145], which is still being developed.

# Part IV

# APPENDIX AND BIBLIOGRAPHY

# A

# IN SEARCH OF THE PERFECT MIRROR

## A.1 PROCURING THE CAVITY MIRRORS

Procuring our cavity mirrors, which are described in Sec. 4.1, took about two years, from the first inquiry with a company (mid 2015) to receiving the final batch of mirrors (mid 2017). In this section, key steps in the process are summarised.

The cavity-mirror substrates were manufactured and polished by the company Perkins Precision Development (PPD) in Boulder. A technical drawing of the substrates, provided by PPD, is shown in Fig. A.1. The super polishing of the surfaces of such tightly curved (10 mm ROC) mirror substrates seems not to be a commercially available process as standard: from approximately 20 contacted companies, PPD was the only one confident about achieving our required target specification of $< 1$ Å RMS surface roughness after super-polishing. This level of surface roughness seems to be a key requirement for mirrors with scattering and absorption loss L on the few-ppm level, as suggested by the results of Ref. [110] and from personal discussions with, among others, Tracy E. Northup and the companies Advanced Thin Films (ATF) and PPD. Moreover, loss measurements carried out on mirrors with 100 mm ROC, super-polished to below 1 Å RMS surface roughness as well as coated by the company ATF for the group of Tracy E. Northup at the UIBK, yielded a loss of $L < 5$ ppm per mirror. These characterisation results, which are summarised in Ref. [145] Sec. 3.2, served us as a benchmark for the targeted maximum loss of our 10-mm-ROC mirrors.

The coating runs that produced our final cavity mirrors were the last in a series of coating attempts that failed to produce the desired target of $L < 5$ ppm per mirror. The first coating attempt of the 10-mm-ROC substrates was performed by PPD (in mid 2016), with a targeted transmission of 2 ppm at 854 nm and less than 100 ppm at 785 nm. While the transmission targets were met (2 ppm at 854 nm and 60 ppm at 785 nm), the achieved cavity loss was $L_1 + L_2 = 51$ ppm (measured by PPD at 852 nm). PPD have since upgraded their coating facilities. After repolishing by PPD, the substrates were sent to ATF for coating. A coating run, with target transmission 2 ppm at 854 nm and 30–300 ppm at 785 nm, produced mirrors with L ranging from 13(3) ppm to more than 50 ppm per mirror at 854 nm, as measured by us via the methods outlined in Sec. 4.1.1 (transmission measurements using a laser and power meter combined with cavity-ringdown measurements). A minimum L of 14(3) ppm per mirror

was also measured for 100-mm-ROC mirrors, super-polished by ATF to below 1 Å RMS surface roughness and coated in the same run as the 10-mm ROC substrates from PPD. This higher-than-expected loss, compared to the UIBK substrates mentioned earlier, was due to the fact that ATF had reverted from a simple quarterwave stack to a different coating design structure. This was done in order to simultaneously meet both specified transmission targets (854 nm and 785 nm), despite the priority of keeping the loss L as small as possible.

Finally, two coating runs were ordered with ATF. One with transmission targets of 2 ppm at 854 nm and less than 100 ppm at 785 nm, with the specification that a simple quarterwave stack be used and a loss of $L < 5$ ppm be achieved per mirror. A total of 19 mirrors with 10 mm ROC were produced in this coating run, which we refer to as the "2-ppm batch". The other run was targeted for $100 \pm 20$ ppm at both 854 nm and 785 nm, with $L < 5$ ppm per mirror. A total of 20 mirrors with 10 mm ROC were produced in this coating run, which we refer to as the "100-ppm batch". The results of transmission and loss measurements on mirrors from the two batches are presented in the next section.

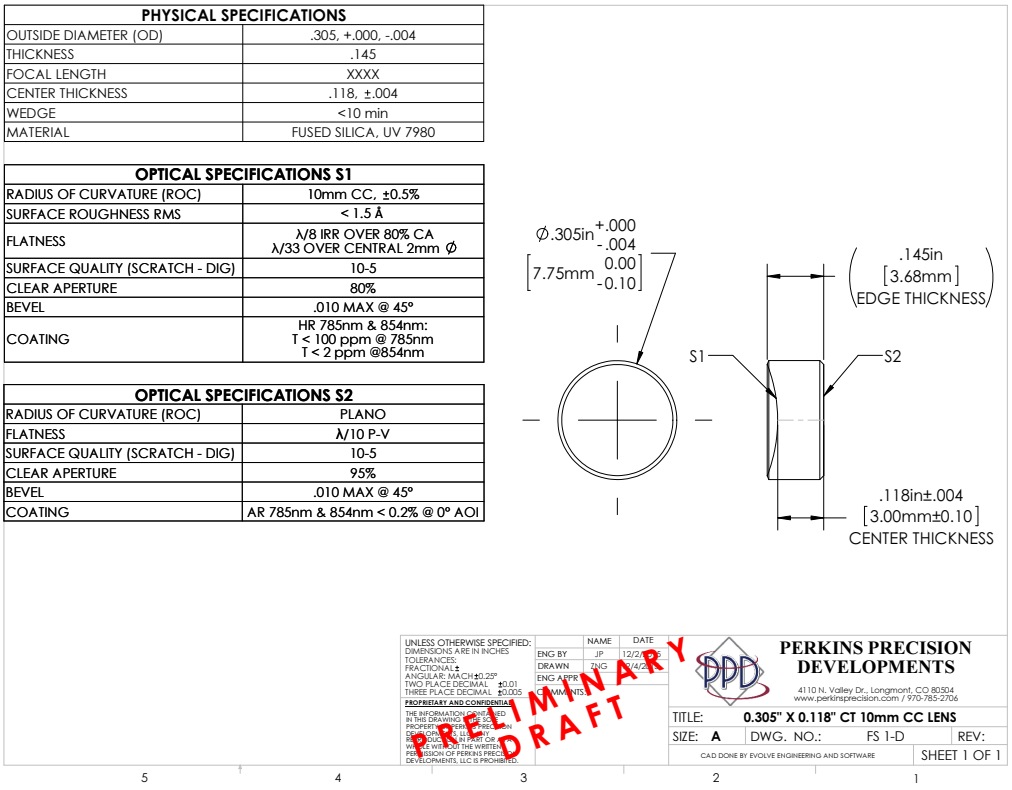

| PHYSICAL SPECIFICATIONS | |
|---|---|
| OUTSIDE DIAMETER (OD) | .305, +.000, -.004 |
| THICKNESS | .145 |
| FOCAL LENGTH | XXXX |
| CENTER THICKNESS | .118, ±.004 |
| WEDGE | <10 min |
| MATERIAL | FUSED SILICA, UV 7980 |

| OPTICAL SPECIFICATIONS S1 | |
|---|---|
| RADIUS OF CURVATURE (ROC) | 10mm CC, ±0.5% |
| SURFACE ROUGHNESS RMS | < 1.5 Å |
| FLATNESS | λ/8 IRR OVER 80% CA<br>λ/33 OVER CENTRAL 2mm Ø |
| SURFACE QUALITY (SCRATCH - DIG) | 10-5 |
| CLEAR APERTURE | 80% |
| BEVEL | .010 MAX @ 45° |
| COATING | HR 785nm & 854nm:<br>T < 100 ppm @ 785nm<br>T < 2 ppm @854nm |

| OPTICAL SPECIFICATIONS S2 | |
|---|---|
| RADIUS OF CURVATURE (ROC) | PLANO |
| FLATNESS | λ/10 P-V |
| SURFACE QUALITY (SCRATCH - DIG) | 10-5 |
| CLEAR APERTURE | 95% |
| BEVEL | .010 MAX @ 45° |
| COATING | AR 785nm & 854nm < 0.2% @ 0° AOI |



Fig. A.1: **Technical drawing of the cavity-mirror substrates.** With kind permission of PPD.

## A.2 CHARACTERISATION OF THE MIRROR BATCHES

In the following, characterisation measurements of individual mirrors from the two batches (2-ppm batch and 100-ppm batch) are presented. The labels used in this section to distinguish different mirrors corresponds to the storage location of the mirrors, with the designation "#1" for the top left corner of the box the mirrors are stored in, and then counting from left to right, row per row. The mirrors used for the final cavity consist of mirror #10 from the 2-ppm batch and mirror #6 from the 100-ppm batch.

*Mirror labels*

BATCH TRANSMISSION: The transmission of individual mirrors from each batch was measured for different wavelengths via the method using a laser and power meter presented in Sec. 4.1.1 (Method 1). As pointed out in Sec. 4.1.1, the transmission of the mirrors used for the final cavity changed when they were submitted to several bakes with maximum temperatures of 450 °C, in order to remove glue from unsuccessful attempts[1] of gluing the mirrors into mirror holders. The two mirrors were submitted to a total of three bakes and the transmission was measured before and after the first bake as well as after the final bake.

Fig. A.2a shows the results of transmission measurements for mirrors from the 2-ppm batch, together with the transmission profile provided by the coating company ATF. The pre-bake measurements yield a mean transmission of 2.2(2) ppm at 854 nm and 87(37) ppm at 785 nm. Measured and provided transmission profiles for mirrors from the 100-ppm batch are shown Fig. A.2b. Here, the pre-bake measurements yield a mean transmission of 132(4) ppm at 854 nm and 84(2) ppm at 785 nm.

As seen in Fig. A.2a, the bakes shifted the transmission curve of the 2-ppm cavity mirror towards higher wavelengths. While this shift did not affect the transmission at 854 nm, lying in the central flat region of the curve, the values at the edge of the high-reflective region changed drastically. As a consequence, the 785-nm wavelength originally intended for locking the cavity became unsuitable and a wavelength of 806 nm was chosen for the cavity lock (Sec. 4.1.3). As already mentioned in Sec. 4.1.2, the bakes did not contaminate the mirrors, i.e., the combined loss of the mirrors $L = L_1 + L_2$ did not increase by the glue removal, where L was extracted from combined measurements of the mirror transmission coefficients and cavity finesse (see Sec. 4.1.1).

Further transmission measurements of the cavity mirrors at 854 nm and 806 nm were carried out for the assembled, in-vacuum cavity following the protocol described in Ref. [79], as summarised in Sec. 4.1.1 (Method 2). The results are shown in Table 4.2. Note that the

1 These were the attempts where the cavity-mirror birefringence increased drastically due to the stress induced by the glue (see Sec. 4.1).

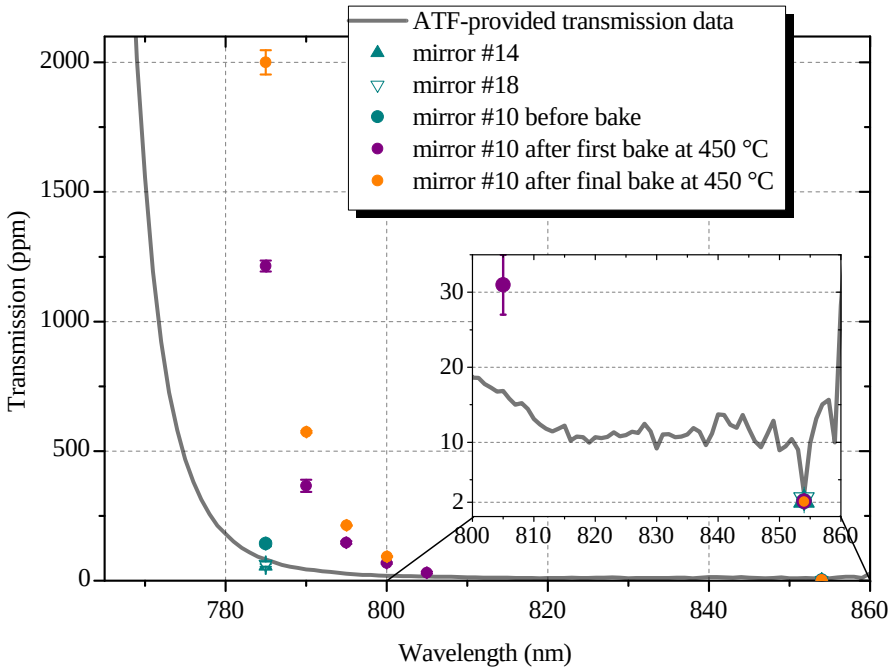


(a) Transmission of mirrors from the 2-ppm batch.

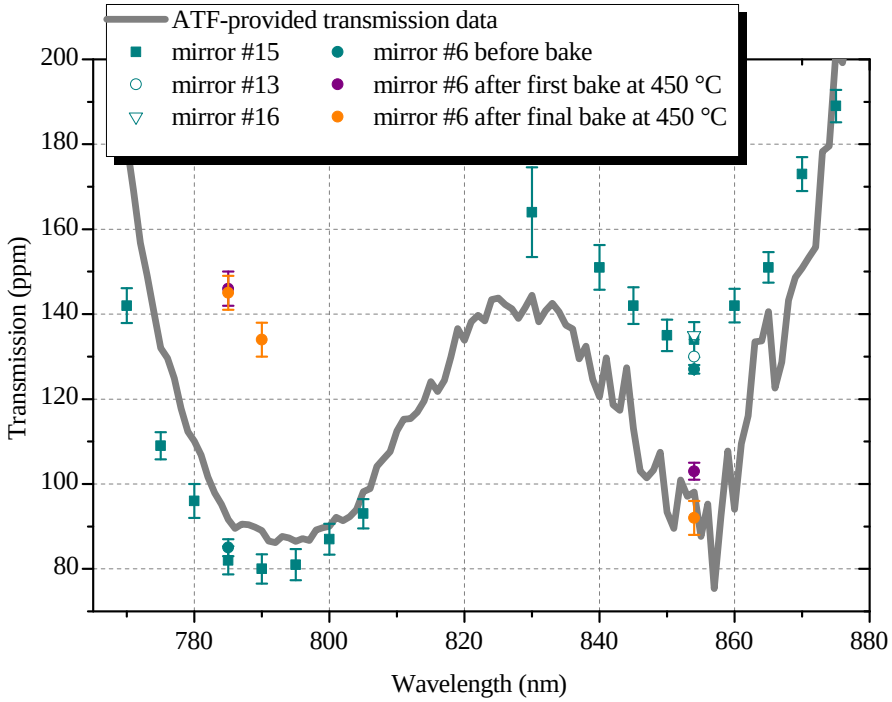


(b) Transmission of mirrors from the 100-ppm batch.

Fig. A.2: **Batch characterisation: transmission.** Error bars correspond to confidence intervals, determined by the uncertainty of the power measurements.

transmission coefficient of the 2-ppm mirror ($T_1$) at 806 nm measured for the in-vacuum cavity is much higher than the value apparent in Fig. A.2a (measured before the cavity was assembled). The reason for this

discrepancy is likely a strong dependence of the mirror transmission at 806 nm on the mirror alignment: slight differences in the angle between mirror and incident beam lead to significantly different transmission values.

BATCH FINESSE: The finesse of cavities formed by different mirror pairs from the two batches was measured via the cavity ringdown method presented in Sec. 4.1.1. The cavities were aligned out of vacuum in a test setup, with each mirror mounted on a multi-axes alignment stage. The ringdown measurements were performed for cavity lengths of 15–17 mm, with an estimated uncertainty of 0.5 mm, measured with a caliper. Fig. A.3a shows the results of these finesse measurements at 854 nm for cavities formed by two mirrors from the 2-ppm batch. The error bars are dominated by the length uncertainty. Also shown are the corresponding sums of transmission and loss $T + L$ per mirror, assuming symmetric mirror-transmission and -loss coefficients $T, L$ for each cavity (i.e., $T_1 + L_1 = T_2 + L_2 = T + L$, such that the total cavity loss is given by $\mathcal{L} = 2L + 2T$). A mean value of $T + L = 6.9(3)$ ppm is found for the 2-ppm batch.

Fig. A.3b shows the results of finesse measurements at 854 nm for cavities formed by a mirror from the 2-ppm batch and a mirror from the 100-ppm batch. Here, the sums of transmission and loss $T + L$ are shown for each of the 100-ppm mirrors, assuming for the 2-ppm mirrors the corresponding $(T + L)$-value from Fig. A.3a. Note that the finesse values of the final cavity presented in Sec. 4.1.1 were measured after the transmission change caused by the bakes.

FINESSE VS. CAVITY LENGTH: Fig. A.4 shows the results of cavity finesse measurements (at 854 nm) for increasing cavity lengths. For the mirror pair used for this measurement (2-ppm #14 and 100-ppm #15), the finesse decreases as the cavity approaches the concentric limit. Assuming that a change of the cavity length does not affect the mirror transmission coefficients (characterised in Figs. A.2a and A.2b), the decrease in finesse corresponds to an increase of the cavity loss $L_1 + L_2$, also displayed in the figure. This increase of the cavity loss is likely caused by defects further away from the mirror centres on the mirror surfaces, which are sampled by the larger cross sections of the cavity mode. As a consequence of the increased loss, a different mirror pair was chosen for the final cavity[2]. Unfortunately, for the final cavity a similar dataset as the one shown in Fig. A.4 does not exist. The results of ringdown measurements done with the final glued cavity (and therefore fixed length up to the piezo ranges) are detailed in Sec. 4.1.1.

2 #10 (2-ppm batch) and #6 (100-ppm batch), see beginning of this section for the labelling of the mirrors.

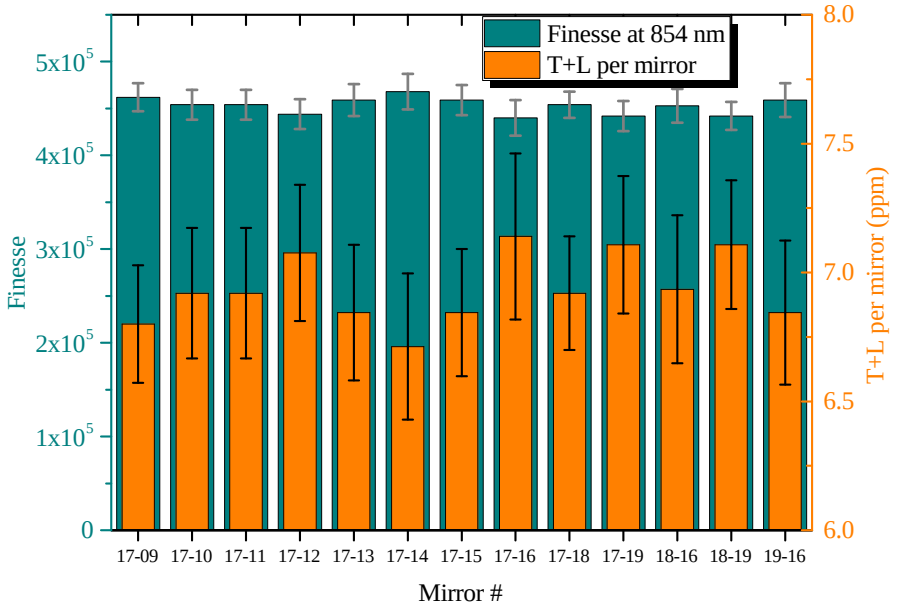


(a) Finesses of cavities formed by two mirrors from the 2-ppm batch.

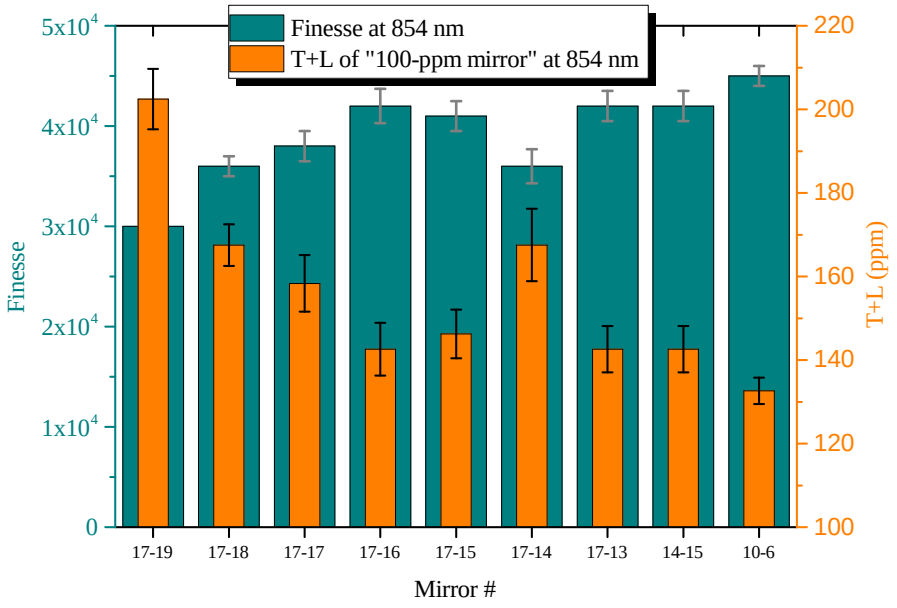


(b) Finesses of cavities formed by a mirror from the 2-ppm batch and a mirror from the 100-ppm batch.

Fig. A.3: **Batch characterisation: finesse.** The measurement of the mirrors #10 (2-ppm batch) and #6 (100-ppm batch), i.e., the pair used for the final cavity, was performed before the bakes mentioned earlier in this section (as also apparent from the extracted value of $T + L$ in subpanel b).

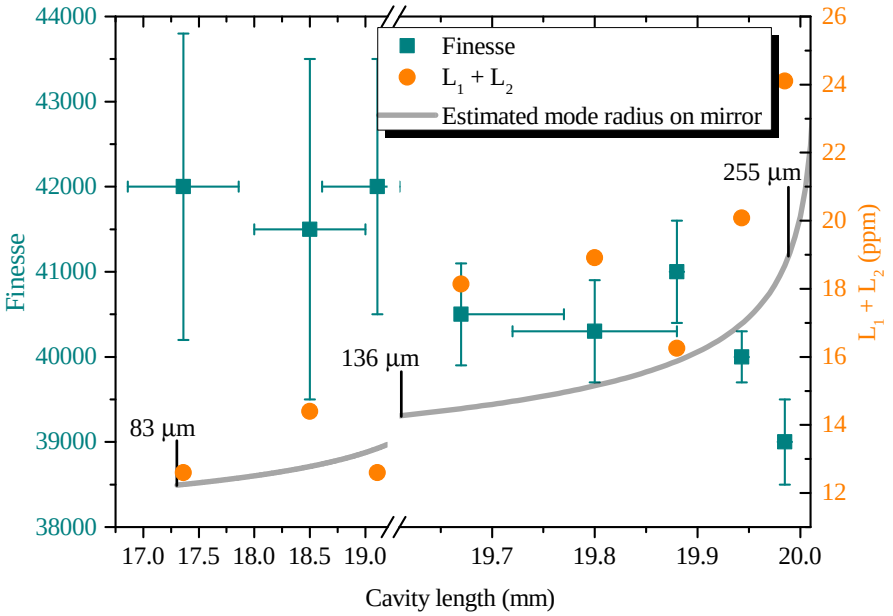


Fig. A.4: **Finesse vs. cavity length.** Example measurement for a mirror pair (2-ppm #14 and 100-ppm #15) where the measured cavity finesse (at 854 nm) decreases and the cavity loss $L_1 + L_2$ increases for increasing cavity lengths. The mode radius on the cavity mirrors was estimated via Eq. (2.6) for a measured mirror ROC of 10.010(2) mm for this cavity mirror pair. For datapoints up to a cavity length of 19.8 mm, the error in the finesse is dominated by an uncertainty in the cavity length (measured with a caliper, assuming that the error does not extend beyond neighbouring datapoints). For datapoints beyond cavity lengths of 19.8 mm (three rightmost points), the error corresponds to $\pm 1\sigma$ standard deviation determined from repeated measurements. The uncertainties in the corresponding values of $L_1 + L_2$, due to the error in the measured value of the Finesse for cavity lengths of more than 19.8 mm, are $\pm 2$ ppm.

# BIBLIOGRAPHY


[1] J. Bardeen and W. Brattain. "The Transistor, A Semiconductor Triode." In: *Proceedings of the IEEE* 86.1 (1998), pp. 29–30. DOI: 10.1109/JPROC.1998.658753.

[2] J. Bell and A. Aspect. "Introduction: John Bell and the second quantum revolution." In: *Speakable and Unspeakable in Quantum Mechanics*. Cambridge University Press, 2004, pp. xvii–xl. ISBN: 9780511815676. DOI: 10.1017/CBO9780511815676.002.

[3] J. P. Dowling and G. J. Milburn. "Quantum technology: the second quantum revolution." In: *Philosophical Transactions of the Royal Society of London. Series A: Mathematical, Physical and Engineering Sciences* 361.1809 (2003). Ed. by A. G. J. MacFarlane, pp. 1655–1674. DOI: 10.1098/rsta.2003.1227.

[4] R. P. Feynman. "Simulating physics with computers." In: *International Journal of Theoretical Physics* 21.6-7 (1982), pp. 467–488. DOI: 10.1007/BF02650179.

[5] D. Deutsch. "Quantum theory, the Church–Turing principle and the universal quantum computer." In: *Proceedings of the Royal Society of London. A. Mathematical and Physical Sciences* 400.1818 (1985), pp. 97–117. DOI: 10.1098/rspa.1985.0070.

[6] J. I. Cirac and P. Zoller. "Goals and opportunities in quantum simulation." In: *Nature Physics* 8.4 (2012), pp. 264–266. DOI: 10.1038/nphys2275.

[7] P. Shor. "Algorithms for quantum computation: discrete logarithms and factoring." In: *Proceedings 35th Annual Symposium on Foundations of Computer Science*. IEEE Comput. Soc. Press, 1994, pp. 124–134. ISBN: 0-8186-6580-7. DOI: 10.1109/SFCS.1994.365700.

[8] L. K. Grover. "A fast quantum mechanical algorithm for database search." In: *Proceedings of the twenty-eighth annual ACM symposium on Theory of computing - STOC '96*. Vol. 75. 6. New York, USA: ACM Press, 1996, pp. 212–219. ISBN: 0897917855. DOI: 10.1145/237814.237866.

[9] N. Gisin, G. Ribordy, W. Tittel, and H. Zbinden. "Quantum cryptography." In: *Reviews of Modern Physics* 74.1 (2002), pp. 145–195. DOI: 10.1103/RevModPhys.74.145.

[10] G. S. Solomon, C. Santori, and A. Kuhn. "Single Emitters in Isolated Quantum Systems." In: *Experimental Methods in the Physical Sciences*. Vol. 45. Elsevier Inc., 2013, pp. 467–539. ISBN: 9780123876959. DOI: 10.1016/B978-0-12-387695-9.00013-5.

[11] K. Heshami, D. G. England, P. C. Humphreys, P. J. Bustard, V. M. Acosta, J. Nunn, and B. J. Sussman. "Quantum memories: emerging applications and recent advances." In: *Journal of Modern Optics* 63.20 (2016), pp. 2005–2028. DOI: 10.1080/09500340.2016.1148212.

[12] C. Monroe, R. Raussendorf, A. Ruthven, K. R. Brown, P. Maunz, L.-M. Duan, and J. Kim. "Large-scale modular quantum-computer architecture with atomic memory and photonic interconnects." In: *Physical Review A* 89.2 (2014), p. 022317. DOI: 10.1103/PhysRevA.89.022317.

[13] H. J. Kimble. "The quantum internet." In: *Nature* 453.7198 (2008), pp. 1023–1030. DOI: 10.1038/nature07127.

[14] S. Wehner, D. Elkouss, and R. Hanson. "Quantum internet: A vision for the road ahead." In: *Science* 362.6412 (2018), eaam9288. DOI: 10.1126/science.aam9288.

[15] P. Sekatski, S. Wölk, and W. Dür. "Optimal distributed sensing in noisy environments." In: *Physical Review Research* 2.2 (2020), p. 023052. DOI: 10.1103/PhysRevResearch.2.023052.

[16] P. Kómár, E. M. Kessler, M. Bishof, L. Jiang, A. S. Sørensen, J. Ye, and M. D. Lukin. "A quantum network of clocks." In: *Nature Physics* 10.8 (2014), pp. 582–587. DOI: 10.1038/nphys3000.

[17] L.-M. Duan, M. D. Lukin, J. I. Cirac, and P Zoller. "Long-distance quantum communication with atomic ensembles and linear optics." In: *Nature* 414.6862 (2001), pp. 413–418. DOI: 10.1038/35106500.

[18] A. Reiserer and G. Rempe. "Cavity-based quantum networks with single atoms and optical photons." In: *Reviews of Modern Physics* 87.4 (2015), pp. 1379–1418. DOI: 10.1103/RevModPhys.87.1379.

[19] C. Junge, D. O'Shea, J. Volz, and A. Rauschenbeutel. "Strong Coupling between Single Atoms and Nontransversal Photons." In: *Physical Review Letters* 110.21 (2013), p. 213604. DOI: 10.1103/PhysRevLett.110.213604.

[20] H. Wang et al. "Towards optimal single-photon sources from polarized microcavities." In: *Nature Photonics* 13.11 (2019), pp. 770–775. DOI: 10.1038/s41566-019-0494-3.

[21] T. G. Tiecke, J. D. Thompson, N. P. de Leon, L. R. Liu, V. Vuletić, and M. D. Lukin. "Nanophotonic quantum phase switch with a single atom." In: *Nature* 508.7495 (2014), pp. 241–244. DOI: 10.1038/nature13188.

[22] T. Hummel, C. Ouellet-Plamondon, E. Ugur, I. Kulkova, T. Lund-Hansen, M. A. Broome, R. Uppu, and P. Lodahl. "Efficient demultiplexed single-photon source with a quantum dot coupled to a nanophotonic waveguide." In: *Applied Physics Letters* 115.2 (2019), p. 021102. DOI: 10.1063/1.5096979.

[23] C. D. Bruzewicz, J. Chiaverini, R. McConnell, and J. M. Sage. "Trapped-ion quantum computing: Progress and challenges." In: *Applied Physics Reviews* 6.2 (2019), p. 021314. DOI: 10.1063/1.5088164.

[24] N. Friis, O. Marty, C. Maier, C. Hempel, M. Holzäpfel, P. Jurcevic, M. B. Plenio, M. Huber, C. Roos, R. Blatt, and B. Lanyon. "Observation of Entangled States of a Fully Controlled 20-Qubit System." In: *Physical Review X* 8.2 (2018), p. 021012. DOI: 10.1103/PhysRevX.8.021012.

[25] J. Zhang, G. Pagano, P. W. Hess, A. Kyprianidis, P. Becker, H. Kaplan, A. V. Gorshkov, Z.-X. Gong, and C. Monroe. "Observation of a many-body dynamical phase transition with a 53-qubit quantum simulator." In: *Nature* 551.7682 (2017), pp. 601–604. DOI: 10.1038/nature24654.

[26] H. Häffner, F. Schmidt-Kaler, W. Hänsel, C. F. Roos, T. Körber, M. Chwalla, M. Riebe, J. Benhelm, U. D. Rapol, C. Becher, and R. Blatt. "Robust entanglement." In: *Applied Physics B* 81.2-3 (2005), pp. 151–153. DOI: 10.1007/s00340-005-1917-z.

[27] N. Sangouard, R. Dubessy, and C. Simon. "Quantum repeaters based on single trapped ions." In: *Physical Review A* 79.4 (2009), p. 042340. DOI: 10.1103/PhysRevA.79.042340.

[28] W. J. Munro, K. Azuma, K. Tamaki, and K. Nemoto. "Inside Quantum Repeaters." In: *IEEE Journal of Selected Topics in Quantum Electronics* 21.3 (2015), pp. 78–90. DOI: 10.1109/JSTQE.2015.2392076.

[29] I. Baumgart, J.-M. Cai, A. Retzker, M. B. Plenio, and C. Wunderlich. "Ultrasensitive Magnetometer using a Single Atom." In: *Physical Review Letters* 116.24 (2016), p. 240801. DOI: 10.1103/PhysRevLett.116.240801.

[30] S. M. Brewer, J.-S. Chen, A. M. Hankin, E. R. Clements, C. W. Chou, D. J. Wineland, D. B. Hume, and D. R. Leibrandt. "$^{27}Al^{+}$ Quantum-Logic Clock with a Systematic Uncertainty below $10^{-18}$." In: *Physical Review Letters* 123.3 (2019), p. 033201. DOI: 10.1103/PhysRevLett.123.033201.

[31] D. L. Moehring, P Maunz, S Olmschenk, K. C. Younge, D. N. Matsukevich, L.-M. Duan, and C Monroe. "Entanglement of single-atom quantum bits at a distance." In: *Nature* 449.7158 (2007), pp. 68–71. DOI: 10.1038/nature06118.

[32] D. Hucul, I. V. Inlek, G. Vittorini, C. Crocker, S. Debnath, S. M. Clark, and C. Monroe. "Modular entanglement of atomic qubits using photons and phonons." In: *Nature Physics* 11.1 (2015), pp. 37–42. DOI: 10.1038/nphys3150.

[33] L. J. Stephenson, D. P. Nadlinger, B. C. Nichol, S An, P Drmota, T. G. Ballance, K Thirumalai, J. F. Goodwin, D. M. Lucas, and C. J. Ballance. "High-Rate, High-Fidelity Entanglement of Qubits Across an Elementary Quantum Network." In: *Physical Review Letters* 124.11 (2020), p. 110501. DOI: 10.1103/PhysRevLett.124.110501.

[34] A. Stute, B. Casabone, P. Schindler, T. Monz, P. O. Schmidt, B. Brandstätter, T. E. Northup, and R. Blatt. "Tunable ion–photon entanglement in an optical cavity." In: *Nature* 485.7399 (2012), pp. 482–485. DOI: 10.1038/nature11120.

[35] P. Kobel, M. Breyer, and M. Köhl. "Deterministic spin-photon entanglement from a trapped ion in a fiber Fabry–Perot cavity." In: *npj Quantum Information* 7.1 (2021), p. 6. DOI: 10.1038/s41534-020-00338-2.

[36] A. Stute. "A light-matter quantum interface : ion-photon entanglement and state mapping." Dissertation. University of Innsbruck, 2012.

[37] H. Goto, S. Mizukami, Y. Tokunaga, and T. Aoki. "Figure of merit for single-photon generation based on cavity quantum electrodynamics." In: *Physical Review A* 99.5 (2019), p. 053843. DOI: 10.1103/PhysRevA.99.053843.

[38] J. Schupp, V. Krcmarsky, V. Krutyanskiy, M. Meraner, T. E. Northup, and B. P. Lanyon. "Interface between Trapped-Ion Qubits and Traveling Photons with Close-to-Optimal Efficiency." In: *PRX Quantum* 2.2 (2021), p. 020331. DOI: 10.1103/PRXQuantum.2.020331.

[39] V. Krutyanskiy, M. Meraner, J. Schupp, V. Krcmarsky, H. Hainzer, and B. P. Lanyon. "Light-matter entanglement over 50 km of optical fibre." In: *npj Quantum Information* 5.1 (2019), p. 72. DOI: 10.1038/s41534-019-0186-3.

[40] V. Krutyanskiy, M. Meraner, J. Schupp, and B. P. Lanyon. "Polarisation-preserving photon frequency conversion from a trapped-ion-compatible wavelength to the telecom C-band." In: *Applied Physics B* 123.9 (2017), p. 228. DOI: 10.1007/s00340-017-6806-8.

[41] M. Meraner. Dissertation. University of Innsbruck, to be published.

[42] C. Russo. "Photon statistics of a single ion coupled to a high-nesse cavity." Dissertation. University of Innsbruck, 2008.

[43] Siegman. *Lasers*. University Science Books, 1986. ISBN: 0935702113.

[44] P. Meystre and M. Sargent. *Elements of Quantum Optics*. Berlin, Heidelberg: Springer, 2007. ISBN: 978-3-540-74209-8. DOI: 10.1007/978-3-540-74211-1.

[45] C. Gerry and P. Knight. *Introductory Quantum Optics*. Cambridge: Cambridge University Press, 2004. ISBN: 9780521527354. DOI: 10.1017/CBO9780511791239.

[46] N. Ismail, C. C. Kores, D. Geskus, and M. Pollnau. "Fabry-Pérot resonator: spectral line shapes, generic and related Airy distributions, linewidths, finesses, and performance at low or frequency-dependent reflectivity." In: *Optics Express* 24.15 (2016), p. 16366. DOI: 10.1364/OE.24.016366.

[47] E. Jaynes and F. Cummings. "Comparison of quantum and semiclassical radiation theories with application to the beam maser." In: *Proceedings of the IEEE* 51.1 (1963), pp. 89–109. DOI: 10.1109/PROC.1963.1664.

[48] M. Hennrich. "Kontrollierte Erzeugung einzelner Photonen in einem optischen Resonator hoher Finesse." Dissertation. Technische Universität München, 2004.

[49] A. Kuhn and D. Ljunggren. "Cavity-based single-photon sources." In: *Contemporary Physics* 51.4 (2010), pp. 289–313. DOI: 10.1080/00107511003602990.

[50] E. M. Purcell. "Spontaneous Emission Probabilities at Radio Frequencies." In: *Physical Review*. 1995, p. 839. ISBN: 0031-899X. DOI: 10.1007/978-1-4615-1963-8_40.

[51] C. K. Law and H. J. Kimble. "Deterministic generation of a bit-stream of single-photon pulses." In: *Journal of Modern Optics* 44.11-12 (1997), pp. 2067–2074. DOI: 10.1080/09500349708231869.

[52] S. J. van Enk and H. J. Kimble. "Single atom in free space as a quantum aperture." In: *Physical Review A* 61.5 (2000), p. 051802. DOI: 10.1103/PhysRevA.61.051802.

[53] M. Meraner, A. Mazloom, V. Krutyanskiy, V. Krcmarsky, J. Schupp, D. A. Fioretto, P. Sekatski, T. E. Northup, N. Sangouard, and B. P. Lanyon. "Indistinguishable photons from a trapped-ion quantum network node." In: *Physical Review A* 102.5 (2020), p. 052614. DOI: 10.1103/PhysRevA.102.052614.

[54] C. Maurer, C. Becher, C. Russo, J. Eschner, and R. Blatt. "A single-photon source based on a single $Ca^+$ ion." In: *New Journal of Physics* 6 (2004), p. 94. DOI: 10.1088/1367-2630/6/1/094.

[55] H. G. Barros. "Raman spectroscopy and single-photon source in an ion-cavity system." Dissertation. University of Innsbruck, 2010.

[56] B. U. Brandstätter. "Integration of fiber mirrors and ion traps for a high-fidelity quantum interface." Dissertation. University of Innsbruck, 2013.

[57] B. Casabone. "Two Ions Coupled to an Optical Cavity : from an Enhanced Quantum Computer Interface towards Distributed Quantum Computing Dissertation." Dissertation. University of Innsbruck, 2015.

[58] K. Friebe. "On dispersive interactions between a trapped ion and a cavity field." Dissertation. University of Innsbruck, 2018.

[59] P. A. Barton, C. J. S. Donald, D. M. Lucas, D. A. Stevens, A. M. Steane, and D. N. Stacey. "Measurement of the lifetime of the $3d^2D_{5/2}$ state in $^{40}Ca^+$." In: *Physical Review A* 62.3 (2000), p. 032503. DOI: 10.1103/PhysRevA.62.032503.

[60] J. Jin and D. A. Church. "Precision Lifetimes of the $Ca^+$ $4p^2P$ Levels: Experiment Challenges Theory at the 1% Level." In: *Physical Review Letters* 70.21 (1993), pp. 3213–3216. DOI: 10.1103/PhysRevLett.70.3213.

[61] A. Stute, B. Casabone, B. Brandstätter, D. Habicher, H. G. Barros, P. O. Schmidt, T. E. Northup, and R. Blatt. "Toward an ion–photon quantum interface in an optical cavity." In: *Applied Physics B* 107.4 (2012), pp. 1145–1157. DOI: 10.1007/s00340-011-4861-0.

[62] R. Gerritsma, G. Kirchmair, F. Zähringer, J. Benhelm, R. Blatt, and C. F. Roos. "Precision measurement of the branching fractions of the $4p^2P_{3/2}$ decay of Ca II." In: *The European Physical Journal D* 50.1 (2008), pp. 13–19. DOI: 10.1140/epjd/e2008-00196-9.

[63] P. Müller and J. Eschner. "Single calcium-40 ion as quantum memory for photon polarization: a case study." In: *Applied Physics B* 114.1-2 (2014), pp. 303–306. DOI: 10.1007/s00340-013-5681-1.

[64] D. Leibfried, R. Blatt, C. Monroe, and D. Wineland. "Quantum dynamics of single trapped ions." In: *Reviews of Modern Physics* 75.1 (2003), pp. 281–324. DOI: 10.1103/RevModPhys.75.281.

[65] H. Haeffner, C. F. Roos, and R. Blatt. "Quantum computing with trapped ions." In: *Physics Reports* 469.4 (2008), pp. 155–203. DOI: 10.1016/j.physrep.2008.09.003.

[66] C. Roos. "Controlling the quantum state of trapped ions." Dissertation. University of Innsbruck, 2000.

[67] M. Ramm, T. Pruttivarasin, M. Kokish, I. Talukdar, and H. Häffner. "Precision Measurement for Branching Fractions of Excited $P_{1/2}$ States applied to $^{40}Ca^+$." In: *Physical Review Letters* 111.2 (2013), p. 023004. DOI: 10.1103/PhysRevLett.111.023004.

[68] J. Eschner, G. Morigi, F. Schmidt-Kaler, and R. Blatt. "Laser cooling of trapped ions." In: *Journal of the Optical Society of America B* 20.5 (2003), p. 1003. DOI: 10.1364/JOSAB.20.001003.

[69] C. Hempel. "Digital quantum simulation, Schrödinger cat state spectroscopy and setting up a linear ion trap." Dissertation. University of Innsbruck, 2014.

[70] P. Schindler, D. Nigg, T. Monz, J. T. Barreiro, E. Martinez, S. X. Wang, S. Quint, M. F. Brandl, V. Nebendahl, C. F. Roos, M. Chwalla, M. Hennrich, and R. Blatt. "A quantum information processor with trapped ions." In: *New Journal of Physics* 15.12 (2013), p. 123012. DOI: 10.1088/1367-2630/15/12/123012.

[71] F. Diedrich, J. C. Bergquist, W. M. Itano, and D. J. Wineland. "Laser Cooling to the Zero-Point Energy of Motion." In: *Physical Review Letters* 62.4 (1989), pp. 403–406. DOI: 10.1103/PhysRevLett.62.403.

[72] C. Roos, T. Zeiger, H. Rohde, H. C. Nägerl, J. Eschner, D. Leibfried, F. Schmidt-Kaler, and R. Blatt. "Quantum State Engineering on an Optical Transition and Decoherence in a Paul Trap." In: *Physical Review Letters* 83.23 (1999), pp. 4713–4716. DOI: 10.1103/PhysRevLett.83.4713.

[73] D. Wineland, C. Monroe, W. Itano, D. Leibfried, B. King, and D. Meekhof. "Experimental issues in coherent quantum-state manipulation of trapped atomic ions." In: *Journal of Research of the National Institute of Standards and Technology* 103.3 (1998), p. 259. DOI: 10.6028/jres.103.019.

[74] A. Kuhn, M. Hennrich, and G. Rempe. "Deterministic Single-Photon Source for Distributed Quantum Networking." In: *Physical Review Letters* 89.6 (2002), p. 067901. DOI: 10.1103/PhysRevLett.89.067901.

[75] J. McKeever, A. Boca, A. D. Boozer, R. Miller, J. R. Buck, A. Kuzmich, and H. J. Kimble. "Deterministic Generation of Single Photons from One Atom Trapped in a Cavity." In: *Science* 303.5666 (2004), pp. 1992–1994. DOI: 10.1126/science.1095232.

[76] M. Harlander, M. Brownnutt, W. Hänsel, and R. Blatt. "Trapped-ion probing of light-induced charging effects on dielectrics." In: *New Journal of Physics* 12.9 (2010), p. 093035. DOI: 10.1088/1367-2630/12/9/093035.

[77] F. R. Ong, K. Schüppert, P. Jobez, M. Teller, B. Ames, D. A. Fioretto, K. Friebe, M. Lee, Y. Colombe, R. Blatt, and T. E. Northup. "Probing surface charge densities on optical fibers with a trapped ion." In: *New Journal of Physics* 22.6 (2020), p. 063018. DOI: 10.1088/1367-2630/ab8af9.

[78] H. Takahashi, E. Kassa, C. Christoforou, and M. Keller. "Strong Coupling of a Single Ion to an Optical Cavity." In: *Physical Review Letters* 124.1 (2020), p. 013602. DOI: 10.1103/PhysRevLett.124.013602.

[79] C. J. Hood, H. J. Kimble, and J. Ye. "Characterization of high-finesse mirrors: Loss, phase shifts, and mode structure in an optical cavity." In: *Physical Review A* 64.3 (2001), p. 033804. DOI: 10.1103/PhysRevA.64.033804.

[80] T. D. Barrett, O. Barter, D. Stuart, B. Yuen, and A. Kuhn. "Polarization Oscillations in Birefringent Emitter-Cavity Systems." In: *Physical Review Letters* 122.8 (2019), p. 083602. DOI: 10.1103/PhysRevLett.122.083602.

[81] E. Kassa, W. Hughes, S. Gao, and J. F. Goodwin. "Effects of cavity birefringence on remote entanglement generation." In: *arxiv* (2020), pp. 1–11. arXiv: 2008.11712.

[82] A. J. Fleisher, D. A. Long, Q. Liu, and J. T. Hodges. "Precision interferometric measurements of mirror birefringence in high-finesse optical resonators." In: *Physical Review A* 93.1 (2016), p. 013833. DOI: 10.1103/PhysRevA.93.013833.

[83] B. Casabone, A. Stute, K. Friebe, B. Brandstätter, K. Schüppert, R. Blatt, and T. E. Northup. "Heralded Entanglement of Two Ions in an Optical Cavity." In: *Physical Review Letters* 111.10 (2013), p. 100505. DOI: 10.1103/PhysRevLett.111.100505.

[84] V. Krcmarsky. Dissertation. University of Innsbruck, to be published.

[85] E. D. Black. "An introduction to Pound–Drever–Hall laser frequency stabilization." In: *American Journal of Physics* 69.1 (2001), pp. 79–87. DOI: 10.1119/1.1286663.

[86] W. Paul. "Electromagnetic traps for charged and neutral particles." In: *Reviews of Modern Physics* 62.3 (1990), pp. 531–540. DOI: 10.1103/RevModPhys.62.531.

[87] P. K. Ghosh. *Ion Traps*. Clarendon Press, 1995. ISBN: 0198539959.

[88] M. Guggemos. "Precision spectroscopy with trapped $^{40}Ca^{+}$ and $^{27}Al^{+}$ ions." Dissertation. University of Innsbruck, 2017.

[89] H. Hainzer. "Laser Locking For Trapped-Ion Quantum Networks." Masters thesis. University of Innsbruck, 2018.

[90] D. Heinrich. "Ultrafast coherent excitation of a $^{40}Ca^{+}$ ion." Dissertation. University of Innsbruck, 2019.

[91] NIST. Atomic spectra database. URL: https://physics.nist.gov/PhysRefData/ASD/ionEnergy.html.

[92] G. Kirchmair. "Frequency stabilization of a Titanium-Sapphire laser for precision spectroscopy on Calcium ions." Dissertation. University of Innsbruck, 2006.

[93] D. F. V. James, P. G. Kwiat, W. J. Munro, and A. G. White. "On the Measurement of Qubits." In: *Physical Review A* 64.5 (2001), p. 052312. DOI: 10.1103/PhysRevA.64.052312.

[94] J. Benhelm. "Precision spectroscopy and quantum information processing with trapped calcium ions." Dissertation. University of Innsbruck, 2008.

[95] P. Schindler. "Frequency synthesis and pulse shaping for quantum information processing with trapped ions." Diploma thesis. University of Innsbruck, 2008.

[96] M. A. Nielsen and I. L. Chuang. *Quantum Computation and Quantum Information*. 2010. DOI: 10.1017/cbo9780511976667.

[97] M. Ježek, J. Fiurášek, and Z. Hradil. "Quantum inference of states and processes." In: *Physical Review A* 68.1 (2003), p. 012305. DOI: 10.1103/PhysRevA.68.012305.

[98] B. Efron and R. Tibshirani. "Bootstrap Methods for Standard Errors, Confidence Intervals, and Other Measures of Statistical Accuracy." In: *Statistical Science* 1.1 (1986), pp. 54–75. DOI: 10.1214/ss/1177013815.

[99] S. M. Tan. "Computational toolbox for quantum and atomic optics." In: *Journal of Optics B: Quantum and Semiclassical Optics* 1.4 (1999), pp. 424–432. DOI: 10.1088/1464-4266/1/4/312.

[100] P. B. R. Nisbet-Jones, J. Dilley, D. Ljunggren, and A. Kuhn. "Highly efficient source for indistinguishable single photons of controlled shape." In: *New Journal of Physics* 13.10 (2011), p. 103036. DOI: 10.1088/1367-2630/13/10/103036.

[101] O. Morin, M. Körber, S. Langenfeld, and G. Rempe. "Deterministic Shaping and Reshaping of Single-Photon Temporal Wave Functions." In: *Physical Review Letters* 123.13 (2019), p. 133602. DOI: 10.1103/PhysRevLett.123.133602.

[102] N. H. Lindner and T. Rudolph. "Proposal for Pulsed On-Demand Sources of Photonic Cluster State Strings." In: *Physical Review Letters* 103.11 (2009), p. 113602. DOI: 10.1103/PhysRevLett.103.113602.

[103] S. E. Economou, N. Lindner, and T. Rudolph. "Optically Generated 2-Dimensional Photonic Cluster State from Coupled Quantum Dots." In: *Physical Review Letters* 105.9 (2010), p. 093601. DOI: 10.1103/PhysRevLett.105.093601.

[104] I. Schwartz, D. Cogan, E. R. Schmidgall, Y. Don, L. Gantz, O. Kenneth, N. H. Lindner, and D. Gershoni. "Deterministic generation of a cluster state of entangled photons." In: *Science* 354.6311 (2016), pp. 434–437. DOI: 10.1126/science.aah4758.

[105] K. Azuma, K. Tamaki, and H.-k. Lo. "All-photonic quantum repeaters." In: *Nature Communications* 6.1 (2015), p. 6787. DOI: 10.1038/ncomms7787.

[106] J. Borregaard, H. Pichler, T. Schröder, M. D. Lukin, P. Lodahl, and A. S. Sørensen. "One-Way Quantum Repeater Based on Near-Deterministic Photon-Emitter Interfaces." In: *Physical Review X* 10.2 (2020), p. 021071. DOI: 10.1103/PhysRevX.10.021071.

[107] R. Lechner, C. Maier, C. Hempel, P. Jurcevic, B. P. Lanyon, T. Monz, M. Brownnutt, R. Blatt, and C. F. Roos. "Electromagnetically-induced-transparency ground-state cooling of long ion strings." In: *Physical Review A* 93.5 (2016), p. 053401. DOI: 10.1103/PhysRevA.93.053401.

[108] M. K. Joshi, A. Fabre, C. Maier, T. Brydges, D. Kiesenhofer, H. Hainzer, R. Blatt, and C. F. Roos. "Polarization-gradient cooling of 1D and 2D ion Coulomb crystals." In: *New Journal of Physics* 22.10 (2020), p. 103013. DOI: 10.1088/1367-2630/abb912.

[109] T. Walker, S. V. Kashanian, T. Ward, and M. Keller. "Improving the indistinguishability of single photons from an ion-cavity system." In: *Physical Review A* 102.3 (2020), p. 032616. DOI: 10.1103/PhysRevA.102.032616.

[110] G. Rempe, R. Lalezari, R. J. Thompson, and H. J. Kimble. "Measurement of ultralow losses in an optical interferometer." In: *Optics Letters* 17.5 (1992), p. 363. DOI: 10.1364/OL.17.000363.

[111] C. H. Nguyen, A. N. Utama, N. Lewty, and C. Kurtsiefer. "Operating a near-concentric cavity at the last stable resonance." In: *Physical Review A* 98.6 (2018), p. 063833. DOI: 10.1103/PhysRevA.98.063833.

[112] M. Cetina, A. Bylinskii, L. Karpa, D. Gangloff, K. M. Beck, Y. Ge, M. Scholz, A. T. Grier, I. Chuang, and V. Vuletić. "One-dimensional array of ion chains coupled to an optical cavity." In: *New Journal of Physics* 15.5 (2013), p. 053001. DOI: 10.1088/1367-2630/15/5/053001.

[113] S. Begley, M. Vogt, G. K. Gulati, H. Takahashi, and M. Keller. "Optimized Multi-Ion Cavity Coupling." In: *Physical Review Letters* 116.22 (2016), p. 223001. DOI: 10.1103/PhysRevLett.116.223001.

[114] S. Ritter, C. Nölleke, C. Hahn, A. Reiserer, A. Neuzner, M. Uphoff, M. Mücke, E. Figueroa, J. Bochmann, and G. Rempe. "An elementary quantum network of single atoms in optical cavities." In: *Nature* 484.7393 (2012), pp. 195–200. DOI: 10.1038/nature11023.

[115] B. Hensen et al. "Loophole-free Bell inequality violation using electron spins separated by 1.3 kilometres." In: *Nature* 526.7575 (2015), pp. 682–686. DOI: 10.1038/nature15759.

[116] P. Schindler, J. T. Barreiro, T. Monz, V. Nebendahl, D. Nigg, M. Chwalla, M. Hennrich, and R. Blatt. "Experimental Repetitive Quantum Error Correction." In: *Science* 332.6033 (2011), pp. 1059–1061. DOI: 10.1126/science.1203329.

[117] N. M. Linke, M. Gutierrez, K. A. Landsman, C. Figgatt, S. Debnath, K. R. Brown, and C. Monroe. "Fault-tolerant quantum error detection." In: *Science Advances* 3.10 (2017), e1701074. DOI: 10.1126/sciadv.1701074.

[118] H.-J. Briegel, W Dür, J. I. Cirac, and P Zoller. "Quantum Repeaters: The Role of Imperfect Local Operations in Quantum Communication." In: *Physical Review Letters* 81.26 (1998), pp. 5932–5935. DOI: 10.1103/PhysRevLett.81.5932.

[119] S Olmschenk, D. N. Matsukevich, P Maunz, D Hayes, L.-M. Duan, and C Monroe. "Quantum Teleportation Between Distant Matter Qubits." In: *Science* 323.5913 (2009), pp. 486–489. DOI: 10.1126/science.1167209.

[120] E. O. Ilo-Okeke, L. Tessler, J. P. Dowling, and T. Byrnes. "Remote quantum clock synchronization without synchronized clocks." In: *npj Quantum Information* 4.1 (2018), p. 40. DOI: 10.1038/s41534-018-0090-2.

[121] H. K. Lo, M. Curty, and B. Qi. "Measurement-device-independent quantum key distribution." In: *Physical Review Letters* 108.13 (2012), pp. 1–5. DOI: 10.1103/PhysRevLett.108.130503.

[122] N. Maring, P. Farrera, K. Kutluer, M. Mazzera, G. Heinze, and H. de Riedmatten. "Photonic quantum state transfer between a cold atomic gas and a crystal." In: *Nature* 551.7681 (2017), pp. 485–488. DOI: 10.1038/nature24468.

[123] A. G. Radnaev, Y. O. Dudin, R. Zhao, H. H. Jen, S. D. Jenkins, A. Kuzmich, and T. A. B. Kennedy. "A quantum memory with telecom-wavelength conversion." In: *Nature Physics* 6.11 (2010), pp. 894–899. DOI: 10.1038/nphys1773.

[124] B. Albrecht, P. Farrera, X. Fernandez-Gonzalvo, M. Cristiani, and H. de Riedmatten. "A waveguide frequency converter connecting rubidium-based quantum memories to the telecom C-band." In: *Nature communications* 5 (2014), p. 3376. DOI: 10.1038/ncomms4376.

[125] A. Dréau, A. Tcheborateva, A. E. Mahdaoui, C. Bonato, and R. Hanson. "Quantum Frequency Conversion of Single Photons from a Nitrogen-Vacancy Center in Diamond to Telecommunication Wavelengths." In: *Physical Review Applied* 9.6 (2018), p. 064031. DOI: 10.1103/PhysRevApplied.9.064031.

[126] T. Walker, K. Miyanishi, R. Ikuta, H. Takahashi, S. Vartabi Kashanian, Y. Tsujimoto, K. Hayasaka, T. Yamamoto, N. Imoto, and M. Keller. "Long-Distance Single Photon Transmission from a Trapped Ion via Quantum Frequency Conversion." In: *Physical Review Letters* 120.20 (2018), p. 203601. DOI: 10.1103/PhysRevLett.120.203601.

[127] M. Bock, P. Eich, S. Kucera, M. Kreis, A. Lenhard, C. Becher, and J. Eschner. "High-fidelity entanglement between a trapped ion and a telecom photon via quantum frequency conversion." In: *Nature Communications* 9.1 (2018), p. 1998. DOI: 10.1038/s41467-018-04341-2.

[128] J. D. Siverns, J. Hannegan, and Q. Quraishi. "Neutral-Atom Wavelength-Compatible 780 nm Single Photons from a Trapped Ion via Quantum Frequency Conversion." In: *Physical Review Applied* 11.1 (2019), p. 014044. DOI: 10.1103/PhysRevApplied.11.014044.

[129] S. Khatri, C. T. Matyas, A. U. Siddiqui, and J. P. Dowling. "Practical figures of merit and thresholds for entanglement distribution in quantum networks." In: *Physical Review Research* 1.2 (2019), p. 023032. DOI: 10.1103/PhysRevResearch.1.023032.

[130] L. Luo, D. Hayes, T. Manning, D. Matsukevich, P. Maunz, S. Olmschenk, J. Sterk, and C. Monroe. "Protocols and techniques for a scalable atom-photon quantum network." In: *Fortschritte der Physik* 57.11-12 (2009), pp. 1133–1152. DOI: 10.1002/prop.200900093.

[131] C. K. Hong, Z. Y. Ou, and L. Mandel. "Measurement of subpicosecond time intervals between two photons by interference." In: *Physical Review Letters* 59.18 (1987), pp. 2044–2046. DOI: 10.1103/PhysRevLett.59.2044.

[132] A. Treiber, A. Poppe, M. Hentschel, D. Ferrini, T. Lorünser, E. Querasser, T. Matyus, H. Hübel, and A. Zeilinger. "A fully automated entanglement-based quantum cryptography system for telecom fiber networks." In: *New Journal of Physics* 11.4 (2009), p. 045013. DOI: 10.1088/1367-2630/11/4/045013.

[133] W. K. Wootters. "Entanglement of Formation of an Arbitrary State of Two Qubits." In: *Physical Review Letters* 80.10 (1998), pp. 2245–2248. DOI: 10.1103/PhysRevLett.80.2245.

[134] J. F. Clauser, M. A. Horne, A. Shimony, and R. A. Holt. "Proposed Experiment to Test Local Hidden-Variable Theories." In: *Physical Review Letters* 23.15 (1969), pp. 880–884. DOI: 10.1103/PhysRevLett.23.880.

[135] B. P. Lanyon, C. Hempel, D. Nigg, M. Müller, R. Gerritsma, F. Zähringer, P. Schindler, J. T. Barreiro, M. Rambach, G. Kirchmair, M. Hennrich, P. Zoller, R. Blatt, and C. F. Roos. "Universal Digital Quantum Simulation with Trapped Ions." In: *Science* 334.6052 (2011), pp. 57–61. DOI: 10.1126/science.1208001.

[136] Y. Wang, M. Um, J. Zhang, S. An, M. Lyu, J.-N. Zhang, L.-M. Duan, D. Yum, and K. Kim. "Single-qubit quantum memory exceeding ten-minute coherence time." In: *Nature Photonics* 11.10 (2017), pp. 646–650. DOI: 10.1038/s41566-017-0007-1.

[137] D. N. Matsukevich, P. Maunz, D. L. Moehring, S. Olmschenk, and C. Monroe. "Bell Inequality Violation with Two Remote Atomic Qubits." In: *Physical Review Letters* 100.15 (2008), p. 150404. DOI: 10.1103/PhysRevLett.100.150404.

[138] C. Simon, H. de Riedmatten, M. Afzelius, N. Sangouard, H. Zbinden, and N. Gisin. "Quantum Repeaters with Photon Pair Sources and Multimode Memories." In: *Physical Review Letters* 98.19 (2007), p. 190503. DOI: 10.1103/PhysRevLett.98.190503.

[139] A. Seri, A. Lenhard, D. Rieländer, M. Gündoğan, P. M. Ledingham, M. Mazzera, and H. de Riedmatten. "Quantum Correlations between Single Telecom Photons and a Multimode On-Demand Solid-State Quantum Memory." In: *Physical Review X* 7.2 (2017), p. 021028. DOI: 10.1103/PhysRevX.7.021028.

[140] M. Chwalla, J. Benhelm, K. Kim, G. Kirchmair, T. Monz, M. Riebe, P. Schindler, A. S. Villar, W. Hänsel, C. F. Roos, R. Blatt, M. Abgrall, G. Santarelli, G. D. Rovera, and P. Laurent. "Absolute Frequency Measurement of the $^{40}Ca^{+}$ Clock Transition." In: *Physical Review Letters* 102.2 (2009), p. 023002. DOI: 10.1103/PhysRevLett.102.023002.

[141] M. Guggemos, D. Heinrich, O. A. Herrera-Sancho, R. Blatt, and C. F. Roos. "Sympathetic cooling and detection of a hot trapped ion by a cold one." In: *New Journal of Physics* 17.10 (2015), p. 103001. DOI: 10.1088/1367-2630/17/10/103001.

[142] P. O. Schmidt. "Spectroscopy Using Quantum Logic." In: *Science* 309.5735 (2005), pp. 749–752. DOI: 10.1126/science.1114375.

[143] J.-W. Pan, Z.-B. Chen, C.-Y. Lu, H. Weinfurter, A. Zeilinger, and M. Żukowski. "Multiphoton entanglement and interferometry." In: *Reviews of Modern Physics* 84.2 (2012), pp. 777–838. DOI: 10.1103/RevModPhys.84.777.

[144] D. A. Fioretto. "Towards a flexible source for indistinguishable photons based on trapped ions and cavities." Dissertation. University of Innsbruck, 2020.

[145] K. Schüppert. "Quantum interface - A fiber cavity perpendicular to a linear ion trap." Dissertation. University of Innsbruck, 2020.

## COLOPHON

This document was typeset using the typographical look-and-feel `classicthesis` developed by André Miede and Ivo Pletikosić. The style was inspired by Robert Bringhurst's seminal book on typography "*The Elements of Typographic Style*". `classicthesis` is available for both LaTeX and LyX:

https://bitbucket.org/amiede/classicthesis/

*Final Version* as of December 20, 2021 (classicthesis v4.6).